

Integrated Engines Design for Launch Vehicles

A project presented to
The Faculty of the Department of Aerospace Engineering
San José State University

In partial fulfillment of the requirements for the degree
Master of Science in Aerospace Engineering

By

Ashita J. Vattadikunnel

May 2022

Approved by

Dr. Periklis Papadopoulos
Faculty Advisor



© 2022
Ashita J. Vattadikunnel
ALL RIGHTS RESERVED

ABSTRACT

Integrated Engines Design for Launch Vehicles

Ashita J. Vattadikunnel

In the current times, as the aerospace industry begins to make large strides in space travel, a demand for an efficient and cost-effective propulsion system have never been more crucial. Even though there are successful and well-established rocket engines, the limitations of these engines are large. This averages the overall cost for cheaper space missions to be around million dollars, especially for massive propellant purchase. Therefore, it is essential for a propulsion system to utilize less propellant, achieve high speeds to escape earth's gravitational force and propel in space. Such objectives demand for more unique designs such as air-breathing propulsion systems. One benefit of designing an airbreathing rocket engine is the ability to carry less propellant during launch while being able to generate enough propulsion to leave earth. This directly translates to high thrust-to-weight ratio and increases a cost-effective design. However, the challenges for such a distinct design are numerous. One such vital issue is the ability to smoothly transition the airbreathing jet into a rocket engine while traveling at supersonic speeds. Both the feasibility and efficiency of this engine during transitional periods have been resounding obstacles. Regardless, there have been advancements made by Reactions Engine Limited which have responded to these obstacles with their Synergetic Air-breathing Rocket Engine. Even though this design has not achieved actual flight hours, all the preliminary tests are promising. Nevertheless, there are still outstanding issues present with this design. This research paper attempts to tackle some of these challenges by proposing a design and testing the model in a CFD simulation. The design process will include historical data analysis, trade studies, a form of Multi-objective Design Optimization process and a parametric study. Throughout the process, the model will be modified constantly for better performance in simulated tests.

ACKNOWLEDGEMENTS

I would like to take this moment to appreciate all my professors who imparted their knowledge and passion of aerospace engineering to me. Their dedication, patience and kindness are what motivated me to continue pursuing this field and keep challenging myself to know more every day. However, none of this would be possible if Dr. Nikos Mourtos had not granted me admission to this program back in Fall of 2018. Thanks to his guiding mentorship and encouraging words, I was able to surpass many obstacles and open my mind to new possibilities. He is the one who reminded me that school can only teach you how to retain new information quickly but it does not teach you everything about the industry. It is our job, as students, to apply these skills in any workplace so that we can adapt and grow. I would also like to thank Dr. Periklis Papadopolous, for being a supportive and caring advisor. There were times when I struggled to solve some issues in this project but with his advice and guidance, I was able to resolve those issues in a timely manner.

Furthermore, I am also very grateful to Nader Ali and Jordan Pollard for guiding me through Fluent Ansys. Through their support I was able to figure out the errors in some of my simulation selections which helped me get the results I needed for my project.

Also, I would like to give an enormous thanks to my family for being supportive during this career change and cheering me on from the sidelines even through my weakest moments. They reminded me to always be humble, and never give up on my dreams. Especially during the pandemic, their consideration and love is what allowed me to continue pursuing my degree.

TABLE OF CONTENTS

ACKNOWLEDGEMENTS	iiiv
TABLE OF CONTENTS	v
LIST OF TABLES	vii
LIST OF FIGURES	viii
NOMENCLATURE	x
CHAPTER 1 – INTRODUCTION	1
1.1 Motivation	1
1.2 Literature Review	2
1.2.1 Chemical Rockets with liquid propellants only	3
1.2.2 Hybrid Chemical Rockets	4
1.2.3 Airbreathing Hybrid Engines	6
1.2.4 Rocket Based Combined Cycle (RBCC)	7
1.3 Project Proposal	9
1.4 Methodology	10
1.5 Chapter Overview	10
CHAPTER 2 – MISSION SPECIFICATIONS AND COMPARATIVE STUDIES	13
2.1 Mission Objective	13
2.1.1 Mission Profile	13
2.1.2 Critical Mission Requirements	14
2.2 Comparative Study	15
2.2.1 Engine Configuration Selection	15
2.2.2 Comparison of Key Engine Parameters	23
2.3 Discussion and Conclusion	24
CHAPTER 3 – WEIGHT SIZING AND SENSITIVITY STUDIES	26
3.1 Introduction	26
3.2 Mission Weight Estimates	26
3.2.1 Engine Parameters of Similar Spacecrafts	26
3.2.2 Determination of Regression Coefficients	29
3.2.3 Determination of Mission Weights	30
3.3 HASA Model Weight Calculations	32
3.4 Trade Studies	36
3.5 Discussion and Conclusion	43
CHAPTER 4 - SELECTING DESIGN POINT (MDO)	44

4.1	Introduction	44
4.1.1	MDO for Airbreathing Engine	44
4.1.2	MDO for Rocket Engine	51
4.2	Discussion and Conclusion.....	55
CHAPTER 5 - COMPUTER AIDED DESIGN FOR AIRBREATHING ENGINE.....		56
5.1	Introduction	56
5.1.1	Calculations for CAD model	56
5.2	Method of Characteristics.....	61
5.3	Discussion and Conclusion.....	63
CHAPTER 6 – REDESIGNING THE CURRENT MODEL.....		67
6.1	Introduction	67
6.1.1	Designing Aerospike Nozzle.....	67
6.1.2	Designing Combustion Chamber	71
6.1.3	Designing Inlet	72
6.2	New 3D CAD Model and Dimensions	74
6.3	2D CFD Simulation and Results	75
6.3.1	Navier Stokes Equation	75
6.3.2	2D Geometry and Mesh.....	77
6.3.3	CFD Simulation.....	81
6.3.4	Results	82
6.4	Conclusion.....	90
CHAPTER 7 – DELTA V BUDGET		91
7.1	Introduction	91
7.2	Assumptions for Trajectory Calculations.....	93
7.3	Orbital Mechanics Calculations	94
7.4	Discussion and Conclusion.....	96
CHAPTER 8 – STAGING		98
8.1	Introduction	98
8.2	Required parameters	98
8.3	Calculations for optimized parameters.....	100
8.4	Discussion and Conclusion.....	102
REFERENCES		105
APPENDIX A - HASA WEIGHT CALCULATIONS.....		112
APPENDIX B – MATLAB CODE FOR DESIGN POINT		115
APPENDIX C – MATLAB CODE FOR STAGING.....		126

LIST OF TABLES

TABLE 2.0.1 – DETAILED SUMMARY OF MISSION OBJECTIVES FOR THE PROPOSED ENGINE	13
TABLE 2.0.2 – KEY ENGINE PARAMETERS IN THEIR RESPECTIVE ENVIRONMENTS.....	15
TABLE 2.0.3 – IMPERATIVE ENGINE PERFORMANCE PARAMETERS.....	23
TABLE 3.0.1 – WEIGHT DATA OF SPACECRAFTS WITH SIMILAR MISSION OBJECTIVES	27
TABLE 3.0.2 – WEIGHT FRACTIONS.....	31
TABLE 3.0.3 – WEIGHT ITERATION.....	32
TABLE 3.0.4 – IDEAL AND ACTUAL VALUES OF THE PROPOSED MODEL	35
TABLE 3.0.5 – FINAL WEIGHT RESULTS.....	36
TABLE 3.0.6 – SUMMARY OF ALL KEY PARAMETERS	43
TABLE 4.0.1 – NECESSARY CONSTRAINTS FOR MDO ANALYSIS.....	46
TABLE 4.0.2 – SUMMARY OF ALL THREE DESIGN POINTS FOR THE ENGINE	55
TABLE 5.0.1 – CALCULATED VALUES OF ALL THE VARIABLES LISTED ABOVE.....	60
TABLE 5.0.2 – ENGINE'S CALCULATED DIMENSIONS AND PARAMETERS	64
TABLE 6.0.1 - COMPARISON CHART BETWEEN DIFFERENT AEROSPIKE MODELS	68
TABLE 6.0.2 - SETTINGS FOR THE MESH GRID	79
TABLE 6.0.3 - SETTINGS FOR INLET AND COWL MESH GRID	80
TABLE 6.4 - SOLUTION INPUTS FOR SIMULATING LINEAR AEROSPIKE NOZZLE AT SEA-LEVEL	81
TABLE 7.0.1 – KNOWN VALUES FOR HOHMANN TRANSFER CALCULATIONS	93
TABLE 7.0.2 – TOTAL DELTA-V BUDGET AND CONVERSION TO ENGLISH UNITS.....	97
TABLE 8.0.1 – ALL THE REQUIRED AND CALCULATED VALUES FOR OPTIMUM MASSES.....	102

LIST OF FIGURES

FIGURE 1.0.1 – GENERAL SCHEMATIC OF A MONOPELLANT ENGINE.....	3
FIGURE 1.0.2 – GENERAL SCHEMATIC OF A BIPELLANT ENGINE	4
FIGURE 1.0.3 – EXAMPLES OF DIFFERENT HYBRID MOTORS	5
FIGURE 1.0.4 – BASIC LAYOUT OF SABRE ENGINE	6
FIGURE 1.0.5 – FOUR BASIC MODES OF A RBCC ENGINE	8
FIGURE 2.0.1 – MISSION PROFILE WITHIN EARTH’S ATMOSPHERE	14
FIGURE 2.0.2 – ORBITAL TRAJECTORY OF LUNAR FLYBY	14
FIGURE 2.0.3 – BOTTOM VIEW OF THE TURBOJET AND ROCKET ENGINE INSTALLMENT	16
FIGURE 2.0.4 – BOTTOM VIEW OF THE TURBOJET AND ROCKET ENGINE INSTALLMENT	16
FIGURE 2.0.5 – SCHEMATIC DIAGRAM OF VARIANT OF SEPR 841.....	16
FIGURE 2.0.6 – TOP VIEW OF SPACESHIPONE WITH ROCKET NOZZLE	17
FIGURE 2.0.7 – BASIC LAYOUT OF THE HYBRID ENGINE FOR SPACESHIPONE	17
FIGURE 2.0.8 – TRIDENT II WITH TURBOMECA GABIZO AND SEPR 631 ENGINE	18
FIGURE 2.0.9 – SCHEMATIC LAYOUT OF TURBOMECA VARIANT	18
FIGURE 2.0.10 – TOP VIEW OF SEPR 631 ENGINE	19
FIGURE 2.0.11 – SR-71 BLACKBIRD IN FLIGHT	19
FIGURE 2.0.12 – SCHEMATIC DRAWINGS OF J-58 TURBORAMJET	20
FIGURE 2.0.13 – RETIRED LOCKHEED NF-104A ROCKET ENGINE ATTACHMENT.....	21
FIGURE 2.0.14 – BASIC SCHEMATIC DRAWING OF J-79 VARIANT	21
FIGURE 2.0.15 – ROCKETDYNE AR2-3	22
FIGURE 2.0.16 – TESTING A SKYLON SPACECRAFT	22
FIGURE 2.0.17 – INNER VIEW OF TRADITIONAL SABRE	23
FIGURE 3.0.1 – GRAPH OF REGRESSION COEFFICIENT.....	30
FIGURE 3.0.2 – EFFECT OF WEIGHT COEFFICIENTS ON OVERALL TURBORAMJET ENGINE WEIGHT	37
FIGURE 3.0.3 – STUDY OF WEIGHT COEFFICIENTS ON OVERALL ENGINE WEIGHT OF ROCKETS.....	38
FIGURE 3.0.4 – THRUST STRUCTURE WEIGHT IS A FUNCTION OF TOTAL VACUUM THRUST, ADAPTED FROM [44]	39
FIGURE 3.0.5 – EFFECT OF WEIGHT COEFFICIENT ON VARIABLE INLET RAMP.....	40
FIGURE 3.0.6 – STUDY ON INLET RAMP LENGTH.....	41
FIGURE 3.0.7– EFFECT OF INCREASED FUEL FRACTION ON TOTAL VEHICULAR WEIGHT	42
FIGURE 3.0.8 – EFFECT OF INCREASED FUEL ON TOTAL VEHICULAR WEIGHT [HASA]	42
FIGURE 4.0.1 – RAMJET STATIONS NUMBERED [52].....	45
FIGURE 4.0.2 – OPTIMAL FEASIBLE DESIGN SPACE.....	47
FIGURE 4.0.3 – SPECIFIC FUEL CONSUMPTION VERSUS SPECIFIC THRUST	48
FIGURE 4.0.4 – SPECIFIC IMPULSE VERSUS SPECIFIC THRUST	48
FIGURE 4.0.5 – RAMJET DESIGN POINT BASED ON SPECIFIC THRUST, SPECIFIC FUEL CONSUMPTION AND OVERALL EFFICIENCY	49
FIGURE 4.0.6– SCRAMJET DESIGN POINT BASED ON SPECIFIC THRUST, SPECIFIC FUEL CONSUMPTION & OVERALL EFFICIENCY	51
FIGURE 4.0.7 – EXPANSION RATIO VERSUS COEFFICIENT OF THRUST	53
FIGURE 4.0.8 – EXPANSION RATIO VERSUS CHARACTERISTIC VELOCITY	54
FIGURE 4.0.9 – DESIGN POINT FOR ROCKET ENGINE FROM COEFFICIENT OF THRUST, CHARACTERISTIC VELOCITY AND SPECIFIC IMPULSE ...	54
FIGURE 5.0.1– THETA-BETA-MACH DIAGRAM [50]	58
FIGURE 5.0.2 – PART OF THE NORMAL SHOCK PROPERTIES [51]	59
FIGURE 5.0.3 - GENERAL VARIABLES AND CALCULATIONS FOR METHOD OF CHARACTERISTICS.....	61
FIGURE 5.0.4– CONTOUR OF THE NOZZLE AT THE DESIRED MACH NUMBER.....	62
FIGURE 5.0.5 - PARABOLIC NOZZLE RELATIONS	62
FIGURE 5.0.6 – LEFT VIEW OF THE PROPOSED MODEL.....	65
FIGURE 5.0.7 – REAR VIEW OF THE PROPOSED MODEL.....	65
FIGURE 5.0.8 – FRONT VIEW OF THE PROPOSED MODEL	65
FIGURE 5.0.9 – CUT VIEW OF THE PROPOSED MODEL	66
FIGURE 6.0.1 - AEROSPIKE CONTOUR USING METHOD OF CHARACTERISTICS	69
FIGURE 6.0.2 - DIMENSION OF LINEAR AEROSPIKE.....	70

FIGURE 6.0.3 - BACK VIEW OF THE LINEAR AEROSPIKE	71
FIGURE 6.0.4 - ISOMETRIC VIEW OF THE COMBUSTION CHAMBER WITH THE PRECOOLER	72
FIGURE 6.0.5 - FRONT VIEW OF THE COMBUSTION CHAMBER	72
FIGURE 6.0.7 - ISOMETRIC VIEW OF THE INLET CONE	73
FIGURE 6.0.6 - DIMENSIONS FOR THE INLET CONE.....	73
FIGURE 6.0.8 – ISOMETRIC VIEW OF AEROSPIKE.....	74
FIGURE 6.0.9 – SLICED VIEW OF THE PROPOSED MODEL	74
FIGURE 6.0.10 - MESH GRID FOR LINEAR AEROSPIKE AND NOZZLE	78
FIGURE 6.0.11 - MESH GRID FOR THE INLET CONE AND RAMPS.....	80
FIGURE 6.0.12 - CONTOUR OF MACH AT SEA-LEVEL.....	82
FIGURE 6.0.13 - CONTOUR OF MACH AT DESIGN ALTITUDE	83
FIGURE 6.0.14 - CONTOUR OF TOTAL PRESSURE AT SEA-LEVEL.....	83
FIGURE 6.0.15 - CONTOUR OF TOTAL PRESSURE AT DESIGN ALTITUDE	84
FIGURE 6.0.16 - CONTOUR OF TURBULENT KINETIC ENERGY AT SEA-LEVEL	84
FIGURE 6.0.17 - CONTOUR OF TURBULENT KINETIC ENERGY AT DESIGN ALTITUDE.....	85
FIGURE 6.0.18 - CONTOUR OF MACH AT SEA-LEVEL.....	86
FIGURE 6.0.19 - CONTOUR OF MACH AT DESIGN ALTITUDE	86
FIGURE 6.0.20 - CONTOUR OF TOTAL PRESSURE AT SEA-LEVEL.....	87
FIGURE 6.0.21 - CONTOUR OF TOTAL PRESSURE AT DESIGN ALTITUDE	87
FIGURE 6.0.22 - CONTOUR OF TOTAL TEMPERATURE AT SEA-LEVEL	88
FIGURE 6.23 - CONTOUR OF TOTAL TEMPERATURE AT DESIGN ALTITUDE.....	88
FIGURE 7.0.1 – ORBITAL TRAJECTORY FOR A HOHMANN TRANSFER	91
FIGURE 7.0.2 – FIGURE EIGHT TRAJECTORY FROM TWO TRANSFER ELLIPSES AND ONE CIRCULAR ORBIT.....	92

NOMENCLATURE

Symbol	Definition
P_e	exit pressure
P_a	ambient pressure
F_T	thrust force
ρ	density
\dot{m}	mass flow rate
A_e	exit area
\vec{V}_e, c	exit velocity
T	temperature
a	speed of sound
MFP	mass flow parameter
γ	specific heat ratio of air
C_p	specific heat at constant pressure
C_v	specific heat at constant volume
t	time
e	energy
\dot{Q}, \dot{q}	heat with respect to time
\dot{W}	work with respect to time
P	power
P, p	pressure
RBCC	rocket based combined cycle
MDO	multi-objective design optimization
GSA	global sensitivity analysis

Symbol	Definition
LEO	low earth orbit
GTO	geosynchronous transfer orbit
ISS	international space station
NASA	National Aeronautics and Space Administration
JAXA	Japanese Aerospace Exploration Agency
CFD	computational fluid dynamics
RLV - TD	reusable launch vehicle - technology demonstrator
TPS	thermal protection system
GNC	guidance, navigation and control
DAB	diffusion and afterburning
SMC	simultaneous mixing and combustion
WIRES	winged reusable sounding rockets
ISRO	Indian Space Research Organization
I_{sp}	specific impulse
g	earth's gravitational acceleration
SLS	space launch system
$\frac{T}{W}$	thrust to weight ratio
ΔV	delta V burn /change in velocity
F_T	thrust force
m_o	initial mass
m_f	final mass
m_F	fuel mass

Symbol	Definition
SABRE	synergetic air-breathing rocket engine
LLO	low lunar orbit
τ_r	temperature ratio from freestream to inlet
τ_b	temperature ratio from end of compressor to end of combustion
τ_c	temperature ratio from end of inlet to end of compressor
f	mass flow over mass fuel ratio
τ_{xy}, τ_{yz}	tangential stress in the x-direction
τ_{yx}, τ_{yz}	tangential stress in the y-direction
τ_{zx}, τ_{zy}	tangential stress in the z-direction
u	x component of the velocity vector
w	z component of the velocity vector
r_p	radius at perigee
G	gravitational constant
V_{circp}	velocity of circular orbit at perigee
θ	angle in degrees
R_t	turbulence Reynolds number
A^*	nozzle throat area
M	Mach number
r_a	apogee radius
n	mass ratio
a'	semi-major axis
LOI	lunar orbit insertion
MCC	midcourse correction
R_E	radius of earth

Symbol	Definition
CAD	computer aided design
η_o	overall engine efficiency
η_c	engine cycle efficiency
η_p	propulsive efficiency
h_{pr}	enthalpy of products
τ_λ	temperature ratio from end of combustion chamber to freestream
τ_{xx}	normal stress in the x-direction
τ_{yy}	normal stress in the y-direction
τ_{zz}	normal stress in the z-direction
v	y component of the velocity vector
k	thermal conductivity
r_a	radius at apogee
M'	mass of the heavenly body
V_{circa}	velocity of circular orbit at apogee
R_{th}	radius at the nozzle throat
L_N	nozzle length
A_i	inlet's capture area
V_θ	tangential velocity
r_p	perigee radius
Δi	change in inclination
TLI	trans-lunar insertion
TEI	trans-earth insertion
r_{Lpm}	lunar radius of perigee for return trajectory
ε'	structural ratio

Symbol	Definition
π', λ	payload ratio
c^*	characteristic velocity
ε	expansion ratio
W	weight
E_{ltr}	endurance loiter
η_{vol}	volumetric efficiency
k_b	calibration constant
V_{tot}	total volume
D_{bc}	diameter of fuselage
M_{ff}	mass fuel fraction
F_r	fineness ratio
θ_f	forward cone half angle
Λ	ratio of body length to body radius
W_{sub}	subsystem weight
W_{pay}	payload weight
TTOT	total take-off weight
T_{cf}	temperature correction factor
L_{TR}	total ramp length
W_{fuel}	fuel weight
W_{IVR}	inlet variable ramp weight
P_o	ambient pressure
Q_{in}	energy input
ν_t	turbulence number

Symbol	Definition
d	distance
C_F	coefficient of thrust
M_n	Mach number of normal component
R_{cr}	cruise range
HASA	hypersonic aerospace sizing analysis
k_n	ratio of body depth/width
k_c	calibration constant for non-idealized body
L_b	body length
L/D	lift to drag ratio
GTOW	gross take-off weight
B_b	body diameter
θ_r	aft cone half angle
S_{tot}	total surface area
W_{str}	structures weight
N_{engr}	number of rocket engines
WC	weight coefficients
A_{TC}	total capture area at inlet
n	number of inlets
W_{prop}	propulsion weight
M_o	initial Mach number
T_o	ambient temperature
ε_{DR}	dissipation rate
k'	eddy viscosity turbulence

$C_{\mu},$ $C_{\varepsilon dr1},$ $C_{\varepsilon dr2}$	turbulence model constants
\bar{U}, u	mean and fluctuating velocity components in x-direction
y^+	dimensionless distance from the wall

f_{μ}, f_1, f_2	turbulence model functions
$\sigma_k, \sigma_{\varepsilon}$	turbulence model constants for diffusion of k and ε

Chapter 1 – Introduction

1.1 Motivation

John F. Kennedy who challenged American scientists, engineers and astronauts in the 1960s, led to the birth of Apollo 11, Space Shuttle, International Space Station (ISS), Hubble telescope, Voyager, Sojourner and many more groundbreaking inventions. Regardless of such engineering developments, manned missions to space diminished drastically. In fact, it has been nearly fifty years since an American astronaut walked on the moon. So why do these contradicting patterns occur? The simple answer to this complex question is cost. Before SpaceX, each unmanned mission to space easily surpassed \$100 million in overall expense. However, as private company owners such as Elon Musk and Jeff Bezos stepped into the industry, the race to space was re-ignited. Furthermore, the launch cost for unmanned space missions dwindled down to \$62 million and spaceflights with astronauts lowered to \$140 million [1].

Inspired by these successes, international and domestic investors see space tourism as a future capitalistic revenue. SpaceX has initiated designing Starship, a spaceplane with 100-passenger capacity that allow civilians to travel to LEO [2]. Challenging Starship, Blue Origin has also established designs for New Shepard. In the span of ten minutes, New Shepard is engineered to travel passed the Karman line with payload and large viewing windows for customers to observe during the flight. Unlike the Space Shuttle, New Shepard is built for vertical take-off and vertical landing [4]. Boeing's CST-100 Starliner is yet another candidate for space tourism however due to some testing discrepancies, Boeing's progress has been delayed [5]. Currently, Starliner is striving to successfully transport NASA astronauts to ISS with maximum capacity of seven crew members, two of which can be converted as payload bay [6]. Once they have achieved official certification from NASA, Boeing aspires to promote space tourism with a fully autonomous Starliner. Although, SpaceX, Blue Origin, and Boeing are not the only private companies investing in this endeavor. Michael Colglazier, CEO of Virgin Galactic launched SpaceShipTwo for the sole purpose of space tourism. However, due to some unforeseen circumstances, one of the test flights resulted in a crash and death of one pilot [11]. Regardless, Virgin Galactic continued to refine and improve the SpaceShipTwo design until the updated version, Unity 22, made its first maiden flight on July 11th, 2021 [56].

All the progress discussed so far only incorporates domestic developments; however, space tourism fever has reached international levels. For instance, the European Union successfully launched Intermediate Experimental Vehicle (IXV) in 2015 with sensitive infrared cameras and thermocouples installed on the wing [7]. During its early stages, the model was tested through Computational Fluid Dynamics (CFD) on its autonomous lifting and aerodynamically controlled capabilities [8]. From the actual flight, the engineers were able to corroborate some of the simulated results along with discovering areas that still need improvement before they can venture into capitalizing space. JAXA (Japanese Aerospace Exploration Agency) released the robotic test bed which enables the reuse of suborbital spaceplane. The Winged Reusable Sounding Rocket (WIRES) was expected to launch in the year 2020; however, due to unexpected delays, the deadlines were not met [9]. In conjunction with Japan's progress, Indian Space Research Organization (ISRO) tested their version of a Reusable Launch Vehicle-Technology Demonstrator (RLV-TD) which endorsed their autonomous Guidance, Navigation, and Control (GNC) system, reusable Thermal Protection System (TPS), and re-entry mission management [10]. There are other countries such as Russia and China who have also successfully tested and developed hypersonic missiles and aircrafts in recent years. Therefore, it is safe to conclude the increase in feasibility of space tourism and its viable benefits for commercialization in the past few years. These macroscopic advancements could not be plausible without an effective propulsion system that possess' vital attributes such as: reusability, design simplicity, economical, consistency in contradicting atmospheres and achievement of a speed regime from static to hypersonic. Based on all the current existing propulsion systems, there is no comprehensive rocket engine that carries all these attributes to be classified as an ideal engine. Regardless, few successful designs were able to provide solutions to some of these challenges.

1.2 Literature Review

Desire for space exploration and knowledge led many researchers to hypothesize an array of designs for high performance propulsion systems. There are multiple types of propulsion systems that achieve the greatest performance in specific environments. However, for space travel, the propulsion system is exposed to a range of velocities, atmospheric pressure, temperatures, and densities. Former rocket engines were able to accomplish this feat with

remedial and limited technologies. As 20th century technology exceeds expectations, hybrid propulsion systems are more viable alternative solutions for this dilemma. This is evident in propulsion systems such as turboramjets and rocket based combined cycles.

1.2.1 Chemical Rockets with liquid propellants only

Throughout the history of space travel, chemical rockets are the most dominant form of the propulsion system. Since these rockets have a rich flight heritage, researchers have developed two variants: monopropellant and bipropellant. As the name suggests, monopropellant engines only carry one fuel whereas bipropellant engines have two: an oxidizer and a fuel. Even though both types of propellant stem from the original chemical rocket design, they have individual benefits and drawbacks. Monopropellant rockets generally have simple and robust designs, are reliable, can manually be shut down, and are more commonly employed [26]. However, most of the fuels for monopropellant rockets are dangerous. Plus, only utilizing one fuel lowers the amount of thrust and exhaust speeds generated by this rocket. The catalyst included in the propulsion system also generate limited lifespan. Figure 1.1 is a basic configuration of a monopropellant rocket.

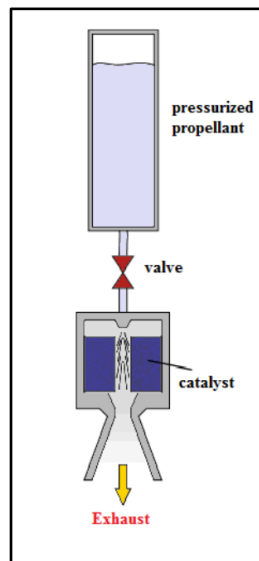


Figure 1.0.1 – General schematic of a monopropellant engine

On the other hand, bipropellant rockets have their own set of merits and demerits. For instance, these engines have more efficiency than hybrid or solid rockets. Since there are two

propellants, this system also has higher exhaust velocity ranging from (3.6-4.4 km/s) [27]. Similar to monopropellant, these rockets have lots of flight time in space and can be turned off. Another merit for this type of engine is the ability to throttle. This feature permits the spacecraft to control the thrust force and maximize fuel consumption. Nevertheless, some demerits of bipropellant rockets stem from the complexity of its design. Since two propellants are utilized in this system, separately stored pressurized tanks along with extra valves and pumps are required. Bipropellant rockets also endure icing issues which necessitates the requirement for cryogenic system [26]. The addition of cryogenic system also contributes to the overall gross weight. Figure 1.2 displays a generic scheme of bipropellant rocket engine.

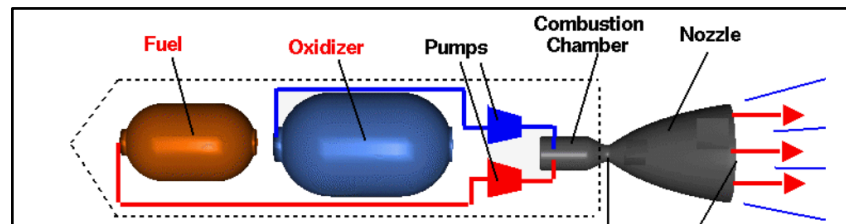


Figure 1.0.2 – General schematic of a bipropellant engine

1.2.2 Hybrid Chemical Rockets

Typically, a hybrid rocket is a combination of solid and liquid propellants designed into one propulsion system. Some of the advantages of this type of rocket propulsion include safety, cost effective, reliability, and simpler design. Due to the inert quality of solid propellants, hybrid rockets are easier to store, manufacture, transport and operate on a rocket engine [21]. Comparatively, solid-liquid propellant has reduced chances of explosion and can produce equally high specific impulse as a chemical rocket. Hybrid propulsion systems require less turbopumps which reduces the gross take-off weight and simplify the design [20]. Generally solid propellants are cheaper to manufacture and produce than the liquid oxidizer and fuel. Since the hybrid propulsion requires fewer liquid propellants, the cost is significantly lowered. Once the solid rocket is ignited the propellant will undeniably combust. Therefore, the reliability of this propulsion system is consistent. Additionally, the counter-balancing effect of hybrids permit regression rate not to be affected by choice of propellants [18]. A popular example of a hybrid rocket is the Spaceship One's propulsion system. Burt Rutan, the chief designer of SpaceshipOne, selected rubber and nitrous oxide as the solid and liquid propellant, respectively

[19]. Nearly 250 seconds of specific impulse at vacuum and 75,000 N of thrust was achieved by this spacecraft [23]. Figure 1.3 depicted below provide examples for various types of hybrid propulsion systems.

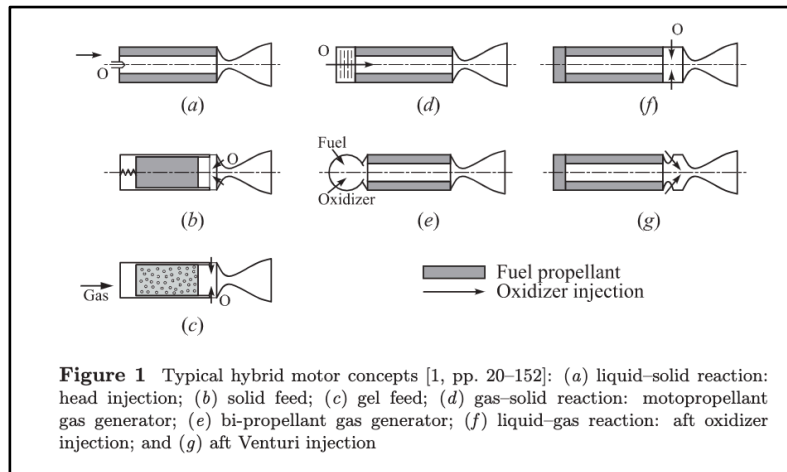


Figure 1.0.3 – Examples of different hybrid motors

Regardless of all the overcoming benefits, disadvantages of hybrid rockets are still present today. Even if the oxidizer’s mass flow rate is held constant, the mixture ratio shifts as the hybrid motor is burning through the solid propellant. This leads to inconsistent specific impulse and lowers the overall thrust force. However, at peak performance, if the hybrid rocket is exceptionally designed then specific impulse will not be affected by the mixture ratio. Additionally, liquids and solid propulsion systems have better combustion efficiencies than hybrids which range from 0.93 to 0.97 [22]. Most hybrids have a larger volume than solid propellants. During ignition, large slivers of solid propellant are leftover due to low density specific impulse. Low regression rates from fuel grain geometry are another major complication of a hybrid propulsion system. There is a larger disparity between a powerful solid propellant and a hybrid rocket’s regression rates. In specific conditions, these rockets develop pressure oscillations that lead to twice the pressure in the operating motor [22]. Unlike liquid propellants, refueling solid propellants is not easy, especially in hybrid rockets. Nonetheless, this issue can be resolved by designing the system for easy replacement of the solid rocket propellants. Even though some of these issues can be surpassed, the range of specific impulse for this type of propulsion system is limited. Usually, hybrids have higher impulse values than a solid propellant

but lower than liquid propellants. Currently, the highest fuel consumption efficiency a hybrid rocket can achieve is about 400 seconds [24].

1.2.3 Airbreathing Hybrid Engines

Amidst the different propulsion systems present today, one distinguished engine produced by Reactions Engine Limited successfully overcame many challenges presented in this paper. The Synergetic Air Breathing Rocket Engine founded by Alan Bond, John Scott-Scott, and Richard Varvill showcases the greatest potential for space engines. This is validated with a projected thrust-to-weight ratio of 14, the highest value presented by any present day theoretical and existing engines. Another distinct feature of this engine is the groundbreaking precooler which is capable of cooling incoming flow from 1000°C to -150°C [15]. Precooler's feature was successfully tested in a Colorado facility, under Mach 5 conditions [16]. Moreover, this innovative precooler can collect and store oxidizer while traversing through supersonic speeds and higher altitudes. Since this design fuses rocket and air breathing components into a synchronized engine, the complexity of the design should increase. However, compared to a turboramjet or a general gas turbine, the overall weight is less. This reduction results from less propellant on board during launch, and extensively fewer mechanical apparatus required for the air-breathing section. As a result, the overall cost dwindles to affordable ranges and increases the reusability of this engine. Figure 1.4 provides a blueprint of the proposed Synergetic Air Breathing Rocket Engine.

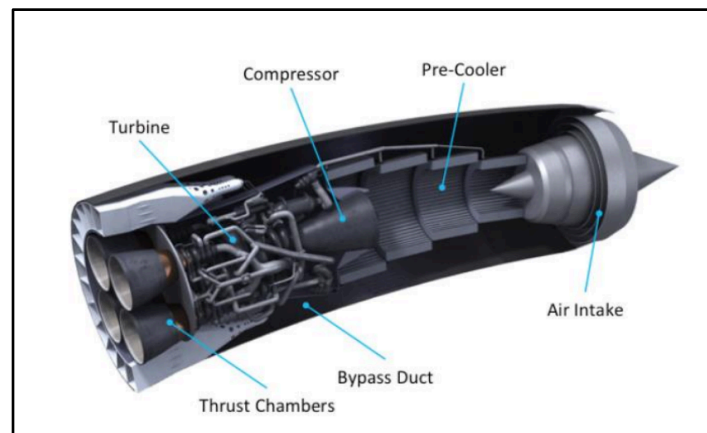


Figure 1.0.4 – Basic layout of SABRE engine

Despite such raving achievements, SABRE design still lacks a few desired qualities for a space engine. For instance, once this engine enters space all the air-breathing components, including the precooler, is rendered obsolete as there is no air to compress or oxygen to create oxidizer. As a result, the useful payload decreases, and more propellant is required to achieve greater distance. Skylon's D1 configuration, a spaceplane that employs SABRE engines, is predicted to travel utmost to the Geosynchronous Transfer Orbit with 34,000lbs of payload [17]. Plus, the choice of rocket for SABRE design is a chemical rocket. As discussed previously, the specific impulse and thrust is constrained by the chemical reactions of the fuel and oxidizer. In other words, a specific impulse will not exceed 600 secs since thrust force is limited by two primary factors: amount of propellant and mass flow rate of the nozzle [28]. Besides, if SABRE is selected for space travel, the engine must regulate at specific temperatures and pressures depending on the length of exposure to the space environment. This would increase design complexity and hence add to the overall gross take-off weight, especially if heat and radiation shields must be included. Even though the precooler's abilities were tested and proved, the completed engine has not been validated in actual flight conditions or attained actual flight hours. In non-ideal or realistic environments, some of the expected values deplete or new issues arise that was not encountered in limited simulation tests. Thus, the promised performance of the SABRE engine is still uncertain.

1.2.4 Rocket Based Combined Cycle (RBCC)

The novelty of this hybrid design renders its own unique capabilities and setbacks. Advantages of RBCC engine proclaim better flexibility and efficiency than traditional rocket engines and increase reusability of space launch systems. Due to airbreathing components embedded in the rocket engine, oxidizer is not required during launch which effectively reduces total mass and increases useful payload mass [13]. This innovative design integrates the high thrust-to-weight ratio of a rocket while generating high specific impulse of air breathing engines. Furthermore, the multi-modal operations of a RBCC engine facilitate transitions between each mode which propel the craft through various altitudes, speeds, and pressures [12]. Conventional prototypes of a RBCC engine reserve four unique modes: ejector, ramjet, scramjet, and rocket mode. Ejector mode is a unique feature which utilizes primary flow by a rocket to produce sufficient thrust to propel from sea-level at static conditions [14]. Flight regime for this mode is

estimated to be from Mach 0 to Mach 4 [13]. Efficiency of a RBCC engine depends heavily on the ejector mode [12]. On the contrary, ramjet mode functions from Mach 2 to 8 while scramjet mode functions at Mach 4 to 12 [13]. Both modes are characterized by formation of oblique shock waves which compress air without heavy machinery. Most RBCC design incorporates an inlet, ramp, strut, mixer, primary and secondary injectors, combustion chamber and a rocket nozzle [14]. Additionally, inclusion of these two modes permit the engine to produce and utilize oxidizer from compressed air, reducing both propellant weight and overall take-off weight. In rocket mode, the inlet is closed allowing the engine to operate nominally in environments with less or no air. Anything greater than Mach 12 is operational in rocket mode [13]. Speed regimes overlap, during which multiple facets are involved to improve the interactions between each mode. Figure 1.5 provides a general diagram of RBCC engine's four common modes.

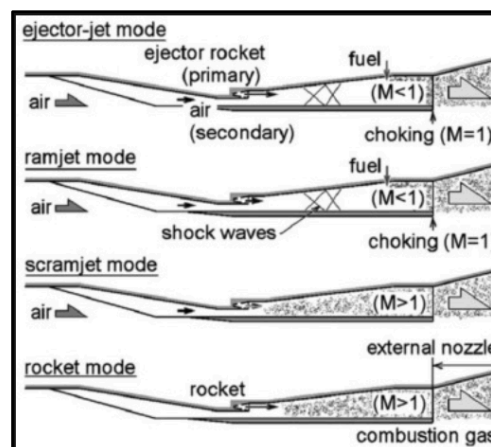


Figure 1.0.5 – Four basic modes of a RBCC

Regardless, there are multiple constraining factors like high entrainment and compression ratios that prevent feasible prototypes from being pursued. Different modes have their own challenges. For instance, ejector mode is considered by a few to be the most essential phase of a RBCC engine. Along with initial thrust, this mode majorly effects the performance parameters of the overall propulsion system. However, few areas of the ejector mode still have challenges to overcome. Improvement areas include combustion organization, mixing efficiency, backpressure resistance and efficiency in mode transitions. Combustion organization indicates an increase in both combustion and thermodynamic cycle efficiencies which promote greater reduction in weight, and complexity of engine design. Future studies focus on optimization of Diffusion and

Afterburning (DAB) and Simultaneous Mixing and Combustion (SMC) modes for effective combustion organization. DAB and SMC only represent one out of four modes available for an ejector phase. Therefore, experimenting on other pair of modes could optimize the ejector mode. Likewise, there is evidence of positive effect of enhanced geometric configuration on combustion organization. Mixing enhancement is depicted by rapid and sufficient diffusion of primary and secondary flows. Current research involves growth characteristics and mixing enhancement mechanisms of confined reactive supersonic mixing layer with complex shock-wave structures. Another pivotal aspect of the ejector mode is the ability to resist backpressure build up as this could lead to inlet unstart. Studies on RBCC configuration, mixing and combustion processes for primary and secondary flows analyze key factors that could optimize backpressure resistance. Transition from ejector to ramjet mode also possess unknown challenges. These can be assessed through sufficient flight tests on multi-modal operational capabilities. Based on current research, smooth mode transitions are influenced by variable thrust, geometry of variable inlet or nozzle and optimized secondary fuel injection [12].

1.3 Project Proposal

In recent years, the explosion for space technology resurfaced many experimental and unique ideas for space travel. Among these ideas, is an air breathing rocket engine that can transport a space plane from static to hypersonic speeds with less fuel. Nonetheless, only recently have designs evolved from CAD drawings to prototype versions. There are still many challenges that prevent the feasibility of such an engine to be possible. In particular, the SABRE engine is a design which has solved most of the challenges for an airbreathing rocket engine. However, this engine has yet to prove its efficiency during mode transitions and contain non-compatible components in space. Therefore, the main objective of this project is to design a horizontal take-off and landing rocket engine that has similar capabilities to the SABRE engine. Regardless, few unique design features proposed in this project include optimizing the nozzle, proposing a new inlet design, redesigning SABRE engine's combustion chamber, and increasing rocket engine capabilities. Plus, this model will be designed for recurring manned or unmanned missions to the moon.

Presently, to test a hypersonic engine design requires a lab or wind tunnel with unique facilities. Even today, there is no established supersonic or hypersonic wind tunnels that can

simulate and withstand re-entry velocities, temperatures, and pressures. Besides, testing in such a wind tunnel will drive up the cost. Therefore, the best cost-effective method to test the performance of a hypersonic engine will be through Computational Fluid Dynamics (CFD) analysis. The model will be tested in specific speed regimes to verify the efficiency of each mode and examine the parameters during crucial mode transitions.

1.4 Methodology

There are two major phases for this project. Part 1 is the preliminary design process before generating the CAD model. Primarily, general trade studies will be executed from the mission specification and historical trends. Secondly, through Multi-objective Design Optimization process, most of the design constraints, points and important performance parameters will be derived. Specifically, the Global Sensitivity Analysis (GSA) will be pursued for the specific propulsion system in consideration. This optimization method will provide the critical parameters that effect the subsystems of the selected rocket system. Finally, an optimized CAD design will be generated in Fluent Ansys.

Part 2 is the post design study of the proposed engine. This phase is initiated when the governing equations from Navier Stokes is derived. After the appropriate equations are achieved, a specific turbulent theory will be selected for the CFD simulation on the CAD model. Once the simulation is conducted, a parametric study of the essential performance factors can be accomplished. The validity of the simulation can be verified from previously implemented experiments. Once all the data has been assembled, analysis on future research can be observed. Furthermore, depending on the accuracy of the generated CFD simulation, constraints of the conducted tests can be established as well as providing better solutions for those issues. Toward the end of the paper, an overall summary will be generated regarding all the findings and concerns of this design process.

1.5 Chapter Overview

Each chapter specifies one aspect of the design process. The chapters are organized into an outline as follows:

Chapter 1 consists of the motivation for this design. This is further solidified with the literary review of all the current technology and developments in rocket propulsion. Thereafter,

the proposed design and a methodology are established for this research paper. Towards the end, a proposition of the general layout for this design process is also accomplished.

Chapter 2 will establish the detailed mission objective for this design process. Once the objective is declared, performance parameters of formerly established airbreathing rockets will be stated from historical data. However only the data from similar engines will be considered to provide an approximate design space.

Chapter 3 will focus on basic trade studies from all the historical data observed from chapter 2. From these studies, few of the sensitivity parameters can be detected and analyzed. Additionally, the amount of effect of one parameter on another can also be established from the trends populated by the graphs.

Chapter 4 will highlight the process of MDO, and the proper values selected for this engine. Results from this optimization method will generate the approximate design points and disclose the coupled parameters of the proposed engines.

Chapter 5 is the summary of all the data analyzed from previous chapters. The CAD model will incorporate specifications on length and geometric configurations. This model will also implement the unique features for this airbreathing engine.

Chapter 6 will implement changes to the proposed model to optimize the performance further. Once the revisions are made, dimensions from the new CAD models will be utilized for running a 2D simulation in Ansys. Furthermore, derivations of the turbulent model from Navier Stokes equations will provide a better understanding of some of the CFD choices. Basic settings for mesh and solution modules of the simulation package will be displayed. All the results from CFD simulations will then be discussed here. This will reveal all the limitations and discrepancies of the testing method. From the limitations of the simulation or turbulent theory models, future work can be proposed.

Chapter 7 will emphasize on the orbital trajectories and the necessary delta V burns required for this mission. Furthermore, the amount of total fuel tabulated will provide an assessment of storage space for fuel tanks. These values will be compared to established lunar missions for gauging the validity of the acquired results.

Chapter 8 will analyze the optimal and minimum staging levels required to input useful payload at the desired orbits. Once all the calculations are derived, a summary table will provide the overall results attained from this chapter.

Chapter 2 – Mission Specifications and Comparative Studies

2.1 Mission Objective

Bia LII is a proposed engine design for hybrid launch vehicles. The main intention of this engine is to decrease the overall fuel weight during take-off and maintain thrust in contradictory environments. This propulsion system is designed to take civilians in a flyby trajectory around the moon. Therefore, a payload of 10 passengers with 230lbs of cargo each and 2 crew members with 150lbs of baggage is incorporated into design considerations. In-depth mission specification requirements are listed in table 2.1 below.

Table 2.0.1 – Detailed summary of mission objectives for the proposed engine

Parameter	Description / Value
Payload Capacity	10 Passengers with 230lbs of baggage each
Crew	2 Astronauts with 150lbs of baggage each
Range	9844 nm
Cruise Speed	16668.47 kts (knots)
Mach Number	0 to 25
Endurance	30 mins
Cruise Altitude	80,000ft and 140,000ft
Main Destination	Lunar Flyby

2.1.1 Mission Profile

Unlike most launch vehicles, Bai LII is designed for horizontal take-off. Most of the flight for this launch vehicle will be in space however some stages will be within the earth's atmosphere. Since both earth and space environments are governed by different forces, this engine will have two primary stages. Initial stage of the engine will resemble a simple aircraft mission profile. Conversely, once the spacecraft travels beyond the earth's atmosphere, the mission profile will be governed by orbital trajectories. Figures 2.1 and 2.2 depict the earth and space mission profiles, respectively.

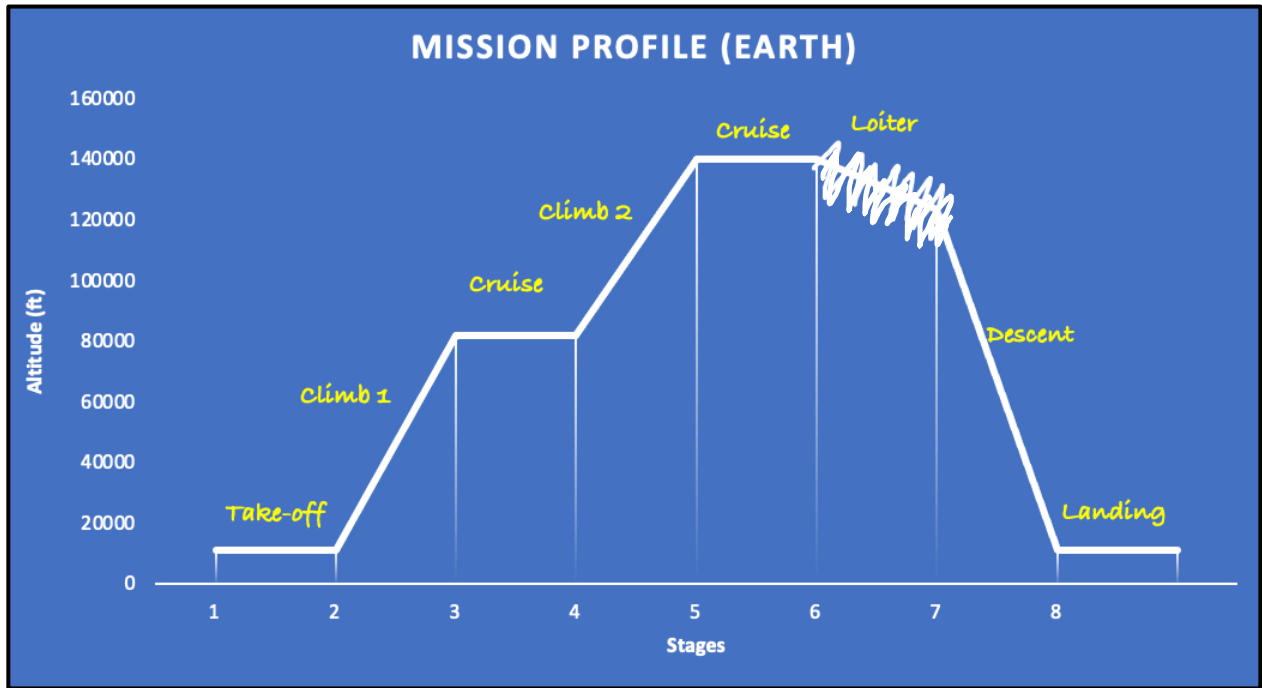


Figure 2.0.1 – Mission profile within Earth’s atmosphere

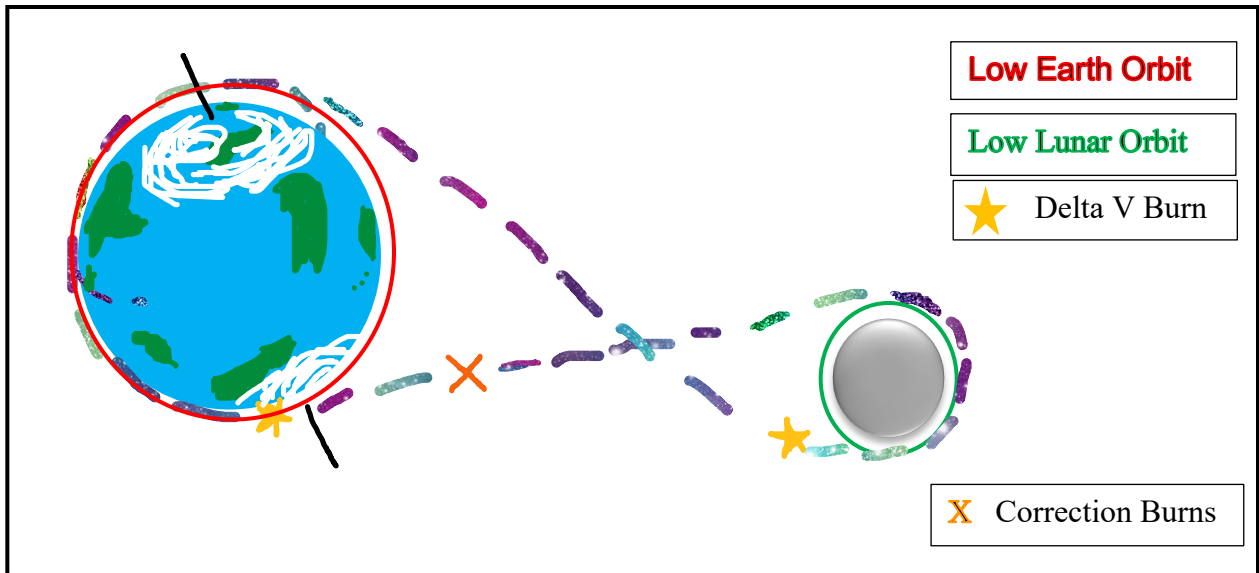


Figure 2.0.2 – Orbital trajectory of lunar flyby

2.1.2 Critical Mission Requirements

Bai LII is a proposed design of an integrated launch vehicle with horizontal take-off and landing capabilities for a lunar flyby. Such a long-distance travel in space is heavily depended on

fuel capacity and various performance parameters of the engine. Furthermore, to make a hybrid engine have consistent performance in various atmospheres, an addition of highly advanced technology must be incorporated into the design. This will increase overall weight of the spacecraft which has direct correlation to fuel weight. The key parameters listed below are separated by environments they are most effective in.

Table 2.0.2 – Key engine parameters in their respective environments

Location	Parameters		
Earth	$\frac{T}{\bar{W}}$		
Space	I_{sp}	ΔV	
Both	F_T	η_p	m_F

2.2 Comparative Study

Due to innovative aspects of this design, there are limited engines that are available for an accurate comparison. To conduct a decent comparison, a mixture of rockets and hybrid aircraft engines are included in this study. From this study, typical engine configurations and engine locations can be observed.

2.2.1 Engine Configuration Selection

- SNECMA Atar 09C turbojet with SEPR 841 rocket engine

This hybrid engine was the main propulsion system for the Dassault Mirage III. Dassault is a fighter jet and the first European aircraft to achieve Mach speed greater than 2 in horizontal flight. Atar 09C is a nine-stage axial compressor with two stage turbine [29]. On the other hand, SEPR 841 was a portable pod that could be mounted on Mirage III anytime. Due to high specific fuel consumption and large center of gravity changes, the oxidizer tank was placed in front of the rocket engine while fuel tanks were located behind the cockpit [30].



Figure 2.0.3 – Bottom view of the turbojet and rocket engine installment

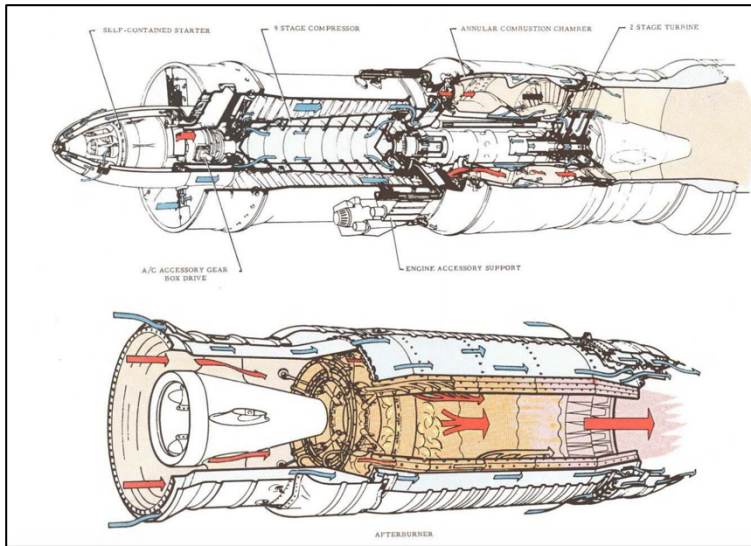


Figure 2.4 – Schematic diagram of SNECMA Atar 09C

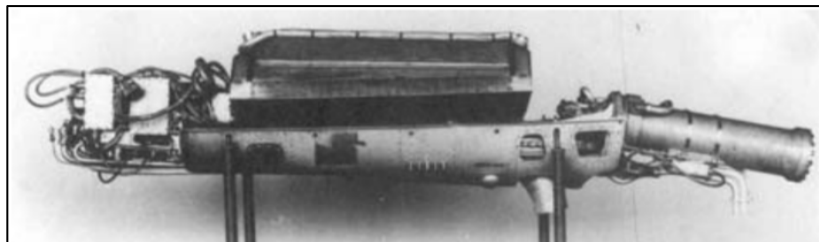


Figure 2.0.5 – Schematic diagram of variant of SEPR 841

- SpaceDev Rocket Engine

SpaceShipOne was a suborbital spacecraft with the oxidizer tank as the main structural component of the fuselage. This spacecraft was equipped with a SpaceDev engine fueled with hydroxyl-terminated polybutadiene and nitrous oxide [32]. Although this spacecraft is technically a chemical rocket, solid fuels behave differently from their liquid counterparts. The greatest speed achieved with SpaceDev engine was 900 m/s in Mach 3.3 [32].



Figure 2.0.6 – Top view of SpaceShipOne with rocket nozzle

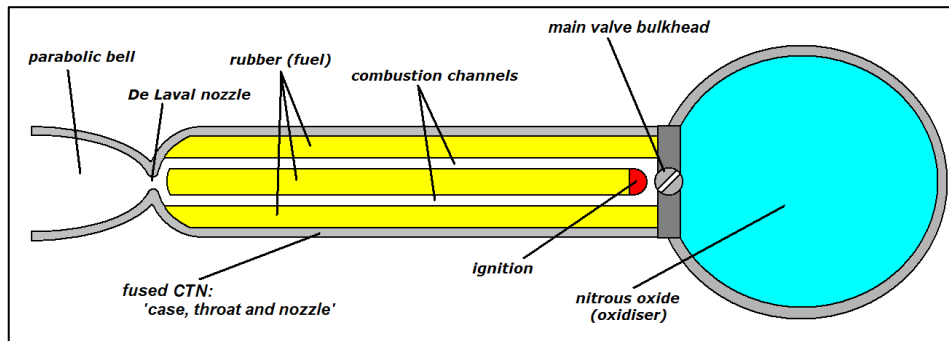


Figure 2.0.7 – Basic layout of the hybrid engine for SpaceShipOne

- Turbomeca Gabizo turbojet with SEPR 631

This engine was developed for SNCASO Trident II, a French interceptor aircraft. The turbojet component is a single stage axial compressor and turbine. Along with the centrifugal compressor, Turbomeca has only one annular combustion chamber [31]. SEPR 631 have two thrust chambers that can be ignited independently from each other. Due to this engine's automated shut down and ignition processes, the aircraft's instrumentation is simplified [33].



Figure 2.0.8 – Trident II with Turbomeca Gabizo and SEPR 631 engine

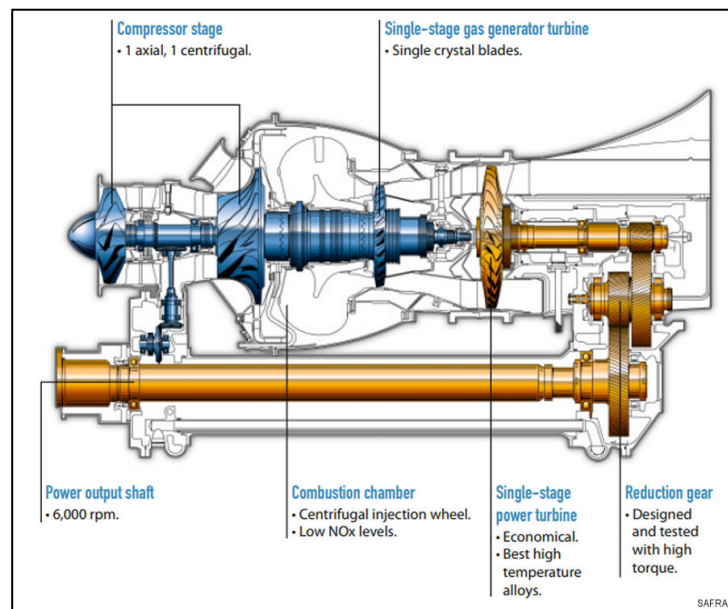


Figure 2.0.9 – Schematic layout of Turbomeca variant

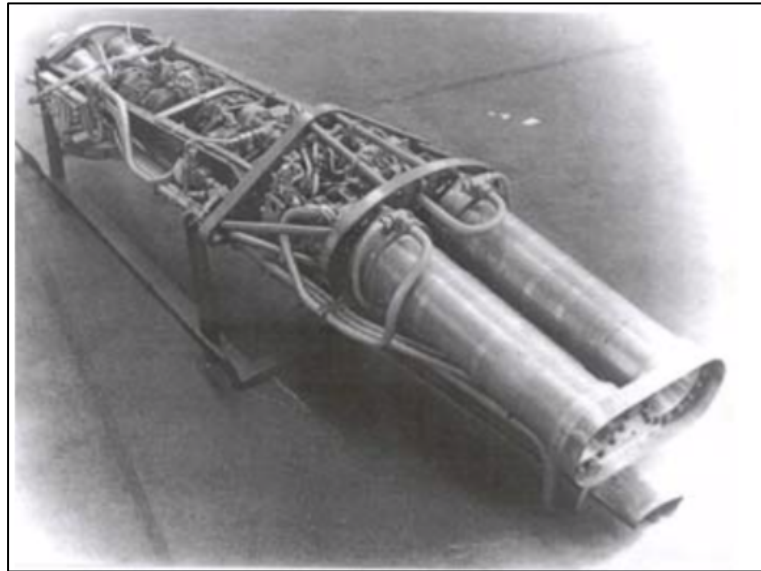


Figure 2.0.10 – Top view of SEPR 631 engine

- Pratt and Whitney J-58 Turboramjet

Lockheed designed J-58 engines for the SR-71 Blackbird. Even though this aircraft was built in early 60s, Blackbird is still one of the fastest reconnaissance aircraft in the world. The turboramjet is equipped with nine-stage axial compressor and two-stage axial turbine [54]. Additionally, the engine is also installed with afterburners to generate enough thrust during take-off. One of its unique features is the variable inlet and forward bypass doors. Top speeds of the Blackbird reached beyond Mach 3.



Figure 2.0.11 – SR-71 Blackbird in flight

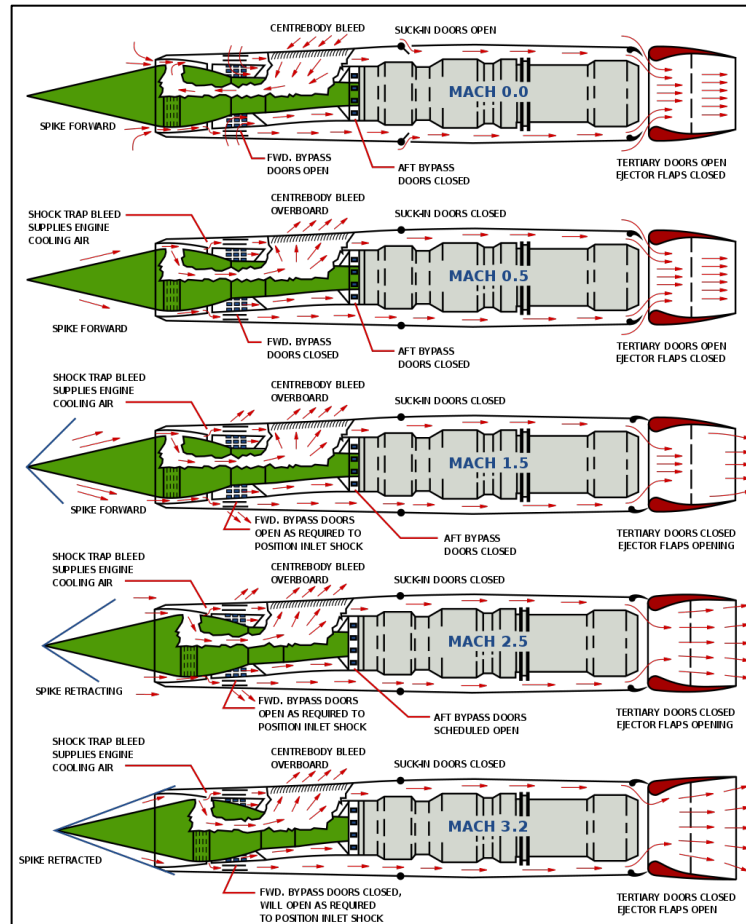


Figure 2.0.12 – Schematic drawings of J-58 Turboramjet

- General Electric's J79-3B turbojet with Rocketdyne AR2-3 rocket engine

Lockheed built this hybrid engine for NF-104A, a supersonic aircraft, for space pilot training. The high-performance engine was composed of a single-spool, 17-stage compressor, and 3-stage turbine. General Electric's engine had 6 rows of stator vanes and one variable inlet guide vanes [36]. The engines were also operational with afterburners. This trainer jet was also designed with the Rocketdyne AR2 engine. Comparatively, the rocket engine is much smaller than the J79. Regardless, AR2 can employ jet propellant as fuel and have variable thrust capabilities [35].



Figure 2.0.13 – Retired Lockheed NF-104A rocket engine attachment

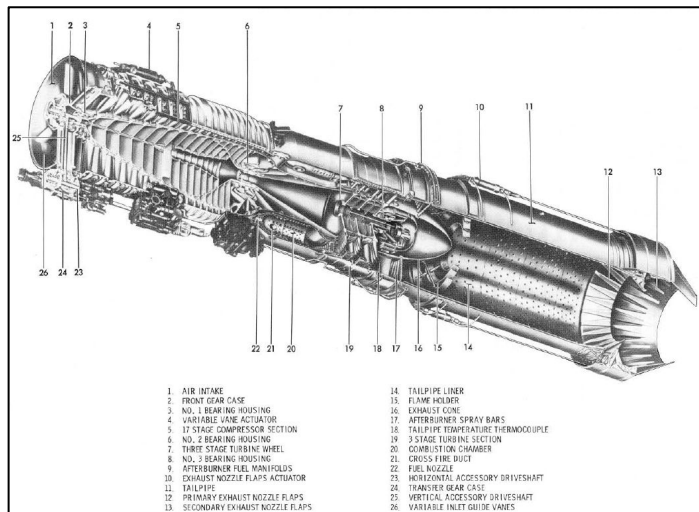


Figure 2.0.14 – Basic schematic drawing of J-79 variant



Figure 2.0.15 – Rocketdyne AR2-3

- Synergetic Air-Breathing Rocket Engine

Skylon is a hypothetical spaceplane currently under development by Reaction Engine Limited and will be installed with S.A.B.R.E engine. Alan Bond and his co-founders of SABRE engineered a unique precooler system that can cool down air from 1000C to -150C in less than a second. Furthermore, with their latest developments the innovative rocket engine could generate oxidizer in high speeds.



Figure 2.0.16 – Testing a Skylon spacecraft

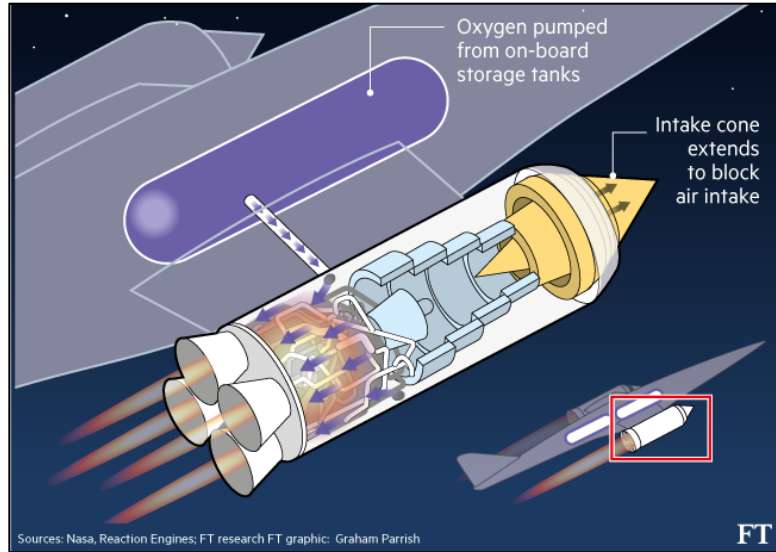


Figure 2.0.17 – Inner view of traditional SABRE

2.2.2 Comparison of Key Engine Parameters

The basic layout of hybrid engines can only be observed from the section above: however, to assess each engine’s performance a comparison of its parameters needs to be conducted. There are many variables that contribute to an engine’s performance. Since pursuing all these variables is outside the scope of this project, only five major parameters are selected: thrust to weight ratio, total fuel weight, thrust force, specific impulse, and specific fuel consumption. In table 2.1, twelve hybrid engine performance are compared. Few engines listed below were proposed designs that only had a TRL of 3, others were separate engines employed in tandem. From all the engines mentioned, only SABRE is truly an air-breathing integrated engine.

Table 2.0.3 – Imperative engine performance parameters

Engine	T/W	m_F (lbs)	Thrust (lbf)	Isp (secs)	SFC (lb/lbf*h)
SNECMA Atar 09C & SEPR 841 engine	jet: 4.13	14660	jet: 12740 rocket: 3375 lbf	220	mil: 1.01 afterburner: 2.03 jet Prop: 0.00435 (lbs/s)
SpaceDev Rocket Engine	2.08	5291	16500	250	0.004

Engine	T/W	m_F (lbs)	Thrust (lbf)	Isp (secs)	SFC (lb/lbf*h)
Turbomeca Gabizo & SEPR 631	0.24	1653	8684.2683	192	jet: 1.00
Pratt and Whitney J-58	0.44	101974.1661	50000		0.88
J79-GE-3B & AR2-3	4.6	7900	15600	245	mil: 0.85 afterburner: 1.965
Armstrong Siddeley Viper 8 and de Havilland Spectre	0.52	11000	9640	265	1.09
J47-GE-7and XLR11-RM-9	0.6	18364.5064	12,900		1.014
Turbomeca Marbore and SEPR 481	0.91	4740	10996.402	208	0.005
Armstrong Siddeley Viper 8 & A.S. Screamer	0.55	11000	9750	195	0.005
Wright J65-W-16A & Rocketdyne LR42-Na-x (AR-1)	0.55	9763	7700		0.916
Synergetic Air-Breathing Engine	14	486518.325	292200	450	---
SNECMA Atar 101 & Nord StatoReacteur	2.98		22900		1.05

2.3 Discussion and Conclusion

Engine placement on the aircraft depends on its mission objective and expected flight velocity. Engines embedded into the fuselage have lower roll inertia and require smaller landing gears,. These engines are also at a risk to of being exposed to wakes from the wing at high angles

of attack. On the other hand, wings with engine experience less flutter, are more exposed to cleaner air and will have lesser noise pollution. Some disadvantages include, having larger skin friction drag and more structural weight for mid to high wings. Each configuration has its own trade-offs and benefits. For this mission, most significant parameters include thrust to weight ratio, reduction of fuel mass and increasing useful payload into orbit. In hypersonic planes, to minimize drag, wings typically have a low aspect ratio and fuselage length. Due to these considerations, Bai LII cannot be placed on the wings. Rather, the proposed engine can be placed below the fuselage near the center of gravity of the highly swept delta wings.

Aside from the location of the engines, the choice of components can also influence engine performance. An ideal air-breathing engine does not require an inlet, compressor, or a turbine. As a result, such an engine cannot initiate enough thrust from static conditions. Adding a rocket at the end of this engine could alleviate this issue. Even though, this would slightly increase the weight of fuel when compared to existing spacecrafts, Bai LII will have lesser oxidizer onboard. Thus, Bai LII will have a smaller scaled rocket combustion chamber to generate thrust at Mach 0. Although, inlet cones will increase the gross take-off weight, the amount of incoming air can be easily controlled with an inlet cone. So, the proposed model of this design will have an inlet cone. During rocket mode, shock waves and aerodynamic heating will damage the engine's components. Thus, the shock cones should be able to extend and close the entrance of the engine. Besides during transitional periods, having extendable inlet cone will designate oblique shock waves at a prime location to provide optimal engine conditions. SABRE's precooler will also be installed between the inlet and combustion chamber. Also, at the aft of Bai LII, one rocket nozzle will be utilized for maximizing the thrust force.

Chapter 3 – Weight Sizing and Sensitivity Studies

3.1 Introduction

Engine configurations provide a rough estimate of weight components. To make a better approximation of the overall engine weight, proper weight sizing needs to be conducted. Since this engine is mainly exposed in hypersonic regimes, Roskam or Raymer's methods would not comply. Instead utilizing the Hypersonic Aerospace Sizing Analysis published by Harloff and Berkowitz will be more appropriate for space missions. However, to begin the sizing calculations, an estimate of the gross take-off weight, fuel, and payload weights are required. The estimate for take-off weight can be calculated utilizing Roskam's method. This method requires regression coefficients from comparative study of weight trends. The values attained from Roskam method will then be inputted into the HASA model from which better sizing approximations can be made. Equations from this model can then be employed to conduct trade studies for the engine.

3.2 Mission Weight Estimates

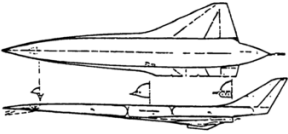
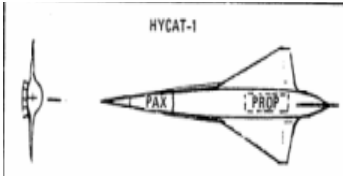
Weight estimates are primarily conducted by determining the weight trends of spacecraft with similar mission objectives. Even though nearly eleven engines were provided in the previous section, most of them did not have similar objectives to the proposed engine. If these spacecrafts are employed for the weight assessments, the results will be irrelevant. Rather, ten new spacecrafts were selected for this section and are listed below.

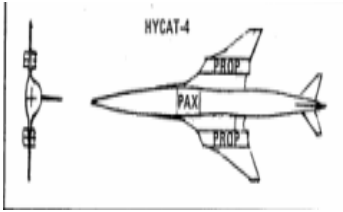
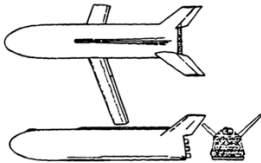
3.2.1 Engine Parameters of Similar Spacecrafts

Total take-off weight of the proposed spacecraft is a highly influential factor for the engine parameters. However, since this spacecraft travels in a hypersonic regime innovative methods are required to attain a proper value for the maximum take-off weight. In this project, two distinct methods are adopted: Roskam and HASA for the hypersonic regime. Initially total gross weight, fuel weight and empty weight are attained from the Roskam method. Once these values are calculated, they are inputted as initial guesses in the HASA method. Table 3.1 is the list of revised spacecraft model with their gross take-off weight and empty weight. The data from

the following table generate the regression coefficients and display the association between take-off weight and empty weight for this set of spacecrafts.

Table 3.0.1 – Weight data of spacecrafts with similar mission objectives

Name of Spacecraft	Gross Take-off Weight	Empty Weight
SpaceShipOne 	7937	2646
Shuttle 	255170	42941
Rockwell 	481400	61410
Hycat-1A 	613174	74670
GD Orbiter 	640000	287500

Name of Spacecraft	Gross Take-off Weight	Empty Weight
<p>Hycat-4</p> 	<p>773706</p>	<p>92757</p>
<p>Martin Marietta</p> 	<p>891795</p>	<p>49355</p>
<p>GD Booster</p> 	<p>959426</p>	<p>105831</p>
<p>Lockheed NF-104A</p> 	<p>2325607</p>	<p>53893</p>
<p>X_15</p> 	<p>3402316</p>	<p>131542</p>

Name of Spacecraft	Gross Take-off Weight	Empty Weight
D-588-2-Skyrocket 	21400	13500
Sanders Roe SR 53 	34000	14600
Trident II 	15787	9421

3.2.2 Determination of Regression Coefficients

Equation 3.1 unravels the logarithmic relationship between the take-off and empty weights.

$$W_{TO} = \text{invlog}_{10}(B * \log_{10} W_E + A) \quad (3.1)$$

The logarithmic values are calculated from table 3.1 and inputted into the equation above. From the inputs, a trendline is generated to attain an average slope of all the data points. Equation of the slope line provides the regression coefficients, A and B. where A is the y-intercept and B is the slope of the line.

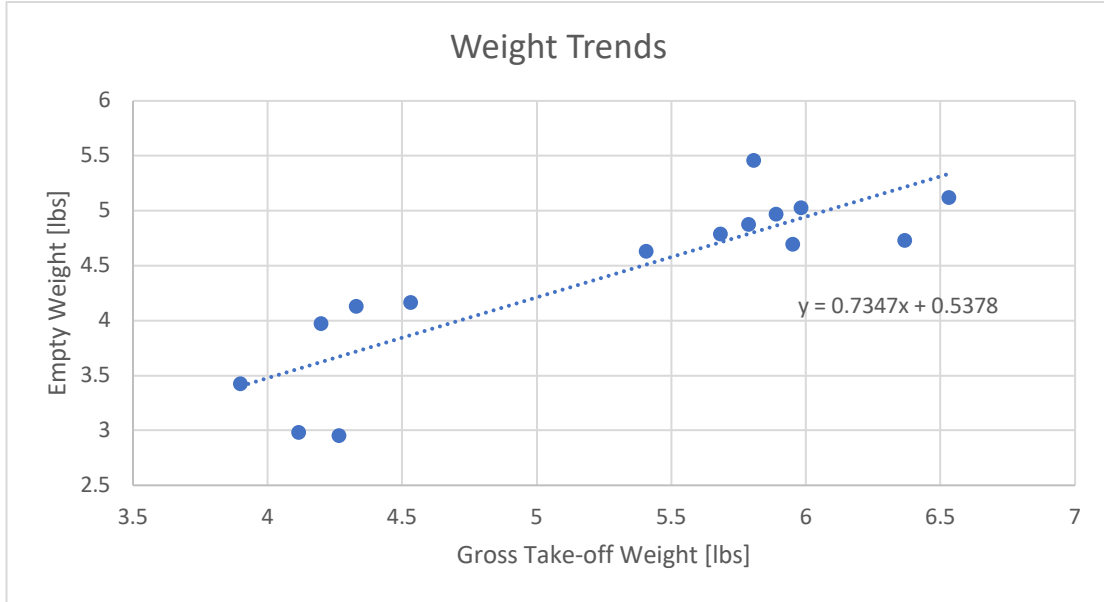


Figure 3.0.1 – Graph of regression coefficient

As seen from the graph above, A is equal to 0.5378 and B is equal to 0.7347. When these results were compared to Table 3.2 in Roskam [37], the closest match is the fighter jets with external loads. This discrepancy could be a result of including fighter jets that had integrated turbo-rocket engines in table 3.1.

3.2.3 Determination of Mission Weights

To determine the different weight ratios for varying phases, other values must be selected first. These include specific fuel consumption, velocity at different cruise speeds, the speed of sound, ranges for different phases, endurance times, L/D cruise, and loiter ratios. Equation 3.2 is utilized to compute weight ratios for cruise while equation 3.3 was employed to attain the ratios for loiter stages.

$$R_{cr} = \left(\frac{V}{SFC} \right)_{cr} \left(\frac{L}{D} \right)_{cr} \ln \left(\frac{W_4}{W_5} \right) \quad (3.2)$$

$$E_{ltr} = \left(\frac{1}{SFC} \right)_{ltr} \left(\frac{L}{D} \right)_{ltr} \ln \left(\frac{W_5}{W_6} \right) \quad (3.3)$$

Table 3.2 are the end results of most of the following calculations using excel. Furthermore, since Roskam's method only functions for aircrafts and engines within earth's atmosphere, the second climb to cruise displayed in figure 2.1 is disregarded for these calculations. During this stage, rocket engine incorporated in the model will be the primary propulsion system.

Table 3.0.2 – Weight fractions

Mission Phase	Weight Ratios	Mission Fuel Weight Fractions
Engine Start, and warm up	W_1/W_0	0.99
Taxi	W_2/W_1	0.995
Take-off	W_3/W_2	0.995
Climb	W_4/W_3	0.92
Cruise	W_5/W_4	0.65
Loiter	W_6/W_5	0.96
Descent	W_7/W_6	0.985
Landing, Taxi and Shutdown	W_8/W_7	0.992

Data from table 3.2 are inputted into equation 3.4 to compute the fuel fraction ratio.

$$M_{ff} = (W_1/W_{TO}) \sum^{i=n} (W)/W \quad (3.4)$$

The value from the fuel fraction predominates the iteration process for take-off weights. Equations 3.5, 3.6, and 3.7 lead to the tentative empty weight which is then compared to the extrapolated value of the allowable weight.

$$W_F = (1-M_{ff}) W_{TO} \quad (3.5)$$

$$W_{OE} = W_{TO} - W_F - W_{PL} \quad (3.6)$$

$$W_E = W_{OE} - (0.005 \times W_{TO}) - W_{crew} \quad (3.7)$$

Once the difference between the two weights is less than 1%, the overall gross weight for the proposed model is declared. Table 3.3 discloses the following weight iteration.

Table 3.0.3 – Weight iteration

W_o Guess	Empty Weight	Allowable Weight	Difference
90000	37318.58038	44025	-6706.419625
100000	42611.75597	44334	-1722.244027
101000	43141.07353	44364.9	-1223.826468
101008	43145.30807	44365.1472	-1219.839127
101098	43192.94665	44367.9282	-1174.981547
103455	44440.54814	44440.7595	-0.211358565

W_e = Empty Weight, W_o = Initial Guess Weight

From Table 3.3, the overall take-off weight for this design is 103,455lbs. This gross weight is inconsistent with most spacecrafts; therefore, the result seems to be invalid. Since this spacecraft requires a lot of weight, the amount of fuel is estimated to be around 48,177.18lbs. These weights seem to be slightly lower than expected which is attributed by the optimistic assumptions made during weight ratio calculations. For instance, the engine must produce a specific fuel consumption of 0.8 at hypersonic speeds with L/D ratio of 1.5. Engines have not been designed yet for such optimal fuel consumption ratios while traveling at Mach 3.5 or above. Moreover, in high speeds, attaining a value of 1.5 for L/D is almost improbable given that these speeds increase the pressure gradient when shocks are present. Shocks on airfoils increase lift. On the contrary, drag derived from shocks are twice as high which lowers the L/D ratio. All these assumptions increase the discrepancy between realistic and theoretical values.

3.3 HASA Model Weight Calculations

Hypersonic Aerospace Sizing Analysis is an iterative process developed from previously established hypersonic spacecrafts. The inputs to attain the total gross weight of a potential model include total volume (V_{tot}), length of the body (L_b) and diameter of the fuselage (D_{bc}). However, these three inputs are iteratively attained from the following constants: length calibration constant (k_b), calibration coefficient for non-idealized body (k_c), and ratio of body

depth over width (k_n). Equations 3.8-3.10 are derived from the ideal equations of total volume, wetted area, and body width.

$$k_n = D_{bc} \left| \frac{2\pi \left(\frac{1}{6 \tan \theta_f} + \frac{\Lambda_{lorb}}{2} + \frac{1}{6 \tan \theta_r} \right)}{\frac{W_{tot} - \delta W_{fuel} - W_{pay}}{\rho_a} + \delta V_{fuel} + V_{pay} + V_{a.f.}} \right| - 1 \quad (3.8)$$

$$k_c = \frac{2D_{bc}^2}{(1+k_n)^2 3.309 \sqrt{L_b V_{tot}}} \left(\frac{\pi}{\sin \theta_f} + \pi \Lambda_{lorb} + \frac{\pi}{\sin \theta_r} \right) \quad (3.9)$$

$$k_b = \frac{\left(\frac{D_{bc}}{1+k_n} \right) \left(\frac{1}{\tan \theta_f} + \Lambda_{lorb} + \frac{1}{\tan \theta_r} \right)}{L_b} \quad (3.10)$$

Total volume is a summation of all the volumes including empty weight, fuel, payload, and air factory as seen in equation 3.11.

$$V_{tot} = \frac{W_{tot} - \delta W_{fuel} - W_{pay} - \delta W_{tnk} - W_{tps}}{\rho_a} + \delta V_{fuel} + V_{pay} + V_{a.f.} \quad (3.11)$$

The ideal wetted area for a hypersonic spacecraft is function of body length, calibration coefficient and total volume. Since the aircraft is traveling in hypersonic speeds, wave drag will contribute heavily to the total drag of the body. Therefore, in the Sears-Haack body of revolution the effect of wave drag is accounted by the value of 3.309 as seen in equation 5.

$$S_{tot} = 3.309 k_c \sqrt{L_b V_{tot}} \quad (3.12)$$

Equation 3.13 showcases total length of the fuselage as a function of fineness ratio, volumetric efficiency, and length calibration constant. However, fineness ratio is equivalent to the body length over body diameter as depicted in equation 3.14.

$$L_b = k_b \left(\frac{F_f^2 V_{tot}}{\frac{\pi}{4} \eta_{vol}} \right)^{\frac{1}{3}} \quad (3.13)$$

$$F_r = \frac{L_b}{D_{bc}} \quad (3.14)$$

Finally, the diameter of the body is calculated from the total volume, body length and volumetric efficiency. Since a CAD model has not been developed yet, the volumetric efficiency is the tabulated averages of similar spacecrafts in table 3.1. Body width is a function of depth over width ratio and body diameter, which is disclosed in equation 3.16.

$$D_{bc} = \sqrt{\frac{V_{tot}}{L_b \frac{\pi}{4} \eta_{vol}}} \quad (3.15)$$

$$B_b = \frac{2D_{bc}}{1+k_n} \quad (3.16)$$

Once all the required values are inputted into the HASA model, the results are then utilized on the equations above to generate the ideal total wetted area, body length and diameter. These ideal values are compared to its actual counterpart equations, listed below, by taking their differences. The values that result in less than 10% difference are selected as the final total volume, wetted area, length, and diameter of the proposed spacecraft. Some of the other guessed values that need to be inputted into the HASA model includes: θ_f , θ_r and Λ_{lorb} . These inputs refer to the geometry of the fuselage. For instance, θ_f is the forward cone half angle represented in degrees while θ_r is the aft cone half angle in degrees. The ratio of body's length over radius is signified by Λ_{lorb} . All these values were averaged from the spacecrafts listed in table 3.1.

$$S_{tot} = \frac{2D_{bc}^2}{(1+k_n)^2} \left| \frac{\pi}{2} \frac{1}{\sin \theta_f} + \pi \Lambda_{lorb} + \frac{\pi}{2} \frac{1}{\sin \theta_r} \right| \quad (3.17)$$

$$L_b = \frac{\frac{R}{\tan \theta_f} + R \Lambda_{lorb} + \frac{R}{\tan \theta_r}}{k_b} \quad (3.18)$$

$$V_{\text{tot}} = \left(\frac{D_{bc}}{1+k_n}\right)^3 2\pi \left(\frac{1}{6\tan\theta_f} + \frac{\Lambda_{\text{orb}}}{2} + \frac{1}{6\tan\theta_r}\right) \quad (3.19)$$

Once the iterative process was conducted, the final values for all four terms are summed up in table 3.4. Initially, it was quite evident that the calculations for the wetted surface area was inaccurate, especially since there was an enormous discrepancy between the predicted and the actual values. One of the speculations was that the calibration coefficient for non-idealized body, attained from the calculations, was out of proportion. Following that logic, error was soon discovered. Unfortunately, the half angle values were inputted into the equations as degrees instead of radians. Once this error was corrected, discrepancy between the ideal and final values were still higher than 10%. Therefore, a correction factor of 0.07 was multiplied to the actual value because the computed value for k_b was derived from the averages of similar spacecrafts which were 7% away from the ideal value of the calibration coefficient. So the final value of S_{tot} was corrected from 92,090,918.2ft² to 13,446,364.27 ft².

Table 3.0.4 – Ideal and actual values of the proposed model

Terms	Ideal	Final Values
V_{tot}	46488.14	46520.31
S_{tot}	13388147.37	13446364.27
L_b	218.59	220.34
D_{bc}	19.67	19.54

These values are then used as inputs to tabulate the total gross weight of the proposed model which is computed by equation 3.20. Each component for this equation is formulated by the relations presented in Appendix A.

$$W_{\text{gtot}} = W_{\text{propellant}} + W_{\text{str}} + W_{\text{pay}} + W_{\text{propulsion}} + W_{\text{sub}} \quad (3.20)$$

The summation of all the results is listed in table 3.5. These values are then verified with spacecrafts that have similar missions. Based on the comparisons, they seem to have similar approximations.

Table 3.0.5 – Final weight results

Weights	Final Values
W_{fuel}	471148.573 lbs
W_{str}	361403.8417 lbs
W_{pay}	212322 lbs
W_{prop}	488125.067 lbs
W_{sub}	28522.15861 lbs
W_{gtot}	1561521.64 lbs

3.4 Trade Studies

There are multiple parameters that influence engine design; however, the sensitivity of each factor is not known. Therefore, trade studies are conducted to observe the most influential factor on the overall weight of the engine. One study was conducted to observe the effect of expansion ratio on the engine weight of the rocket. This was conducted from the equation 3.21, where TTOT represents the total take-off thrust, ϵ represents the expansion ratio and N_{engr} represent the number of rocket engines employed. Figure 3.3 depict the results from the study and reveal that there is a steady increase between expansion ratio and engine weight.

$$W_{rke} = 0.00766 * (TTOT) + 0.00033 * (TTOT) * (\epsilon^{0.5}) + 130 (N_{engr}) \quad (3.21)$$

Equation 3.22 was based on data from GE 12/JZ8 turboramjet engine. This engine's data was employed in the proposed design for its desirable attributes. Constants from this equation are weight coefficients of the upper and lower design points. These design points were a function of dynamic pressure, altitude, Mach number, maximum and minimum inlet pressures.

$$W_{trj} = WC * (e)^{0.0032(\dot{m}_a)} \quad (3.22)$$

Figure 3.2 displays the result of varying the weight coefficients between the upper and lower design limits. The results display a positive, linear relation between the mass flow rate and the overall weight of the engine.

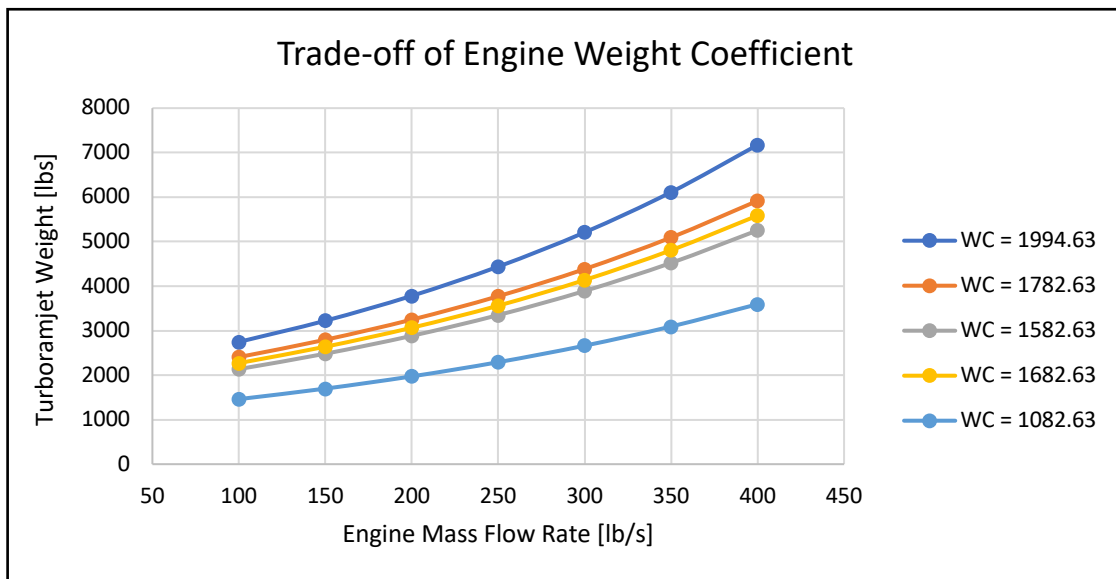


Figure 3.0.2 – Effect of weight coefficients on overall turboramjet engine weight

Mass flow rate has a direct correlation to the inlet's diameter, therefore as the diameter of the engine is increased the overall weight increases. On the other hand, in vacuum, mass flow rate of air is not imperative compared to the thrust produced by the engine. Therefore, a study between total vacuum thrust with respect to the rocket engine's weight coefficient is conducted and depicted in figure 3.3.

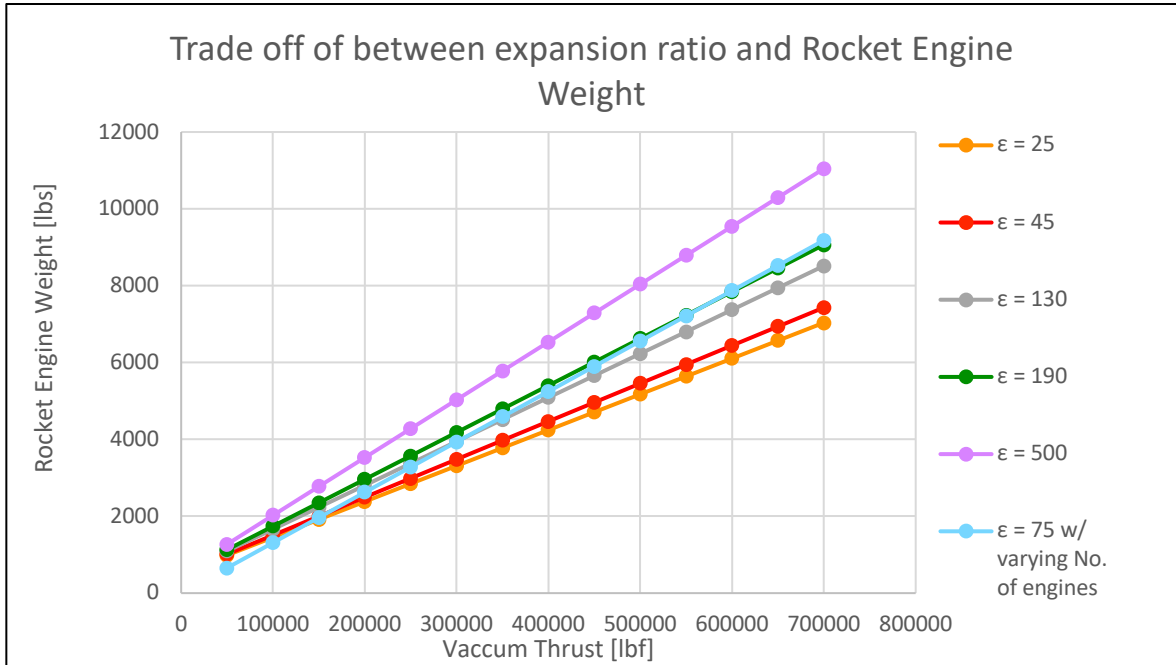


Figure 3.0.3 – Study of weight coefficients on overall engine weight of rockets

The expected range for thrust structure coefficient, denoted by WC_{ST} from equation 3.23, is determined from the slope shown in figure 3.4 which is averaged from several aircraft engine's listed in the legend.

$$W_r = WC_{ST}^{TOT} \quad (3.23)$$

Trade study for rocket engines were conducted with varying thrust structure coefficients. Based on the data, rocket engine weight is linearly affected by thrust coefficient and expansion ratio.

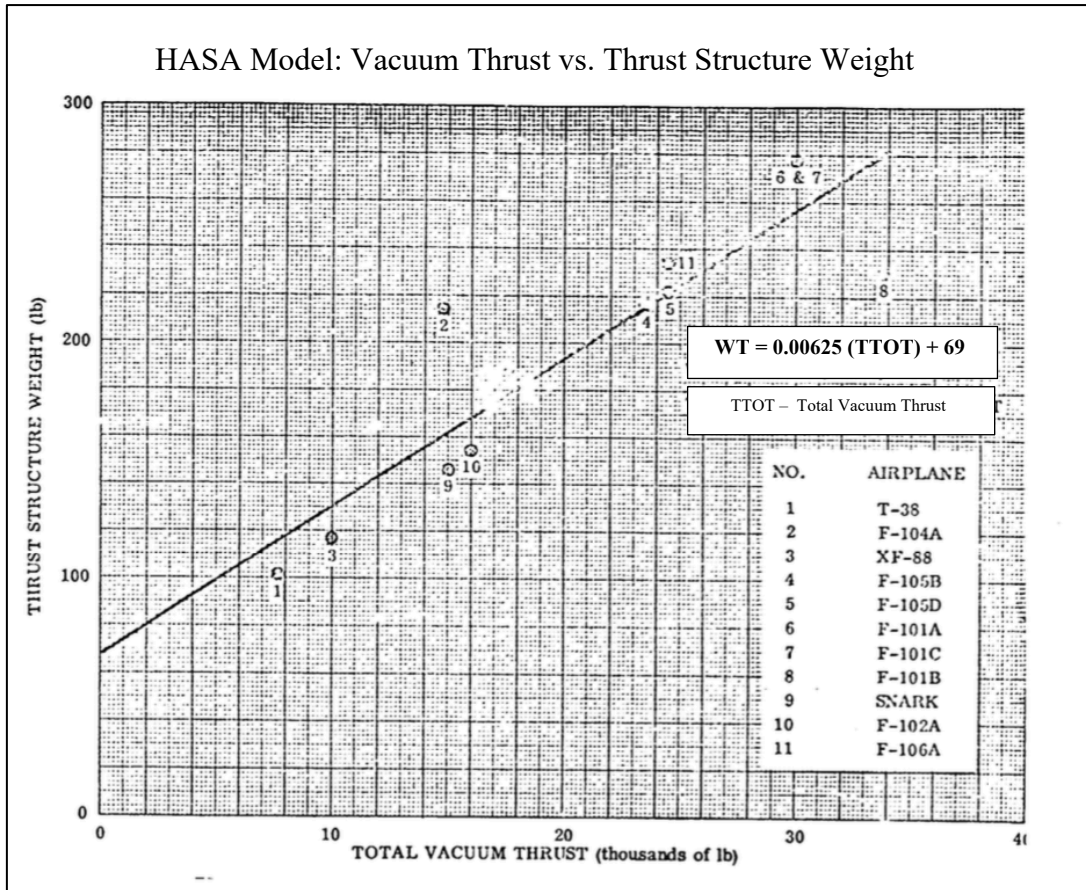


Figure 3.0.4 – Thrust structure weight is a function of total vacuum thrust, adapted from [44]

A key parameter for an airbreathing engine that travels in varying altitudes, speeds, pressure, and temperatures require some variance with the inlet ramp to maintain optimal conditions for maximum engine performance. Altering an inlet ramp requires additional actuators, controls and more advanced technology which are directly correlated to inlet ramp weight. The exact relation is disclosed in equation 3.24 where the constants 117.35 and 0.294 represent the variable ramp weight coefficient employed as the intercept and slope respectively.

$$W_{IVR} = 117.35 * (\eta)^{0.294} \tag{3.24}$$

Variable ramp weight is a function of engine weight coefficient. Weight coefficient is a function of total ramp length (L_{TR}), number of inlets (n), total capture area at the inlet (A_{TC}), and temperature correction factor (T_{cf}) as shown in equation 3.25.

$$\eta = L_{TR} * n * A_{TC}^{0.5 * (T_{cf})} \quad (3.25)$$

Altering the weight coefficients almost generates a logarithmic relation with respect to overall ramp weight as observed in figure 3.5.

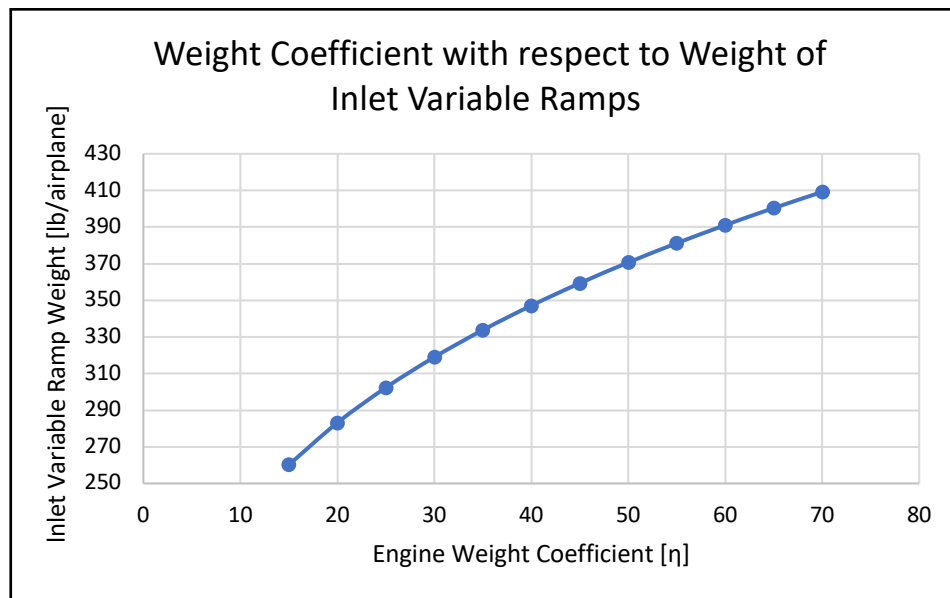


Figure 3.0.5 – Effect of weight coefficient on variable inlet ramp

Most influential variable of the ramp length’s weight coefficient is altering the temperature correction factor as it increases the value exponentially. Second most significant term is the variation of inlet capture area as observed in figure 3.6. For variable ramp length, the number of inlets were set at 2, total inlet capture area was equal to 25.78 ft², and temperature correction factor was held at 5.475. On the other hand, the variable inlet capture area was altered in increments of 1.98 from a minimum area of 1.98 ft² with varying total ramp length.

Temperature correction factor is a function of Mach number so the data was tabulated from Mach 2 to 24.

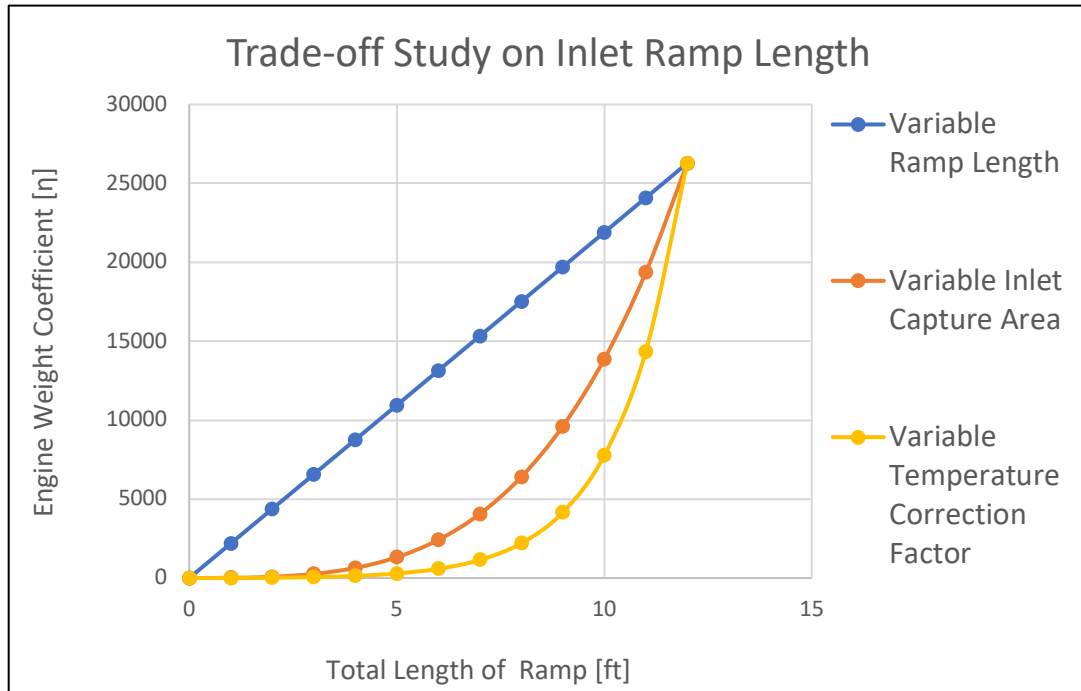


Figure 3.0.6 – Study on inlet ramp length

Engine performance is also determined by the amount of fuel injected onto the incoming airflow. The performance increases when more fuel particles are mixed with compressed air. Since two methods were utilized to determine the overall weight of the spacecraft, two fuel fractions were attained. Based on Roskam’s method, the fuel mass fraction has an exponential relationship with the gross takeoff weight of an aircraft, as depicted in figure 3.7.

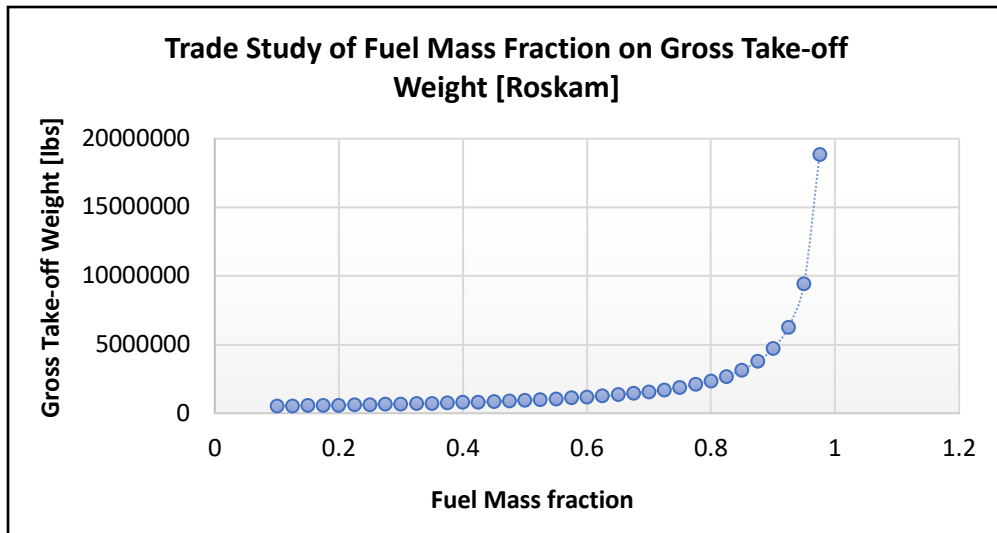


Figure 3.0.7– Effect of increased fuel fraction on total vehicular weight

On the contrary, HASA model displays a linear function of fuel fraction with respect to the gross take-off weight as showcased in figure 3.8. However, the results from Roskam’s method were utilized as inputs for the HASA model. Since this model aids with the design of spacecrafts, the trade study of fuel mass fraction from HASA calculations is more pertinent for this design project.

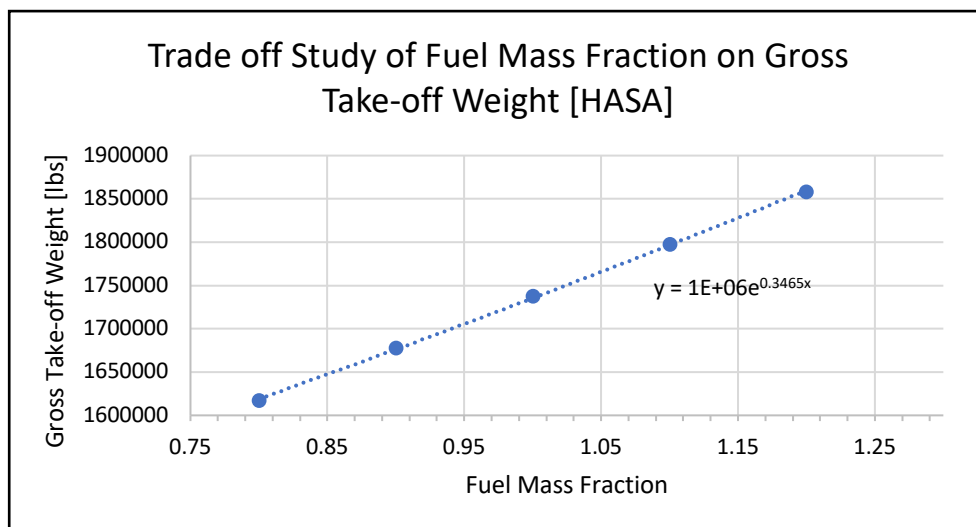


Figure 3.0.8 – Effect of increased fuel on total vehicular weight [HASA]

3.5 Discussion and Conclusion

Even though this design is only for an engine, weight iterations must be calculated to determine the overall weight of the spacecraft. Gross take-off weight is then used to calculate weights of other subsystems including propulsion and propellant. Furthermore, overall fuel required for the specified mission also effects engine weight. Therefore, all the key parameters from the HASA model are summarized in Table 3.6.

Table 3.0.6 – Summary of all key parameters

Parameters	Values
V_{tot}	46520.31 ft ³
S_{tot}	192090918.2 ft ²
L_b	220.34 ft
D_{bc}	19.54 ft
W_{gtot}	1561521.64 lbs
W_{prop}	488125.067 lbs
W_{fuel}	471148.573 lbs

Due to the unique design, multiple trade studies were generated for different types of engines. Each type of engine was affected by specific variables. For instance, turboramjet engines were influenced more by mass flow rate than rocket engines. In fact, mass flow rate displayed an linear growth for the overall engine weight. On the other hand, rocket weight was linearly affected by thrust generated in space. Regardless, key parameters that hindered engine performance were variable inlet ramps and fuel mass fraction. Increase in fuel fraction had a greater effect on gross take-off weight than the effect of variable inlet. When comparing the inlet ramp weight to the gross take-off weight of the spacecraft, ramp weight was nearly insignificant. This is reasonable since ramps only comprise a small portion of the engine when compared to the entire aircraft. Furthermore, increased fuel fraction translates to adding more fuel volume or storage tanks in the spacecraft.

Chapter 4 - Selecting Design Point (MDO)

4.1 Introduction

Engine performance is assessed by three main factors, specific thrust, specific impulse, and specific fuel consumption. All three parameters gauge the power and efficiency of an engine. Specific thrust is a function of mass flow rate, initial Mach number and temperature difference of combustion, especially for airbreathing engines. On the other hand, specific fuel consumption is a direct function of mass and fuel flow rates. However, fuel consumption and overall engine efficiency can be an indirect function of initial Mach flow and the combustion's temperature ratio. Since the main objective of this proposed engine is designed to function in supersonic to hypersonic speeds, only derivations for ramjet and scramjet modes are included. Analysis of ideal cycles for ramjet and scramjet would produce unrealistic values. This is due to total pressure and temperature losses from multiple oblique shock waves. Since this is a preliminary process, assessing the ideal cycles for both modes would provide a general design space. Through Multi-Design Optimization technique, design points can be generated from optimized parameters in this space.

4.1.1 MDO for Airbreathing Engine

At high velocities, compressors become extremely inefficient and eventually obsolete. To counteract this problem, aerodynamicists design oblique shocks at the inlet to attain an optimal total pressure. Such an innovative concept allows airbreathing engines to function without compressors and turbines. Due to this change in engine configuration, a new numbering system must be established. Therefore, a new station numbering system for both modes are proposed in figure 4.1.

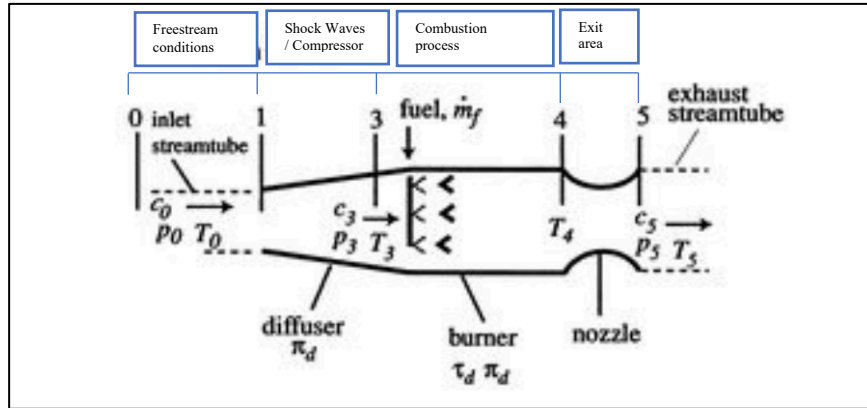


Figure 4.0.1 – Ramjet stations numbered [52]

All parametric equations for ramjet engines are derived from specific thrust force, which is a function of exit velocity, initial velocity, and mass flow rate, as shown in equation 4.1. Assumptions for this equation include: an ideally expanded thrust, adiabatic and isentropic processes and inviscid flows. Also, the pressure ratios for diffuser, combustor and nozzle are assumed to be one.

$$\frac{F}{a_o \dot{m}} = \left(\frac{V_e}{a_o} - \frac{V_o}{a_o} \right) \quad (4.1)$$

Given that velocity is linearly correlated to Mach number and speed of sound, the above equation can be transformed into equation 4.2.

$$\frac{F}{a_o \dot{m}} = \left(\frac{M_5 \sqrt{T_5}}{\sqrt{T_o}} - \frac{M_o \sqrt{T_o}}{\sqrt{T_o}} \right) \quad (4.2)$$

To simplify this equation further, applying the ideal expansion principal allow the inlet and exit pressure ratios to be equivalent. Both pressure ratios are derived from the isentropic relations which make them a function of inlet and exit Mach numbers. Therefore, it is safe to assume the exit Mach number is also equal to the inlet Mach number. So, the above equation simplifies to equation 4.3.

$$\frac{F}{a_o \dot{m}} = M_o \left(\frac{\sqrt{T_5}}{\sqrt{T_o}} - 1 \right) \quad (4.3)$$

The formulas derived in equation 4.4 is based on isentropic relationships at the exit and entrance of the engine. Expanding on these isentropic relationships, if $M_5 = M_o$, then the ratio of T_5/T_o can be simplified down to T_{t5}/T_{to} , as displayed in equation 4.5.

$$\frac{T_{t5}}{T_5} = 1 + \frac{\gamma-1}{2} (M_5)^2 ; \frac{T_{to}}{T_o} = 1 + \frac{\gamma-1}{2} (M_o)^2 \quad (4.4)$$

$$\frac{T_5}{T_o} = \left(\frac{T_{t5}}{1 + \frac{\gamma-1}{2} (M_5)^2} \right) * \left(\frac{1 + \frac{\gamma-1}{2} (M_o)^2}{T_o} \right) = \frac{T_{t5}}{T_{to}} = \frac{T_{t4}}{T_{t3}} = \tau_b \quad (4.5)$$

By substituting tau b into equation 4.3, equation 4.6 is derived which is a generalized specific thrust equation.

$$\frac{F}{a_o \dot{m}} = M_o (\sqrt{\tau_b} - 1) \quad (4.6)$$

In a similar fashion, specific fuel consumption and specific impulse are derived from the assumptions and simplifications made above. Equation 4.7 and 4.8 depicts the final formulas for specific fuel consumption and specific impulse, respectively.

$$S = \frac{f}{\frac{F}{ma_o}} \quad (4.7)$$

$$Isp = M_o (\sqrt{\tau_b} - 1) \frac{a_o}{f * g} \quad (4.8)$$

All three parametric equations are functions of initial Mach number and combustion temperature ratios. Therefore, the feasible solution is determined by randomly selecting a range of tau b and initial Mach number. However, this would produce limitless solutions. To prevent an undefined design space, constraints are applied to the solutions. Table 4.1 summarizes all the constraints applied for this analysis process.

Table 4.0.1 – Necessary constraints for MDO Analysis

No.	Constraints
1	$\frac{F}{a_o \dot{m}}, \Delta h_{pr} \neq 0$
2	$\tau_r * \tau_c \geq 1$
3	$f \leq 0.068$

The value of fuel ratio is attained from the stoichiometric relations of hydrocarbons. Equation of fuel ratio is a function of tau b, tau r, enthalpy of products, specific heat at constant pressure and freestream temperature as displayed in equation 4.9.

$$f = \frac{(\tau_b - 1) \cdot \tau_r \cdot C_p \cdot T_o}{h_{PR}} \leq 0.068 \quad (4.9)$$

All possible values that satisfy the given constraint are graphed in figure 4.2. Data below the red parabola is labeled as the feasible design space. These values are then employed into the derived ideal equations of specific thrust and specific impulse as listed above.

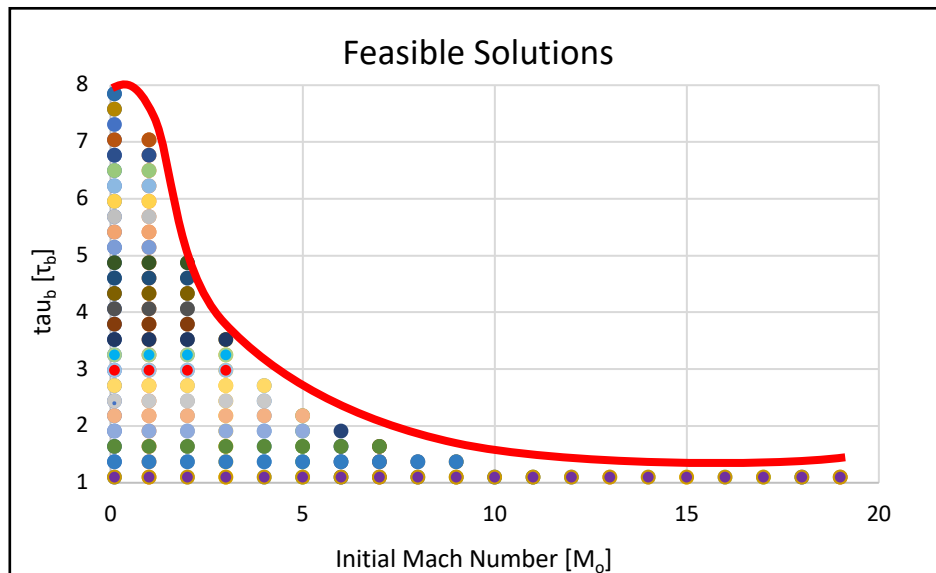


Figure 4.0.2 – Optimal feasible design space

From selected ranges of Mach and tau b values, the data for specific fuel consumption, specific thrust and specific impulse are plotted in a two-dimensional graph. The relations between specific fuel consumption and specific thrust are disclosed in figure 4.3 whereas the relationship between specific impulse and specific thrust are displayed in figure 4.4.

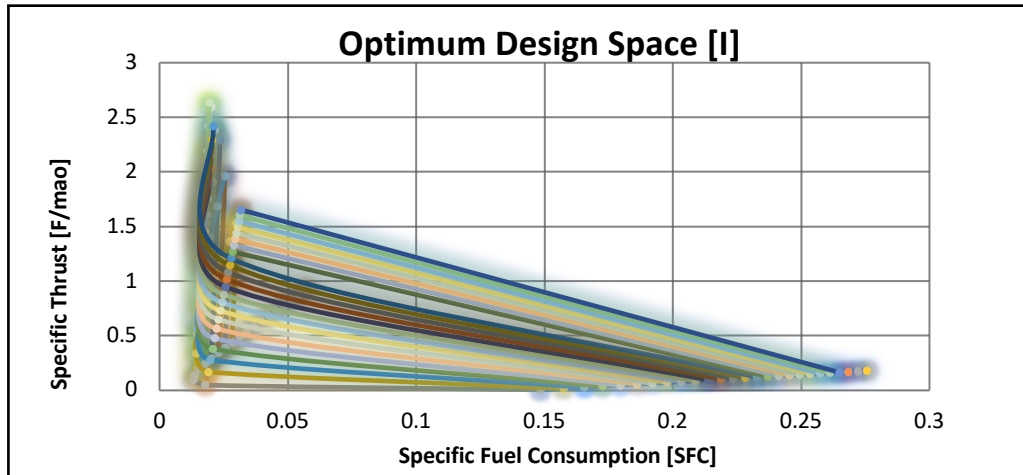


Figure 4.0.3 – Specific fuel consumption versus specific thrust

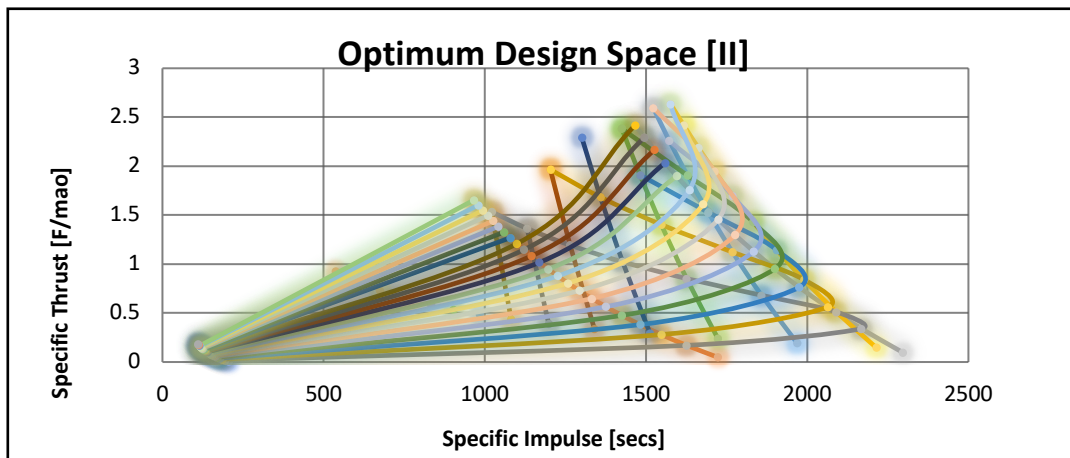


Figure 4.0.4 – Specific impulse versus specific thrust

For a thorough and complete analysis, three-dimensional data has to be populated for selecting a more accurate design point. Therefore, as the third parameter, the engine's overall efficiency is tabulated. Equation 4.10 showcases the relationship of the overall efficiency with respect to thermal and propulsive efficiencies.

$$\eta_o = \eta_p \eta_T \quad (4.10)$$

Thermal efficiency is a function of isentropic relations while propulsive efficiency is a function of velocity ratio. Both thermal and propulsive efficiency are shown in equations 4.11 and 4.12, accordingly.

$$\eta_T = \frac{\frac{\gamma-1}{2}M_0^2}{1 + \frac{\gamma-1}{2}M_0^2} \quad (4.11)$$

$$\eta_p = \frac{2}{1 + \frac{V_e}{V_o}} \quad (4.12)$$

Inlet and exit velocities are tabulated from M_o , M_5 , T_o , and T_5 . From previous assumptions and relations, these variables can be converted to functions of τ_b and M_o . Utilizing MATLAB, a three-dimensional plot was generated for ramjet analysis as seen in figure 4.5. The selected design point has an overall efficiency of 8.294%, a specific thrust of 2.539, and 0.02 specific fuel consumption.

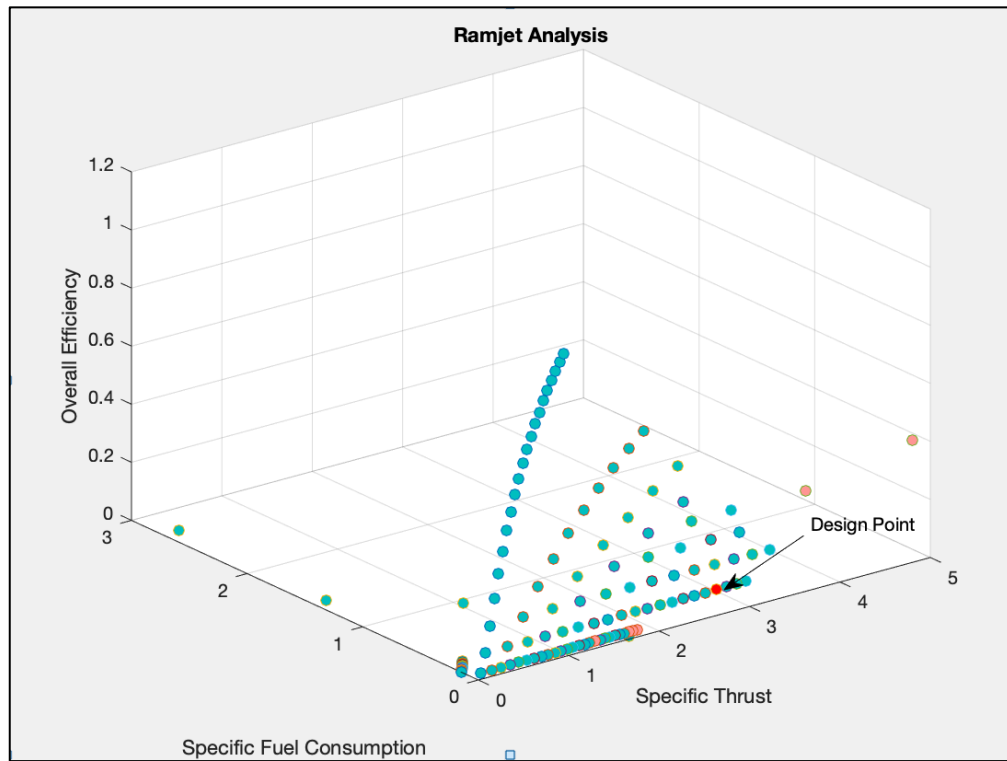


Figure 4.0.5 – Ramjet design point based on specific thrust, specific fuel consumption and overall efficiency

Similarly, an analysis for a scramjet engine was conducted with all three parameters as functions of τ_b and M_o . These functions were simplified using the same assumptions presented in the ramjet analysis and are displayed in equations 4.13, 4.14, and 4.15.

$$\frac{F}{a_o \dot{m}} = M_5 \sqrt{\frac{\tau_b \tau_r}{1 + \frac{\gamma-1}{2} M_5^2}} \quad (4.13)$$

$$S = \frac{f}{\frac{F}{a_o \dot{m}}} \quad (4.14)$$

$$\eta_o = \left(1 - \frac{Q_{out}}{Q_{in}}\right) * \left(\frac{2}{\frac{M_5 \sqrt{T_5}}{M_o \sqrt{T_o}} + 1}\right) \quad (4.14)$$

Energy added and rejected out of the system have two distinct functions. Energy inputted into the system is a product of mass flow rate of fuel and enthalpy gradient of reacting species, as observed in equation 4.15. The mass flow rate of fuel can be related between fuel ratio and mass flow rate as stated in equation 4.16.

$$Q_{in} = \dot{m}_f h_{pr} \quad (4.15)$$

$$f = \frac{\dot{m}_f}{\dot{m}_o} \quad (4.16)$$

On the contrary, energy output is a function of mass flow rate, specific heat at constant pressure and temperature gradient between inlet and nozzle. This relation is depicted in equation 4.17.

$$Q_{out} = \dot{m}_o C_p (T_5 - T_o) \quad (4.17)$$

Employing the same constraints that were depicted in table 4.1, the scramjet data were plotted in a three-dimensional graph as observed in figure 4.6. From this graph, the design point was selected to have an overall efficiency of 3.16%, specific fuel consumption of 0.017 and a specific thrust of 2.91.

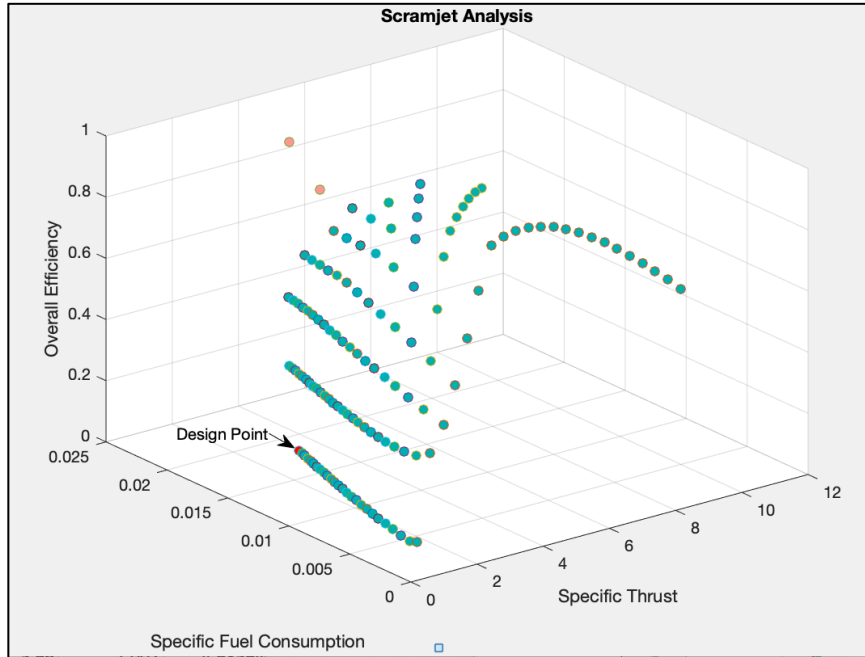


Figure 4.0.6– Scramjet design point based on specific thrust, specific fuel consumption & overall efficiency

4.1.2 MDO for Rocket Engine

Thus far, only the airbreathing modes were discussed. However, after certain hypersonic speeds, any type of jet engine will disintegrate. So, an addition of a rocket engine is required for the proposed model. Optimization of a rocket engine is performed in a similar fashion as the airbreathing engine. The only differences are the governing equations, constraints, and the parametric choices. For the rocket mode, coefficient of thrust, exit velocity and specific impulse are the selected parameters to optimize. Equation 4.18 depicts expansion ratio as a function of gamma and pressure ratios. Capital gamma is also a function of lower-case gamma as shown in equation 4.19.

$$\frac{A_e}{A^*} = \frac{\Gamma(\gamma)}{\sqrt{\frac{2\gamma}{\gamma-1} \left(\frac{P_e}{P_c}\right)^{\frac{2}{\gamma}} \left[1 - \left(\frac{P_e}{P_c}\right)^{\frac{\gamma-1}{\gamma}}\right]}} \quad (4.18)$$

$$\Gamma(\gamma) = \sqrt{\gamma \left(\frac{1+\gamma}{2}\right)^{\frac{1+\gamma}{1-\gamma}}} \quad (4.19)$$

All three parametric equations are stated below. Evidently, the common variable among all three equations is the expansion ratio.

$$C_F = \Gamma(\gamma) \sqrt{\frac{2\gamma}{\gamma-1} \left[1 - \left[\frac{P_e}{P_c} \right]^{\frac{\gamma-1}{\gamma}} \right]} + \left(\frac{P_e}{P_c} - \frac{P_a}{P_c} \right) \frac{\Gamma(\gamma)}{\sqrt{\frac{2\gamma}{\gamma-1} \left(\frac{P_e}{P_c} \right)^{\frac{2}{\gamma}} \left[1 - \frac{P_e}{P_c} \right]^{\frac{\gamma-1}{\gamma}}}} \quad (4.20)$$

$$V_e = \sqrt{\frac{2\gamma}{\gamma-1} \left[1 - \left[\frac{P_e}{P_c} \right]^{\frac{\gamma-1}{\gamma}} \right] \frac{R_A}{M_W} T_c} \quad (4.21)$$

$$I_{sp} = \frac{\sqrt{\frac{2\gamma}{\gamma-1} * \frac{R_A}{M_W} * T_c * \left[1 - \left[\frac{P_e}{P_c} \right]^{\frac{\gamma-1}{\gamma}} \right]}}{g_0} \quad (4.22)$$

However, expansion ratio is not the constraint for this analysis. Rather, the pressure ratio of ambient over combustion chamber is chosen as the constraint for rocket mode analysis. This is due to the indirectly strong influence atmosphere has on rocket performance. As the rocket engine travels from sea-level to space, the ambient pressure decreases. Thus, the pressure ratio is limited to values from 0 to 0.05. At zero pressure ratio, the optimum coefficient of thrust is attained. This is clearly disclosed in figure 4.7. Furthermore, each curve's maxima are also obtained to discover the optimum expansion ratio and coefficient of thrust at specific pressure ratio points.

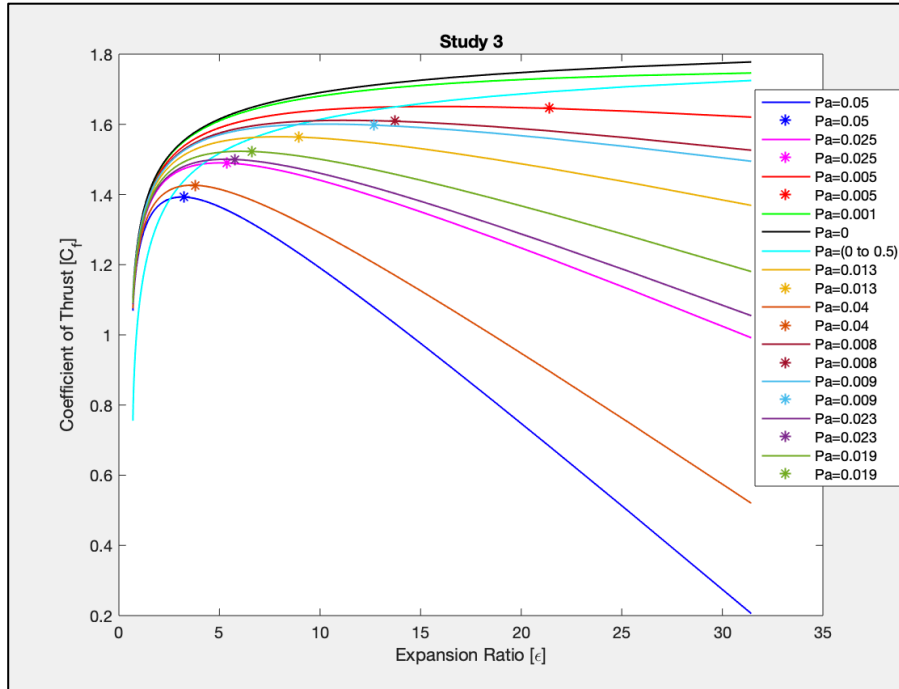


Figure 4.0.7 – Expansion ratio versus coefficient of thrust

Another two-dimensional analysis is conducted between characteristic velocity and expansion ratio. The results are showcased in figure 4.8. Since combustion temperature is held at a constant, the only variable term in equation 4.21 is the pressure ratio. As the pressure ratio is confined within a narrow range, all the velocities assessed in this range will have negligible differences. This corroborates the results seen in figure 4.8, where all the velocities are superimposed to one trendline.

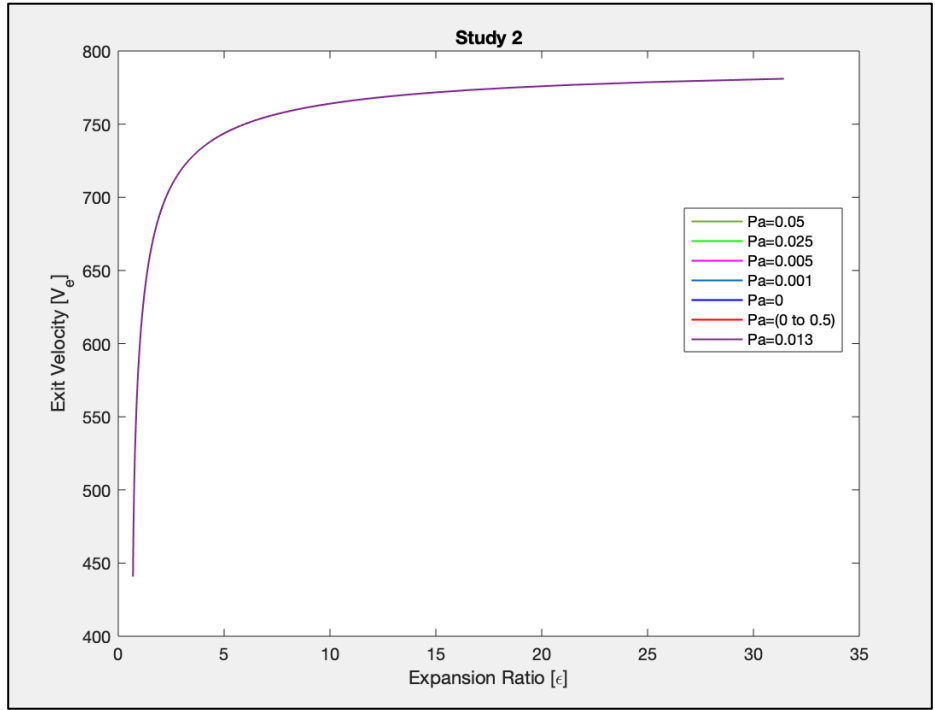


Figure 4.0.8 – Expansion ratio versus characteristic velocity

Like the airbreathing analysis, a three-dimensional comparison between the three parametric factors were generated. From the graph displayed in figure 4.9 a design point of 1.725 coefficient of thrust, 781 m/s exit velocity and specific impulse of 210.6 sec is selected.

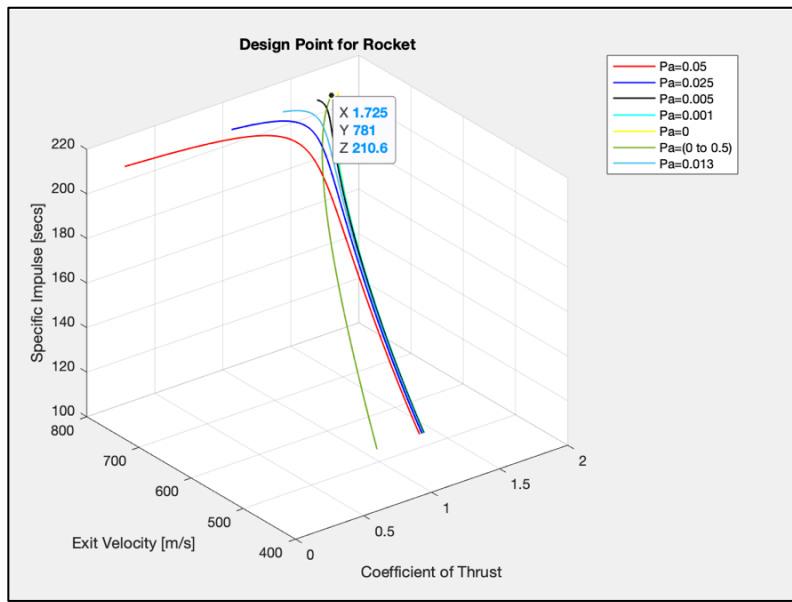


Figure 4.0.9 – Design point for rocket engine from coefficient of thrust, characteristic velocity and specific impulse

4.2 Discussion and Conclusion

According to the mission statement, the proposed model must function in speeds varying from Mach 0 to Mach 10. Since an airbreathing engine is incapable of generating thrust at Mach 0, an addition of a rocket engine is required. Furthermore, rockets are the only engines that can function efficiently at escape velocity speeds. To reduce the number of equations, the broad range of speeds were divided into three main speed regimes: subsonic (Mach 0 to Mach 1), supersonic (Mach 1 to Mach 4), and hypersonic (Mach 5 to Mach 10). Since each regime contains different properties and requirements, three design points for the proposed model were generated. The first design point was for an ideal ramjet, the second was for a scramjet and the third point was for the rocket. Rocket engine is designed for two speeds, subsonic and extremely high hypersonic speeds. However, the scope of this project only permits to observe the speeds from Mach 0 to Mach 10. Therefore, high hypersonic speeds are not considered for these calculations.

Table 4.0.2 – Summary of all three design points for the engine

Engine	Specific Thrust	Specific Fuel Consumption	Overall Efficiency
Ramjet	2.539	0.02 sec/m	8.294%
Scramjet	2.91	0.017	3.16%
Engine	Coefficient of Thrust	Exit Velocity	Specific Impulse
Rocket	1.725	781 m/s	210.6 secs

All three design points are restated in table 4.2. The points selected for ramjet and scramjet engines have very low overall efficiencies. These low values were selected to account for the losses from total pressures and temperatures across each oblique shock. Since rockets are generally closed systems where the engine does not have much interaction with the freestream velocity, these engines have distinct requirements than an airbreathing engine. Typically chemical rockets have specific impulse that ranges from 200 to 468 secs [55]. Regardless, the fuel choice for Bai LII are liquid hydrogen and oxygen. This combination of fuel and oxidizer has a maximum specific impulse of 400 secs [55], However, the design point's impulse is lower compared to the expected value. This could be a result of assuming incorrect gas constant and molecular weight of the propellants.

Chapter 5 - Computer Aided Design for Airbreathing Engine

5.1 Introduction

All the necessary measurements for the CAD model will be derived from the design points designated in Chapter 4. The derivations will mainly focus on ramjet and rocket engine components. Scramjet engine has similar components to a ramjet except for the addition of extra thermal protection system. Furthermore, an integrated design permits a model to unite different concepts into one efficient system. Therefore, both ramjet and scramjet engines will share the same diffuser, inlet, combustion, and nozzle. However, the scramjet's design point will be utilized as the maximum boundary for this model. Components that have unassigned geometric values will adopt measurements from previously established models. Once all the values are attained, a generic model will then be created in SolidWorks.

5.1.1 Calculations for CAD model

Initially, ramjet engine equations were simplified in Chapter 4. However, to incorporate the effect of shocks, derivations in this chapter revert to the original parametric relationships. The original equation of exit velocity with respect to Mach and speed of sound is displayed in equation 5.1. The simplified form of equation 5.1 is inserted into equation 5.2 which represents the specific thrust of an ideal ramjet.

$$V_5 = M_5(a_5) \rightarrow \frac{V_5}{a_o} = \frac{M_5\sqrt{\gamma RT_5}}{\sqrt{\gamma RT_o}} \rightarrow \frac{M_5\sqrt{T_5}}{\sqrt{T_o}} \rightarrow \frac{V_5}{a_o} = M_o\sqrt{\frac{\tau_\lambda}{\tau_r}} \quad (5.1)$$

$$\frac{F_T}{\dot{m}_o} = \frac{a_o}{g_o} \left(\frac{V_5}{a_o} - M_o \right) \quad (5.2)$$

Optimum freestream Mach number and diffuser temperature ratio can be derived from specific thrust by taking the partial differential of equation 5.2 with respect to initial Mach number. Equation 5.3 is the result of the partial differential.

$$\sqrt{\frac{\tau_\lambda}{\tau_r}} - 1 = \sqrt{\frac{\tau_\lambda (\gamma - 1) M_o^2}{2\tau_r}} \quad (5.3)$$

The definition of tau r stated in equation 5.4 is substituted into equation 5.3. This will allow the partially differentiated formula to be in terms of one variable.

$$\tau_r - 1 = \frac{\gamma-1}{2} M_o^2 \quad (5.4)$$

After all the simplifications and calculations are conducted, equations 5.5 and 5.6 are optimized with respect to tau r and freestream Mach number.

$$\tau_{r_{\max}} = \sqrt[3]{\tau_\lambda} \quad (5.5)$$

$$M_{o_{\max}} = \sqrt{\frac{2}{\gamma-1} (\sqrt[3]{\tau_\lambda} - 1)} \quad (5.6)$$

Tau r and M_o are functions of tau lambda which is equivalent to total temperature at the end of the combustor and freestream static temperature. From the mission specifications, cruise altitude for the airbreathing stage is around 82,000 ft. Utilizing the Standard Atmosphere chart: density, pressure and temperature are extracted from the desired altitude. Total temperature at the combustion chamber is assumed to be 2200K. This temperature was extracted from a CFD simulation of the X-43A, the only airbreathing scramjet engine that achieved Mach 9 speeds. Inputting all these values back into equations 5.5 and 5.6 yields a maximum Mach number of 2.41 and tau r value of 2.165. Due to oblique shocks some of the energy is dissipated from heat and frictional losses which reduces the mass flow rate at the inlet's throat. Regardless, the capture area for the proposed model was determined from SR-71's data. Utilizing Blackbird's capture area, top Mach speed and speed of sound at 85,069 ft, a mass flow rate of 2086.24 kg/sec was calculated [54]. Consequently, the inlet's capture area can be deciphered from freestream density, Mach number, speed of sound and mass flow rate, as observed from equation 5.7.

$$\frac{\dot{m}_{o_i}}{\rho_i M_i a_i} = A_i \quad (5.7)$$

Similarly, velocity at the inlet throat area is derived from Mach number and speed of sound. To attain the Mach number, initially a theta value for the inlet cone must be assumed. Based on J-58's engine specifications, the inlet cone's half angle was 13°. Therefore, this value will be employed as theta. From figure 5.1, at Mach 2.4 and theta 13° a beta value of 36° is extrapolated.

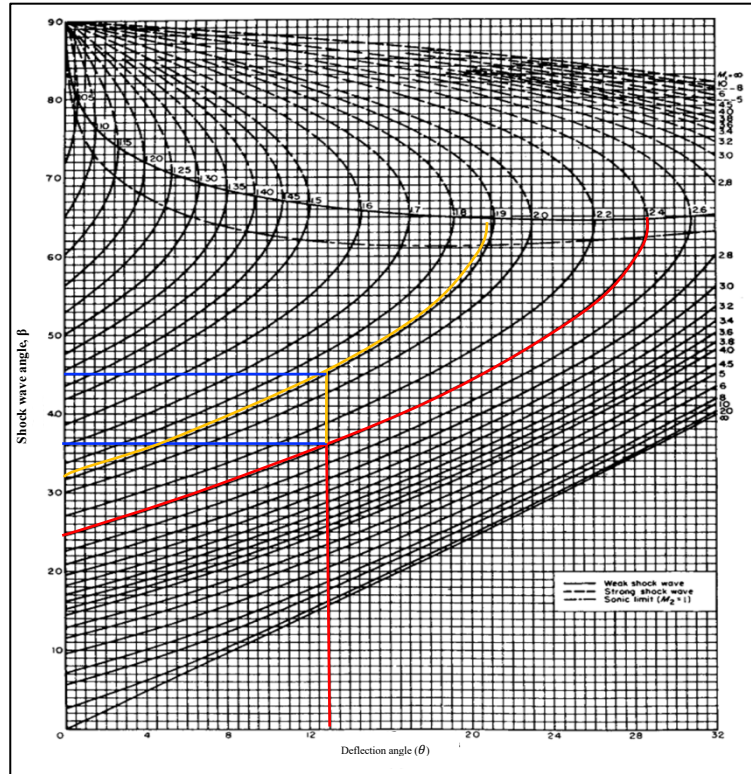


Figure 5.0.1– Theta-beta-Mach diagram [50]

Utilizing equations 5.8, 5.9 and figure 5.1, Mach at the inlet has a value of 1.87. Both equations displayed below are derived from the oblique shock relations. Figure 5.2 is the list of the corresponding properties downstream of the shock at specific Mach numbers.

$$M_{n,o} = M_o \sin(\beta) \quad (5.8)$$

$$M_1 = \frac{M_{n,1}}{\sin(\beta - \theta)} \quad (5.9)$$

M_1	M_2	p_2/p_1	T_2/T_1	ρ_2/ρ_1	P_{o2}/P_{o1}	P_{o2}/P_1
1.00	1.0000	1.0000	1.0000	1.0000	1.0000	1.8929
1.02	0.9805	1.0471	1.0132	1.0334	1.0000	1.9379
1.04	0.9620	1.0952	1.0263	1.0671	0.9999	1.9844
1.06	0.9444	1.1442	1.0393	1.1009	0.9998	2.0325
1.08	0.9277	1.1941	1.0522	1.1349	0.9994	2.0819
1.10	0.9118	1.2450	1.0649	1.1691	0.9989	2.1328
1.12	0.8966	1.2968	1.0776	1.2034	0.9982	2.1851
1.14	0.8820	1.3495	1.0903	1.2378	0.9973	2.2388
1.16	0.8682	1.4032	1.1029	1.2723	0.9961	2.2937
1.18	0.8549	1.4578	1.1154	1.3069	0.9946	2.3500
1.20	0.8422	1.5133	1.1280	1.3416	0.9928	2.4075
1.22	0.8300	1.5698	1.1405	1.3764	0.9907	2.4663
1.24	0.8183	1.6272	1.1531	1.4112	0.9884	2.5263
1.26	0.8071	1.6855	1.1657	1.4460	0.9857	2.5875
1.28	0.7963	1.7448	1.1783	1.4808	0.9827	2.6500
1.30	0.7860	1.8050	1.1909	1.5157	0.9794	2.7136
1.32	0.7760	1.8661	1.2035	1.5505	0.9758	2.7784
1.34	0.7664	1.9282	1.2162	1.5854	0.9718	2.8444
1.36	0.7572	1.9912	1.2290	1.6202	0.9676	2.9115
1.38	0.7483	2.0551	1.2418	1.6549	0.9630	2.9798
1.40	0.7397	2.1200	1.2547	1.6897	0.9582	3.0492
1.42	0.7314	2.1858	1.2676	1.7243	0.9531	3.1198
1.44	0.7235	2.2525	1.2807	1.7589	0.9476	3.1915
1.46	0.7157	2.3202	1.2938	1.7934	0.9420	3.2643
1.48	0.7083	2.3888	1.3069	1.8278	0.9360	3.3382
1.50	0.7011	2.4583	1.3202	1.8621	0.9298	3.4133

Figure 5.0.2 – Part of the normal shock properties [51]

Both temperature and density can be derived from isentropic relations shown in equations 5.10 and 5.12. Area at the inlet throat provides the distance between the engine cowl and maxima of the shock cone for the CAD model. Once the airflow passes the inlet throat, diameter increases to maximize the contact points of the incoming air with the precooler.

$$\frac{T_{To}}{T_o} = 1 + \frac{\gamma-1}{2} M_o^2 \quad (5.10)$$

$$T_{T1} = T_{To} \rightarrow \frac{T_{T1}}{T_1} = 1 + \frac{\gamma-1}{2} M_1^2 \quad (5.11)$$

$$\frac{\rho_{to}}{\rho_o} = \left(1 + \frac{\gamma-1}{2} M_o^2\right)^{\frac{1}{\gamma-1}} \rightarrow \rho_{T1} = \rho_{To} \rightarrow \frac{\rho_{T1}}{\rho_1} = \left(1 + \frac{\gamma-1}{2} M_1^2\right)^{\frac{1}{\gamma-1}} \quad (5.12)$$

Since all the data for airbreathing engine were based on ideal cycles, it is safe to also assume the fluid is governed by ideal gas laws. Therefore, the pressure at the combustion chamber is calculated using equation 5.13. All the results are summarized in table 5.1.

Table 5.0.1 – Calculated values of all the variables listed above

Variables	Values	Units
T_{T0}	468.34	K
T_1	275.59	K
ρ_{t0}	0.57	kg/m ³
ρ_1	0.152	kg/m ³
$M_{0 \max}$	2.41	
$\tau_{r \max}$	2.17	
Assumptions	Values	Units
T_c	2200	K
\dot{m}_o	2086.24	kg/sec
θ	13°	degrees

The expansion ratio, thrust force and mass flow rate values are extracted from the rocket's design point in MATLAB. From equation 5.13, pressure ratios across the oblique shocks will provide the pressure at the end of the third shock. Utilizing equations 5.8 and 5.9 and assuming the same theta value from the inlet cone, Mach number tabulated after the reflected shock is 1.446. However, the pressure ratios will be extracted from figure 5.2, where P_2/P_0 is a function of $M_{n,0}$ while P_3/P_2 is a function of $M_{n,2}$. These values are the static pressures of the compressor. Since the static pressure is isentropically related to the total pressure at station 3, equation 5.14 can be utilized.

$$P_3 = P_0 * \left(\frac{P_2}{P_0}\right) \left(\frac{P_3}{P_2}\right) \quad (5.13)$$

$$\frac{P_{t3}}{P_3} = \left(1 + \frac{\gamma-1}{2} M_0^2\right)^{\frac{\gamma}{\gamma-1}} \quad (5.14)$$

Furthermore, due to ideal cycle assumption of the ramjet, the pressure ratio across the combustion chamber is equivalent to one. Therefore, the combustion chamber pressure is equivalent to 74,374.45 Pascals. Inputting the values denoted by the rocket's design point; the coefficient of thrust is extrapolated by utilizing equation 5.15.

$$C_F = \frac{F_T}{P_c(A^*)} \quad (5.15)$$

5.2 Method of Characteristics

Since the optimal Mach number is determined, through method of characteristics an approximate nozzle contour can be derived. This method plots several characteristic lines across the 2D plot, from which the nozzle wall design will formulate. The more characteristic lines are employed, the more accurate results are produced. Furthermore, at the beginning of this process, the number of characteristic lines determine the number of initial guesses of coordinates at the throat. Once the data for the initial set of characteristic lines is calculated, through the Prandtl-Meyer relations the Mach number at each point is tabulated. Mach number is extrapolated from the Prandtl-Meyer function and Mach angle chart found in Appendix C from Fundamentals of Aerodynamics [40]. This provides the Mach angle where the slope and position of the new points can be attained from. Figure 5.3 depicts the basic values and variables calculated for this process.

No of Characteristic lines	θ	$d\theta$	Point 1													
7	21.81	3.58833333	0.28													
Point	K-	K+	θ	θ_{rad}	ν	ν_{rad}	M	μ	deg	SLOPE	slope	SLOPE	slope (i-(i+1))	X	y	
a			0.28	0.00488692	0.28	0.00488692	1.034	1.3136434	75.2661905					0.01	1.00002388	
b			3.86833333	0.06751518	3.86833333	0.06751518	1.21	0.97276619	55.7353732					0.153	1.006	
c			7.45666667	0.13014344	7.45666667	0.13014344	1.345	0.83828066	48.0299232					0.295	1.022	
d			11.045	0.1927717	11.045	0.1927717	1.465	0.75130613	43.0466517					0.436	1.048	
e			14.63333333	0.25539996	14.63333333	0.25539996	1.587	0.68170738	39.0589393					0.574	1.084	
f			18.2216667	0.31802821	18.2216667	0.31802821	1.715	0.6225275	35.668183					0.71	1.13	
g			21.81	0.38065647	21.81	0.38065647	1.837	0.57563291	32.9813221					0.841	1.186	
1	0.56	0	0.28	0.00488692	0.28	0.00488692	1.034	1.3136434	75.2661905	a1	-3.7284644	1,2	2.4231776	0.27821334	0	
2	7.73666667	0	3.86833333	0.06751518	3.86833333	0.06751518	1.21	0.97276619	55.7353732	b2	-1.2738385	2,3	1.57241996	0.50718135	0.55483017	
3	14.91333333	0	7.45666667	0.13014344	7.45666667	0.13014344	1.345	0.83828066	48.0299232	c3	-0.8562949	3,4	1.4170203	0.62472502	0.73965817	
4	22.09	0	11.045	0.1927717	11.045	0.1927717	1.465	0.75130613	43.0466517	d4	-0.6249098	4,5	1.37093943	0.71797293	0.87179236	
5	29.2666667	0	14.63333333	0.25539996	14.63333333	0.25539996	1.587	0.68170738	39.0589393	e5	-0.4541593	5,6	1.36588072	0.79841844	0.98207828	
6	36.44333333	0	18.2216667	0.31802821	18.2216667	0.31802821	1.715	0.6225275	35.668183	f6	-0.314273	6,7	1.39373073	0.86992035	1.07974136	
7	43.62	0	21.81	0.38065647	21.81	0.38065647	1.837	0.57563291	32.9813221	g7	-0.1974853	7,8	1.41713587	0.93310932	1.16780976	
8	43.62	0	21.81	0.38065647	21.81	0.38065647	1.837	0.57563291	32.9813221	g8	0.40017412			0.98724115	1.24452192	
9	7.73666667	-7.7366667	0	0	7.73666667	0.13503036	1.357	0.82850214	47.4696557	2,9	-1.1778407	9,10	1.06357431	0.9782384	0	
10	14.91333333	-7.7366667	3.58833333	0.06262826	11.325	0.19765862	1.481	0.74126217	42.4711756	3,10	-0.8310438	10,11	1.02893361	1.21357503	0.250298	
11	22.09	-7.7366667	7.17666667	0.12525652	14.91333333	0.26028688	1.61	0.67016845	38.3978073	4,11	-0.6154786	11,12	1.02925537	1.40602182	0.44831297	
12	29.2666667	-7.7366667	10.765	0.18788477	18.5016667	0.32291514	1.73	0.61631819	35.3124159	5,12	-0.4554422	12,13	1.05767428	1.57914603	0.62650199	
13	36.44333333	-7.7366667	14.35333333	0.25051303	22.09	0.3855434	1.847	0.57212339	32.7802417	6,13	-0.3236991	13,14	1.1027972	1.74106001	0.79775424	

Figure 5.0.3 - General variables and calculations for method of characteristics

The nozzle's throat area was assumed to be one for simplifying the calculations, this number was inputted as the initial y point and then incremented by 0.01 for the other six points near the throat. From the desired Mach number and Prandtl-Meyer chart, the ν value is extracted which is half of the theta (θ) value. The derivative of theta ($d\theta$) is calculated from the difference of the first point and theta, divided by the difference between the number of characteristic lines and point 1. Since the first set of numbers are guesses, the characteristic values (K-, K+) and slopes are non-existent. Once all the values are extracted from this process, the nozzle contour and the characteristic lines are plotted in figure 5.4.

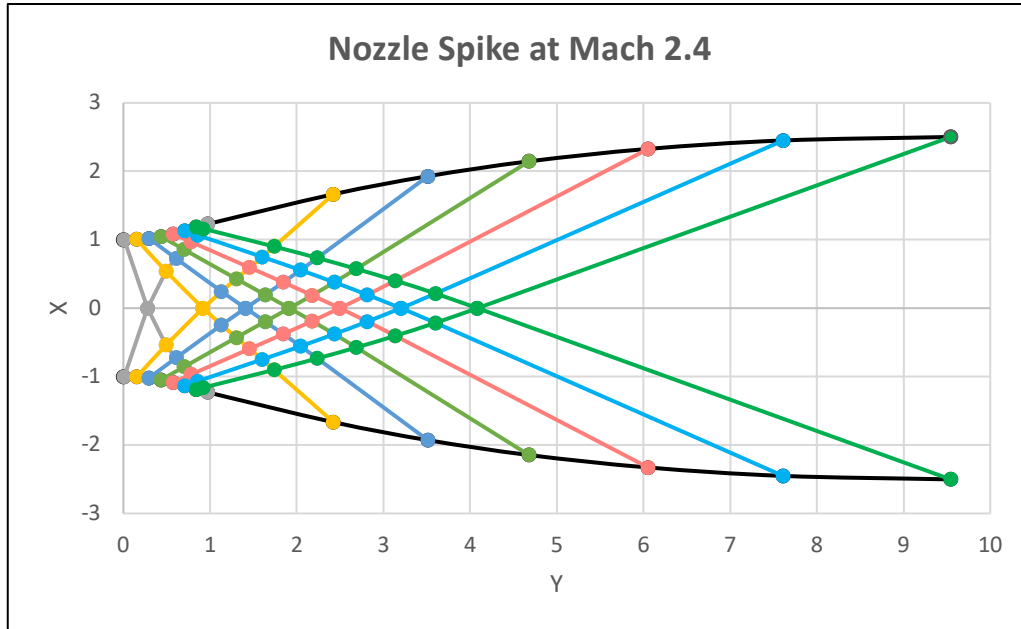


Figure 5.0.4– Contour of the nozzle at the desired Mach number

Even though seven characteristic lines are the standard number of lines, the results are at best approximate. Furthermore, to generate smooth results, the throat radius was assumed to be 1.0. This value deviates 0.435 units from the calculated throat radius. Therefore, the coordinates observed in figure 5.4 cannot be utilized for length, or radii measurements of the nozzle. Rather, the parabolic nozzle equation developed by Rao and Shmyglevsky can be utilized to determine the length [47]. Equation 5.16 depicts the relation of the length to expansion ratio, percent length of conical nozzle and the deflection angle of the flow at the end of the nozzle. The percent length is derived from figure 5.5.

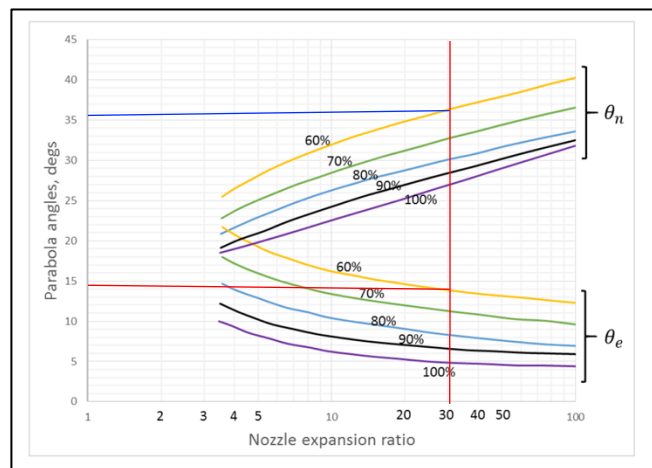


Figure 5.0.5 - Parabolic nozzle relations

This figure is a relation between the expansion ratio, parabolic angles and deflection angles. Typically, the standard “percent bell” or the nozzle length when compared to a conical nozzle with the same expansion ratio, is about 80%. However, the expansion ratio expected for this nozzle will be in the higher spectrum, especially when this engine has to propel a gross take-off weight of 1.56E6lbs, adding more weight will render this model ineffective. Thus, a minimum percent bell of 60 is selected to generate optimal values for this model. Based on this value, the correlating deflection angle is 14.25 degrees and 35.5 degrees for the parabolic angle. These values are inserted into equation 5.6, where kappa refers to the percent bell, epsilon is the expansion ratio, R_{th} is the radius at the throat and θ_e is the deflection angle [48].

$$L_N = \frac{\kappa(\sqrt{\epsilon_{er}}-1)R_{th}}{\tan(\theta_e)} \quad (5.16)$$

Overall length is presented in the table 5.2 and utilized for the CAD model of the nozzle in figures 5.6 to 5.9.

5.3 Discussion and Conclusion

All tabulated results are displayed in table 5.2. Since shocks were inevitable for these types of engines, to derive more realistic dimensions oblique shock equations were utilized. On the other hand, derivations of rocket equation and exit velocity were employed to assess the proper parametric values for the rocket engine. Furthermore, method of characteristics was employed to attain a general shape of the nozzle. Since only seven characteristic lines were used for this process, the x and y coordinates displayed in figure 5.3 are replaced by the calculated values of the nozzle’s length, radii, throat and exit areas.

Through the previously presented equations and derived design points, the chamber pressure, areas and expansion ratio were extrapolated and displayed in table 5.2.

Table 5.0.2 – Engine's calculated dimensions and parameters

Variables	Values	Units
$M_{n,1}$	0.7314	
$M_{n,2}$	0.7664	
M_1	1.87	
M_2	1.446	
A_i	2.395	m^2
D_i	1.746	m
β_1	45°	degrees
β_o	36°	degrees
P_o	2810	Pa
P_2/P_o	2.186	
P_3/P_2	1.928	
C_F	1.725	
F_T	129784.36	N
ε	31.67	kg/m^3
P_c	2345022.1	Pa
A^*	1.00	m^2
A_e	31.76	m^2
D^*	1.13	m
D_e	6.36	m
L_N	6.177	m

The key parameters utilized for the CAD model include the inlet's capture area diameter (D_i), nozzle throat diameter (D^*) and nozzle exit diameter (D_e). Once these values were inputted into the system, the generated CAD model is displayed in figures 5.6 to 5.9. Each figure displays different views of the proposed engine.

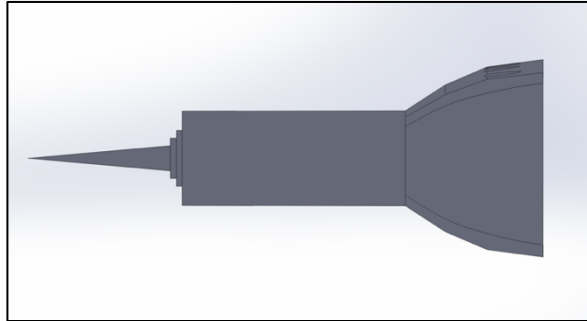


Figure 5.0.6 – Left view of the proposed model

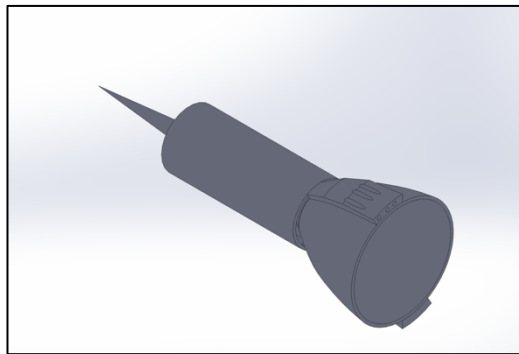


Figure 5.0.7 – Rear view of the proposed model

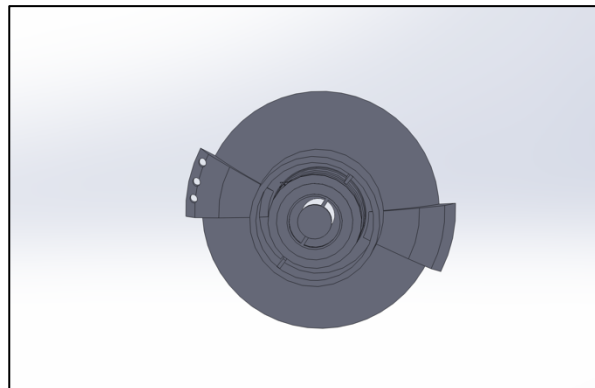


Figure 5.0.8 – Front view of the proposed model

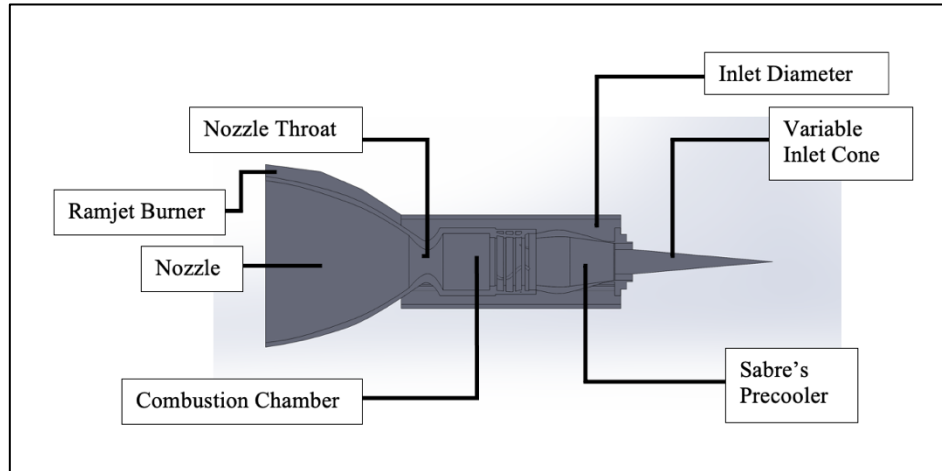


Figure 5.0.9 – Cut view of the proposed model

Chapter 6 – Redesigning the Current Model

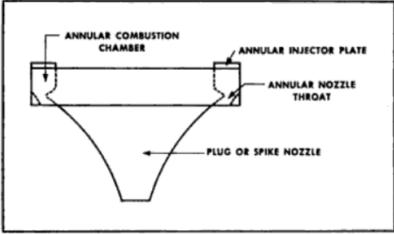
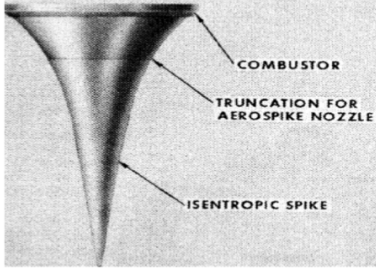
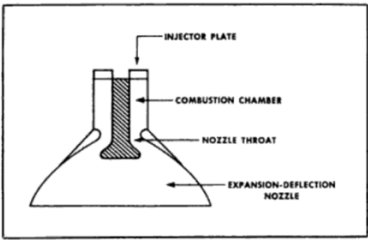
6.1 Introduction

The current model is very similar to the design of the SABRE engine. Although this model is based on the calculated design point, it is not fully optimized. For instance, the inlet and outlet performance are two of the most vital areas that an airbreathing engine can lose a lot of efficiency when not properly designed. Furthermore, the inlet for an airbreathing engine is one of the most challenging areas to optimize and currently under a lot of research. Due to fewer moving parts, the inlet of an airbreathing engine directly effects the combustion pressure which is vital for ignition and optimized thrust. Therefore, a newer inlet design will be considered for increasing the performance of this engine through various Mach regimes. However, inlet is not the only area that could be enhanced. The current model only shows a crude outline of where the combustion chamber is located. So, after revising the inlet, a combustion chamber that can incorporate rocket and air-breathing mode efficiently will also be reviewed. On the other hand, the outlet performance of a nozzle can be increased with a simple design that generates ideal expansion throughout various pressure levels. Therefore, converting the current nozzle into an aerospike design can increase the engine's overall efficiency and thrust output. There are a few aerospike designs that will be reviewed in this chapter. Consequently, a rendering of a 3D model will populate the necessary dimensions and CAD to test all three design modifications through CFD analysis.

6.1.1 Designing Aerospike Nozzle

Table 6.1 displays a few of the possible configurations of an aerospike and list their benefits and disadvantages. Out of the various options, two possible configurations are considered for an aerospike nozzle: linear and expansion deflection nozzle.

Table 6.0.1 - Comparison chart between different aerospike models

Configuration	Advantages	Disadvantages
<p>Linear Aerospike</p> 	<ul style="list-style-type: none"> • Structural rigidity • Lightweight • Differential throttling • Greater altitude compensation • Can be truncated 	<ul style="list-style-type: none"> • Complex design • Multiple and smaller nozzles required • Annular combustion chambers
<p>Toroidal Aerospike</p> 	<ul style="list-style-type: none"> • Easily retrofitted into conventional design • Light weight 	<ul style="list-style-type: none"> • No differential throttling • The tip of the spike melts • Lesser range of maintaining ideal expansion • Need longer length
<p>Expansion-Deflection Aerospike</p> 	<ul style="list-style-type: none"> • Structural rigidity • Wider altitude compensation range than linear • Easiest implementation on the bell nozzle • Light weight combustion chamber • Can be employed in vacuum 	<ul style="list-style-type: none"> • Unable to cool the plug effectively • No differential throttling • Increase in structural weight

Three major advantages of a linear aerospike are the capacity to reduce the overall weight of the spacecraft, generate differential throttling, and is a technology readiness level of 3. On the other hand, expansion-deflection nozzle has better control on back-pressure variations, does not require change in designed area ratio and is smaller in length when compared to other internal-flow nozzles. This reduces structural weight which makes it ideal for a lightweight design. The only downside to this type of nozzle is the difficulty of keeping the central plug cooled. If the plug is deformed or non-functional then all the benefits generated by this aerospike will be lost.

Linear aerospike also has its own disadvantages, two of which include complexity in adding smaller rocket nozzles and configuring the combustion pipelines to bend around the unique shaped nozzle. Despite this complex design and requirements, the overall structural rigidity is stable and does not require additional reinforcements. After considering all the aspects of each design, linear aerospike seems to be the most advantageous selection for the overall engine model.

Since the linear aerospike is an inverted bell nozzle, the contour calculated from Chapter 5 will be employed and each contour will be translated inversely to generate a cone shape. Figure 6.1 depicts the final shape. Truncating the nozzle will help reduce the overall weight of the engine. However, higher truncation values reduce thrust efficiency during over-expansion [44]. There was a study conducted in Embry-Riddle University, where varying truncated nozzles were simulated in the same conditions to compare their effect on thrust efficiencies. Based on this study, 20% truncated nozzle outperformed the other truncated nozzles when tested at combustion pressures of 58atm and 15atm [49]. Therefore, our design will also be truncated by 20% which generates a value of 4.94m represented in the diagram below by a vertical line.

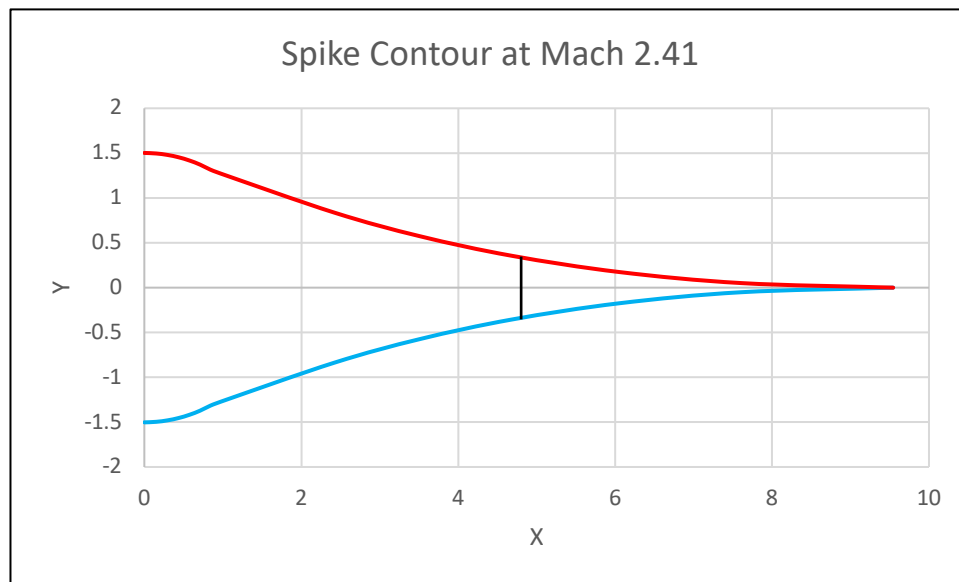


Figure 6.0.1 - Aerospike contour using method of characteristics

Based on all the data provided and previous length of the nozzle, a revised CAD model of the aerospike is produced and displayed in figure 6.3. All the dimensions displayed in figure 6.2 are in meters and the thickness of the linear spike is 0.1m.

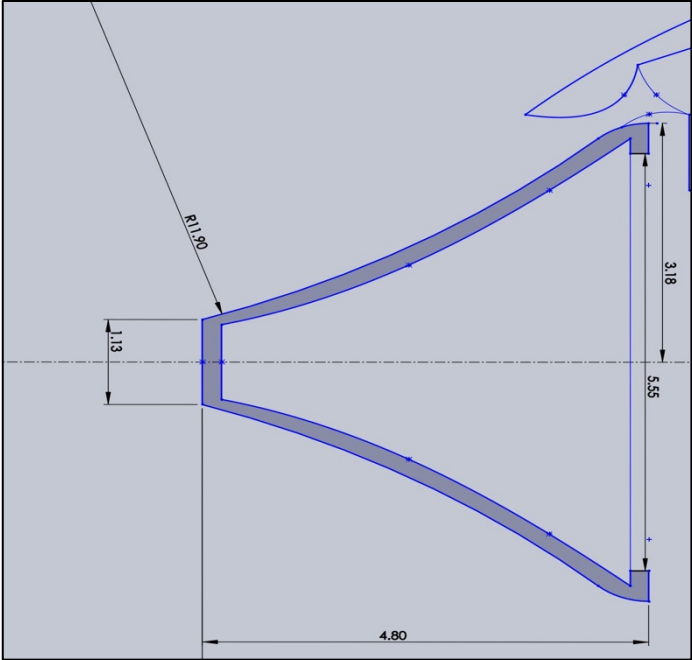


Figure 6.0.2 - Dimension of linear aerospike

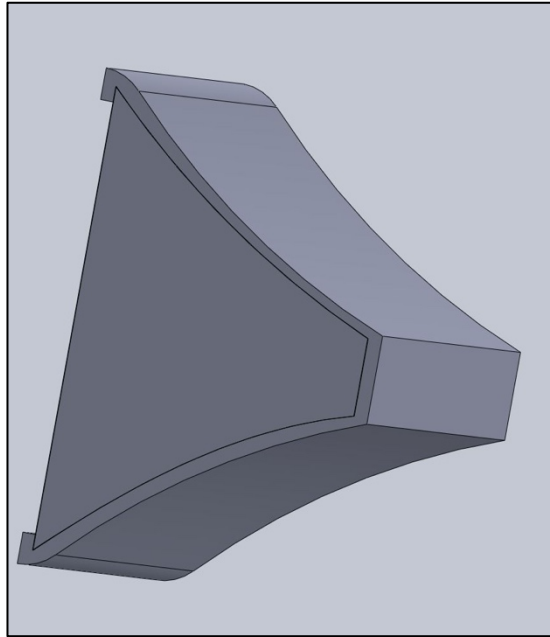


Figure 6.0.3 - Back view of the linear aerospike

6.1.2 Designing Combustion Chamber

The basic components of a combustion chamber are the fuel, oxidizer, and igniter. This is common throughout different types of engines. However, as discussed earlier, the combustion chamber for a rocket engine is not exposed to its surrounding environment while combustion chambers for jet engines are open to its environment. Therefore, to combine a closed and open system, movable flaps are required. These flaps will provide the desirable conditions for both modes during the flight path. Rocket mode will be prevalent from static to initial cruise conditions while air-breathing mode will be dominant during cruise to specific hypersonic speeds. Both modes will share a combustion chamber to reduce the complexity of the design. Oxidizer will only be pumped during rocket mode while fuel is pumped throughout the entire flight plan. During air breathing mode, the incoming air will act as the oxidizer in the combustion chamber while the precooler generates liquid oxygen which will be stored as the oxidizer for the mission in space. For the rocket mode a fuel tank and oxidizer tank will be designed in the fuselage of the spaceplane while pumps will feed these propellants into the combustion chamber. There will be bleed vanes between the precooler and combustion chamber to employ some of the incoming air as a cooling gas for the nozzle and combustion chamber.

Rest of the air will be fed into the chamber for ignition. Figures 6.4 and 6.5 are the CAD model for the proposed combustion chamber.

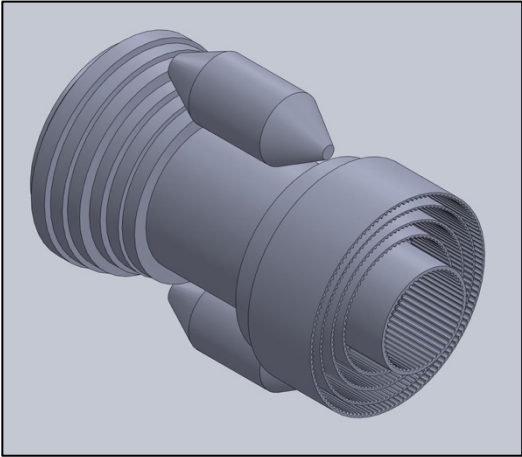


Figure 6.0.4 - Isometric view of the combustion chamber with the pre-cooler

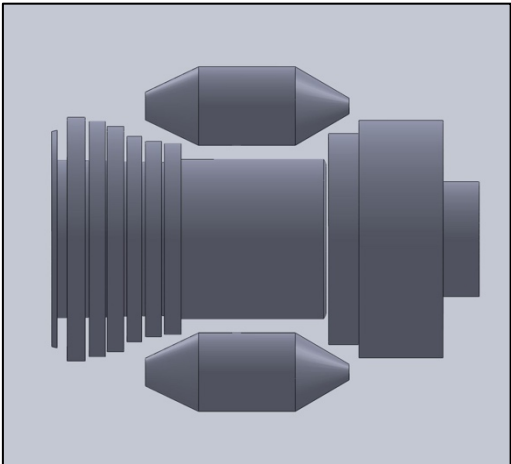


Figure 6.0.5 - Front view of the combustion chamber

6.1.3 Designing Inlet

Inlet design is imperative for proper functioning of the engine. Turbojets and turbofans have a small void between the engine cowl and the compressor that allows air to laminarly flow into the engine. Laminar flow is mostly present during subsonic and transonic speeds. However, during supersonic flows, shocks are more dominant than laminar flow which makes the ducted

void a poor choice for the proposed model. On the other hand, turboramjets employ inlet cones while some scramjets employ inlet ramps to compress and control the high-speed flow. Both designs slow down the incoming air for improved fuel mixing and ignition processes.

Furthermore, their variable lengths allow the incoming shocks to be fixed in their location, angle, and number of shocks during different supersonic speeds. Inlet cones are heavier, expensive, produce more pressure losses and cannot operate at different angles of attack [39]. Regardless of all these disadvantages, shock cones can reduce the flow when compared to inlet ramps [40].

Since there are other components added to this engine which cannot operate at high hypersonic velocities, an inlet cone would can satisfy the velocity requirement. Even though an inlet cone can produce desired velocities inside the engine, adding ramps at the engine cowl could increase the pressure recovery further. Therefore, a variable inlet cone with double ramps is incorporated into the model. Figures 6.6 and 6.7 are the CAD model for the proposed inlet configuration.

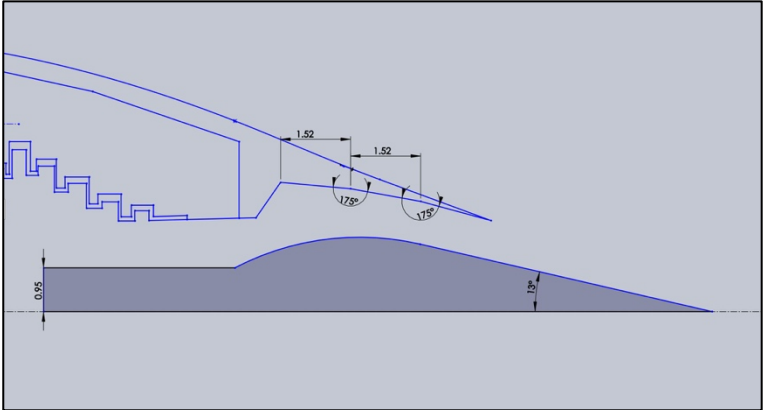


Figure 6.0.7 - Dimensions for the inlet cone

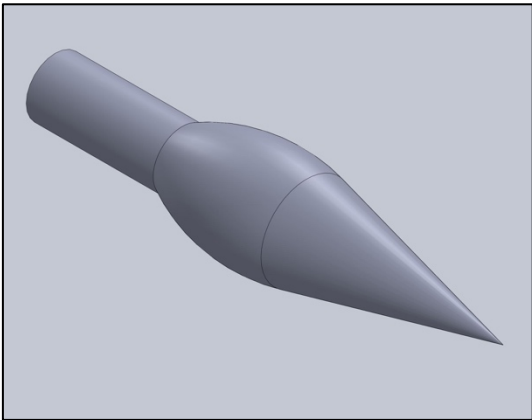


Figure 6.0.6 - Isometric view of the inlet cone

6.2 New 3D CAD Model and Dimensions

Based on the new design choices for the inlet, combustion chamber and nozzle a revised CAD model was developed in SolidWorks. The new design are displayed in figures 6.8 to 6.9. Figure 6.8 displays all the interior designs of the engine including the precooler while figure 6.9 displays the shape of the outer engine cowl.

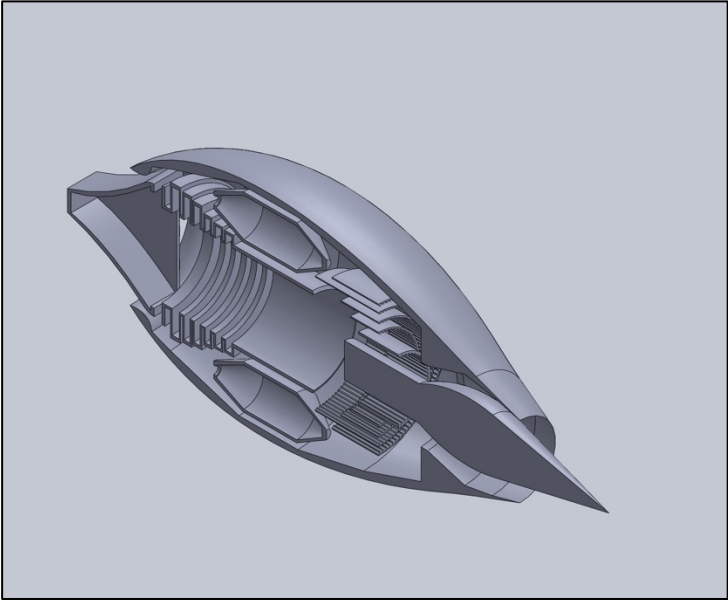


Figure 6.0.8 – Isometric view of aerospike

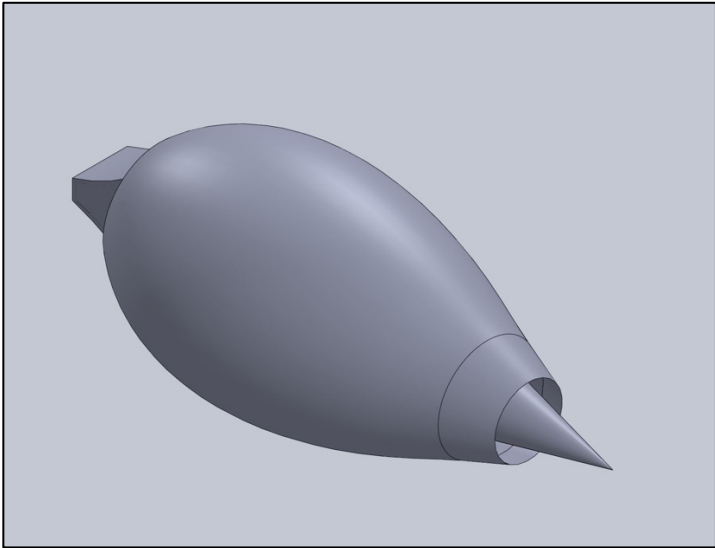


Figure 6.0.9 – Sliced view of the proposed model

The current engine cowl design will generate drag at hypersonic speeds due to its non-aerodynamic curvature. However, this can be easily repaired by placing the two rocket chambers horizontally instead of vertically. This will cause the engine cowl to have a horizontally oblong shape which will reduce the height and increase the width. The height of the width can be reduced to a point, to generate a similar shape of the SR-71 fuselage.

6.3 2D CFD Simulation and Results

Due to the complexity and computational power required to run a 3D simulation, a 2D model will be simulated in CFD to observe the aerodynamic performance. Through the 2D analysis, new revisions can easily be made to the 3D model in areas that are not producing the desired outcomes. Therefore, the model's 2D profile was imported from SolidWorks into Fluent Ansys and the performance around the inlet and outlet of the engine were highlighted. Figures 6.12 to 6.23 provide results of total pressure, total temperature, Mach number and turbulent kinetic energy. The engine was tested in two altitudes: one at 24,993.6m with an ambient pressure of 2527.3Pa and the other at sea-level conditions.

6.3.1 Navier Stokes Equation

Sir Isaac Newton is a revered scientist famous for his discovery of gravity, however he has also contributed many other well-known principles. One of Newton's principles included the three laws of motion: (1) motion will not alter direction or change speed unless acted upon by an external force, (2) force is equivalent to the product of its mass and acceleration, and (3) for every reaction there is an equal and opposite reaction acting on it [42]. Newton's second law and the conservation laws became the foundation for Navier Stokes equations. This set of equations model the behavior of fluids in various conditions. The flow can be viscid, inviscid, laminar, turbulent or a combination of choices. Due to the complexity of assessing the entire flow field, these equations only take into consideration an infinitesimally small element or a finite control volume from which the behavior of the entire flow field can be assumed. These equations can be written in either integral or differential forms. Equations 6.1 to 6.5 express the partial differential form of Navier Stokes equation of mass, momentum, and energy, respectively.

$$\frac{\partial \rho}{\partial t} + \left[\frac{\partial(\rho u)}{\partial x} + \frac{\partial(\rho v)}{\partial y} + \frac{\partial(\rho w)}{\partial z} \right] = 0 \quad (6.1)$$

$$\frac{\partial u}{\partial t} + u \frac{\partial u}{\partial x} + v \frac{\partial u}{\partial y} + w \frac{\partial u}{\partial z} = \frac{1}{\rho} \left[-\frac{\partial p}{\partial x} + \frac{\partial \tau_{xx}}{\partial x} + \frac{\partial \tau_{xy}}{\partial y} + \frac{\partial \tau_{xz}}{\partial z} \right] \quad (6.2)$$

$$\frac{\partial v}{\partial t} + u \frac{\partial v}{\partial x} + v \frac{\partial v}{\partial y} + w \frac{\partial v}{\partial z} = \frac{1}{\rho} \left[-\frac{\partial p}{\partial y} + \frac{\partial \tau_{yx}}{\partial x} + \frac{\partial \tau_{yy}}{\partial y} + \frac{\partial \tau_{yz}}{\partial z} \right] \quad (6.3)$$

$$\frac{\partial w}{\partial t} + u \frac{\partial w}{\partial x} + v \frac{\partial w}{\partial y} + w \frac{\partial w}{\partial z} = \frac{1}{\rho} \left[-\frac{\partial p}{\partial z} + \frac{\partial \tau_{zx}}{\partial x} + \frac{\partial \tau_{zy}}{\partial y} + \frac{\partial \tau_{zz}}{\partial z} \right] \quad (6.4)$$

$$\begin{aligned} \frac{\partial \left(e + \frac{v^2}{2} \right)}{\partial t} + u \frac{\partial \left(e + \frac{v^2}{2} \right)}{\partial x} + v \frac{\partial \left(e + \frac{v^2}{2} \right)}{\partial y} + w \frac{\partial \left(e + \frac{v^2}{2} \right)}{\partial z} = \dot{q} + \frac{1}{\rho} \left[\frac{\partial}{\partial x} \left(k \frac{\partial T}{\partial x} \right) + \frac{\partial}{\partial y} \left(k \frac{\partial T}{\partial y} \right) + \frac{\partial}{\partial z} \left(k \frac{\partial T}{\partial z} \right) - \right. \\ \left. \frac{\partial(pu)}{\partial x} - \frac{\partial(pv)}{\partial y} - \frac{\partial(pw)}{\partial z} + \frac{\partial(u\tau_{xx})}{\partial x} + \frac{\partial(u\tau_{xy})}{\partial y} + \frac{\partial(u\tau_{xz})}{\partial z} + \frac{\partial(v\tau_{yx})}{\partial x} + \frac{\partial(v\tau_{yy})}{\partial y} + \frac{\partial(v\tau_{yz})}{\partial z} + \frac{\partial(w\tau_{zx})}{\partial x} + \right. \\ \left. \frac{\partial(w\tau_{zy})}{\partial y} + \frac{\partial(w\tau_{zz})}{\partial z} \right] \quad (6.5) \end{aligned}$$

The governing equations for the k-ε model is evolved from turbulent kinetic energy, k, reference length, L_e, and eddy viscosity. Kinetic energy are variables of the reference velocity, and characteristic length. From these relations, the equations that determine k-ε model are depicted in equation 6.6 and 6.7 [45].

$$\frac{Dk}{D\tau} = \frac{\partial}{\partial x_j} \left\{ \left(\nu + \frac{\nu_t}{\sigma_{k'}} \right) \frac{\partial k'}{\partial x_j} \right\} - \overline{u_i u_j} \frac{\partial \overline{U_i}}{\partial x_j} - \varepsilon_{DR} \quad (6.6)$$

$$\frac{D\varepsilon_{DR}}{D\tau} = \frac{\partial}{\partial x_j} \left\{ \left(\nu + \frac{\nu_t}{\sigma_{\varepsilon_{DR}}} \right) \frac{\partial \varepsilon_{DR}}{\partial x_j} \right\} - C_{\varepsilon_{DR}1} f_1 \frac{\varepsilon_{DR}}{k'} \overline{u_i u_j} \frac{\partial \overline{U_i}}{\partial x_j} - C_{\varepsilon_{DR}2} f_2 \frac{\varepsilon_{DR}^2}{k'} \quad (6.7)$$

The average velocity components denoted by $\overline{u_i u_j}$ is equivalent to boundary layer thickness, kinetic energy, eddy viscosity and the partial differential of the velocity components as observed in equation 6.8.

$$\overline{u_i u_j} = \nu_t \left(\frac{\partial \overline{U_i}}{\partial x_j} + \frac{\partial \overline{U_j}}{\partial x_i} \right) - \frac{2}{3} \delta_{ij} k \quad (6.8)$$

The variable ν_t with respect to time, ν_t , represents the eddy viscosity which is dictated by a model constant and a model function, as observed in equation 6.9. Model function is related to the dimensionless wall distance and turbulence Reynold's number, as listed below. Additionally, turbulence number is a function of turbulent kinetic energy squared over the product of eddy viscosity and dissipation rate.

$$\nu_t = C_\mu f_\mu \frac{k^2}{\varepsilon_{DR}} \quad (6.10)$$

Depending on the model, some of the constants from equations 6.6, 6.7 and 6.10 might vary; however, the standard values for each constant in these equations are displayed below [45].

- $C_\mu = 0.09$
- $C_{\varepsilon'1} = 1.45$
- $C_{\varepsilon'2} = 1.9$
- $f_1 = 1.0$
- $\sigma_{k'} = 1.4$
- $\sigma_{\varepsilon_{DR}} = 1.3$
- $f_\mu = \left\{ 1 - \exp\left(-\frac{y^+}{26}\right) \right\}^2 \left\{ 1 + \frac{4.1}{\frac{3}{R_t^4}} \right\}$

6.3.2 2D Geometry and Mesh

For conducting a proper CFD simulation, the 2D design had to be modelled in SpaceClaim and imported into the Workbench software. Before the model is imported into Ansys, the type of geometry must be selected. This will provide the proper options for the mesh segment of fluent package. The main goal of meshing is to provide the proper boundaries for the simulation to analyze the model in specific boundary conditions. To attain accurate results, the grid must be as uniform as possible with orthogonal quality greater than 0.1 and skewness below

0.33. At the boundary layers of the model, inflation was employed to provide more accuracy during high velocity simulations. Figure 6.10 display the mesh grid for the aerospike and nozzle. Even though the mesh is not perfectly uniform, this grid produced sufficient quality values thus far.

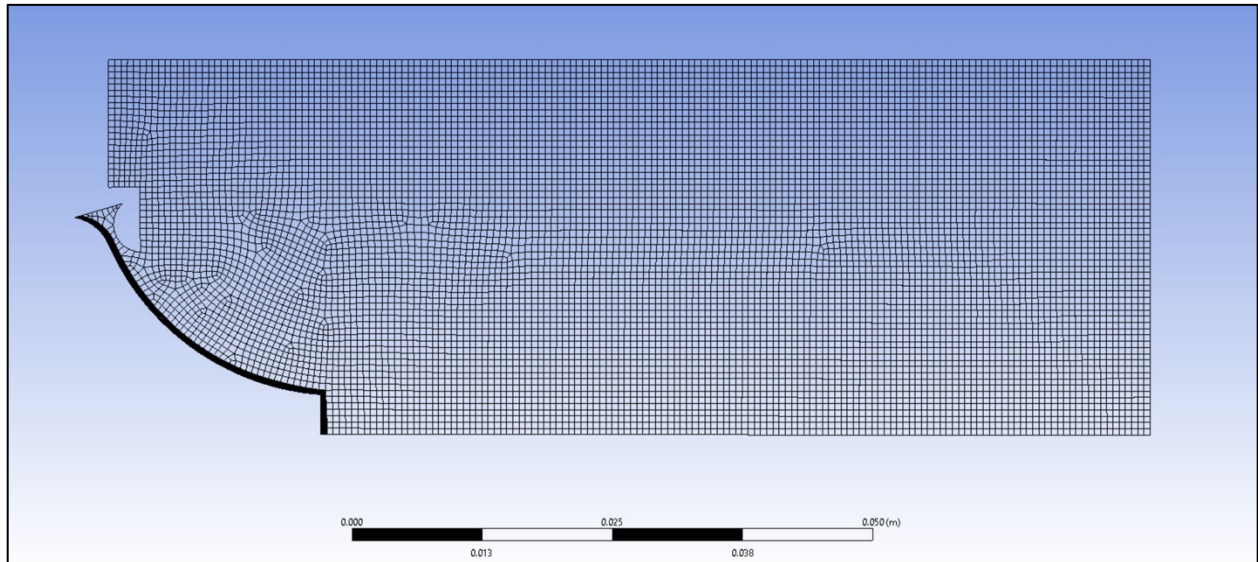


Figure 6.0.10 - Mesh grid for linear aerospike and nozzle

The detailed settings for each selection on this grid are accounted for in table 6.2. Due to certain corners and curvatures in this design, all quadrilateral mesh was impossible. Instead, the Quad/tri option was selected, especially since sharp corners cause specific regions to be easily defined by triangles than squares. Furthermore, the addition of inflation only degraded the skewness of the mesh in those regions.

By slowing down the growth rate of inflation layers, degree of skewness was alleviated in these regions. Furthermore, altering the global maximum of each element size also allowed mesh to have more orthogonal shapes.

Table 6.0.2 - Settings for the mesh grid

Quality	Average Values
Orthogonal	0.9908
Element	0.91947
Skewness	3.1122e-002
Aspect Ratio	1.8147
Mesh	Values
Automatic Method	Quad/Tri
Edge Sizing	0.1 m
<i>Inflation</i>	
Type	Smooth Transition
Transition Ratio	0.1
Maximum Layers	10
Growth Rate	1.0
Quality	Average Values
<i>Statistics</i>	
Nodes	16064
Elements	15768

Conversely, at the inlet, the ramps and shock cone were simulated to assess the pressure recovery and performance of oblique shocks. Due to the large size and symmetry of the cone and cowl, an axisymmetric design was chosen to increase the density of the mesh grid. This will increase accuracy of the simulation results. Inflation was applied at the upper wall of the shock cone, ramps and inner diameter of the inlet area, as observed in figure 6.11.

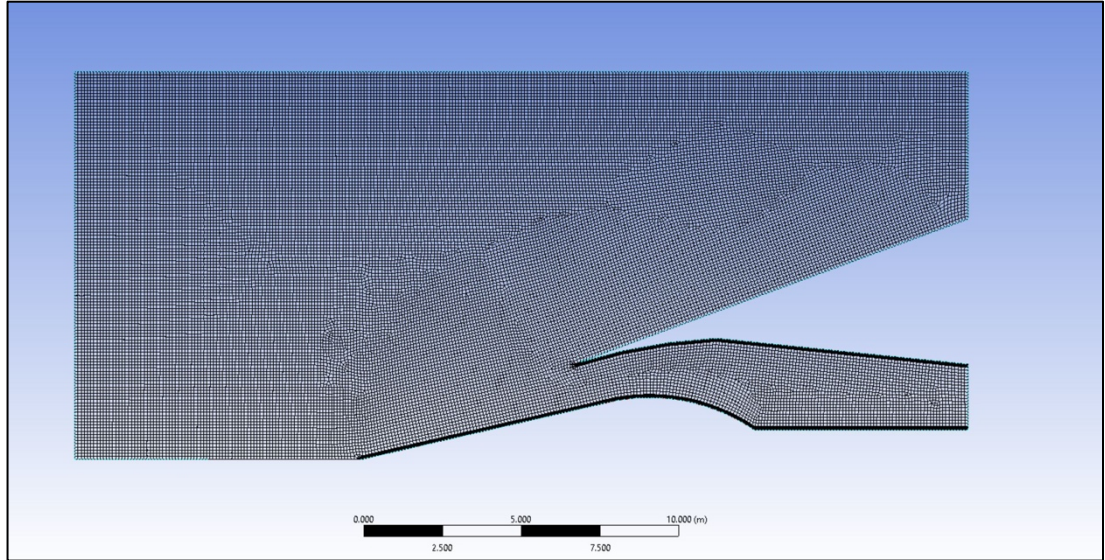


Figure 6.0.11 - Mesh grid for the inlet cone and ramps

There were multiple curvatures and corners on this design than the aerospike nozzle. Therefore, as shown in table 6.3, the reported skew value is higher for this grid than the nozzle's grid. On the other hand, aspect ratio for both models are below 5. Commonly, aspect ratio can be limitless: however, when considering convergence of the energy equation, having an aspect ratio below 35 is ideal. Since both models meet this requirement, the generated grids should suffice to provide appropriate results. Another similar metric among both grids is their orthogonal quality value.

Table 6.0.3 - Settings for inlet and cowl mesh grid

Quality	Average Values
Orthogonal	0.99508
Element	0.87288
Skewness	4.1836E-002
Aspect Ratio	2.1095
Mesh	Values
Automatic Method	Quad/Tri
Face Sizing	0.1 m
<i>Inflation</i>	
Type	Smooth
Transition Ratio	0.1
Maximum Layers	5
Growth Rate	1.0
<i>Statistics</i>	
Nodes	14284
Elements	13384

6.3.3 CFD Simulation

For both test runs, most of the basic settings were similar to each other, as displayed in table 6.4. The only difference between the two models were their boundary condition inputs. At the inlet, due to oblique shocks and unique geometry, pressures observed near the inlet will be different from pressures observed after the combustion process. Pressures at the inlet were calculated in the previous chapter and utilized as inputs for the inlet’s simulation. Sea-level conditions for the aerospike model are presented in table 6.4.

Table 6.4 - Solution inputs for simulating linear aerospike nozzle at sea-level

Selection	Input Values
<i>General</i>	
Type	Density Based
Time	Steady
2D Space	Axissymmetric
Velocity Formulation	Absolute
<i>Models</i>	
Energy Equation	On
Viscosity	k-ε model, Realizable, Standard Wall Function
<i>Materials</i>	
Fluid	Air
Density	Ideal-gas law [kg/m ³]
Specific heat at constant pressure	1006.43 [J/kgK]
Viscosity	Sutherland [kg/ms]
Molecular Weight	28.966 [kg/kgmol]
Thermal conductivity	0.0242 [W/mK]
<i>Boundary Conditions</i>	
Pressure Inlet – Gauge Pressure	1582087.5 [Pa]
Pressure Inlet – Thermal	900 K
Pressure Far-Field – Gauge Pressure	101325 [Pa]
Pressure Far-Field – Mach	0.6
Pressure Far-Field – Thermal	300 [K]
Pressure Outlet – Gauge Pressure	101325 [Pa]
Pressure Outlet – Thermal	300 [K]
Operating Conditions	0 [Pa]
<i>Methods</i>	
Formulation	Implicit
Spatial Discretization - Flow	Second Order Upwind
Spatial Discretization – Turbulent Kinetic Energy	Second Order Upwind

Table 6.4 continued...

Selection	Input Values
Spatial Discretization – Turbulent Dissipation Rate	Second Order Upwind
<i>Monitors</i>	
Residuals	1E-07
<i>Initialization</i>	
Type	Standard Initialization
From	all zones

6.3.4 Results

The minimum iterations for all four cases were set at 300 runs. Figures 6.12 to 6.17 are results of the linear aerospike at sea-level conditions and at design altitude. Design altitude conditions was set at 82,000ft or 24,993.6m with ambient pressure of 2527.3Pa and temperature of 216.66K.

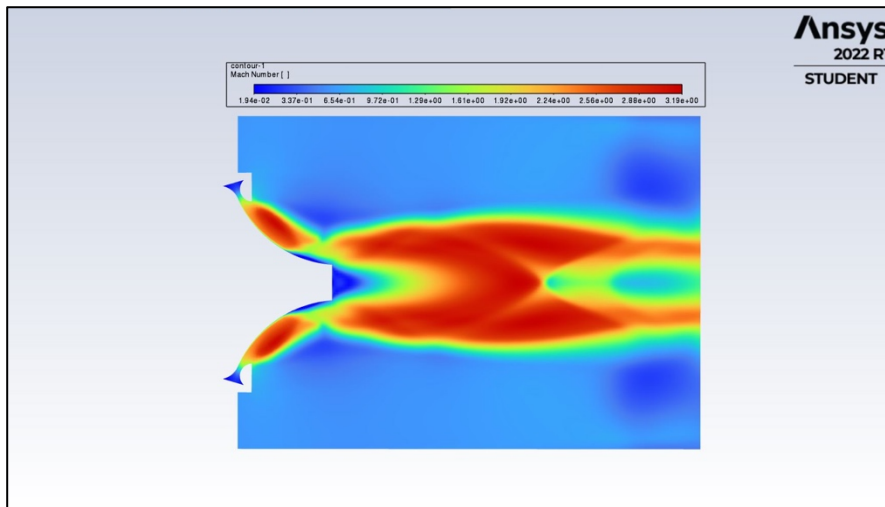


Figure 6.0.12 - Contour of Mach at sea-level

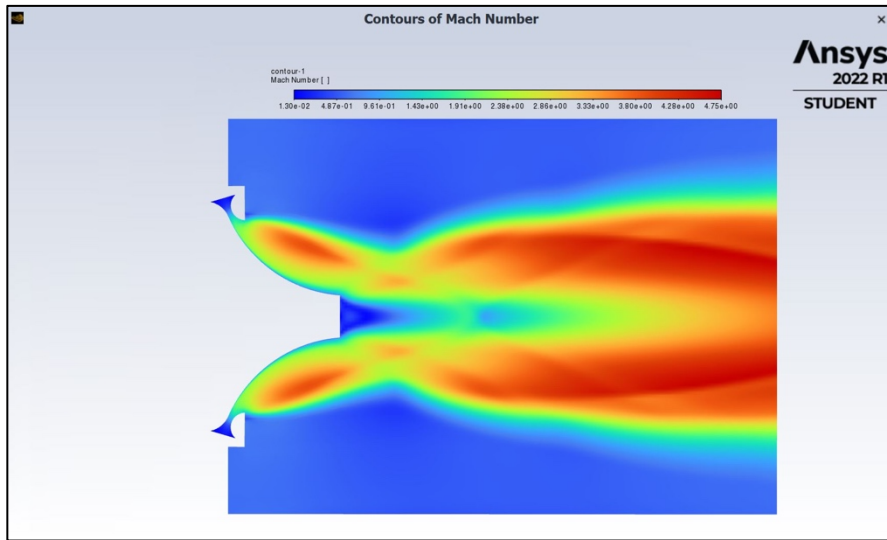


Figure 6.0.13 - Contour of Mach at design altitude

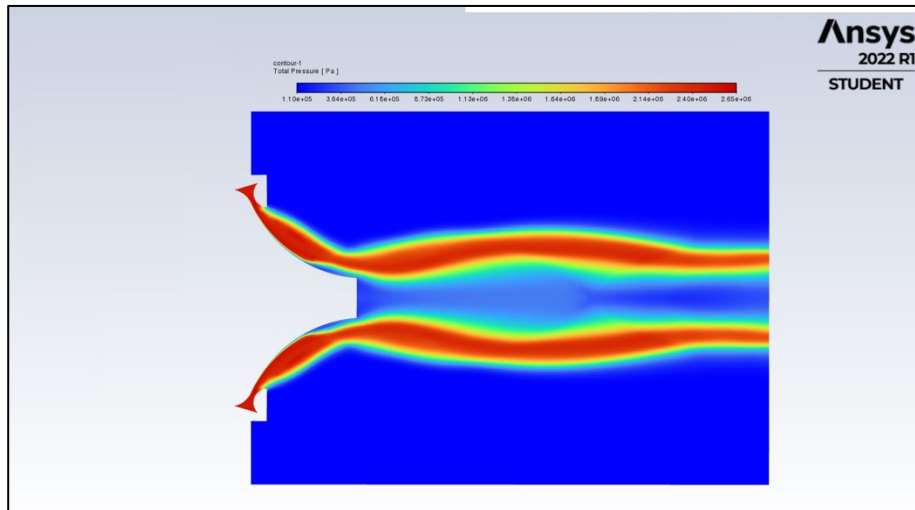


Figure 6.0.14 - Contour of total pressure at sea-level

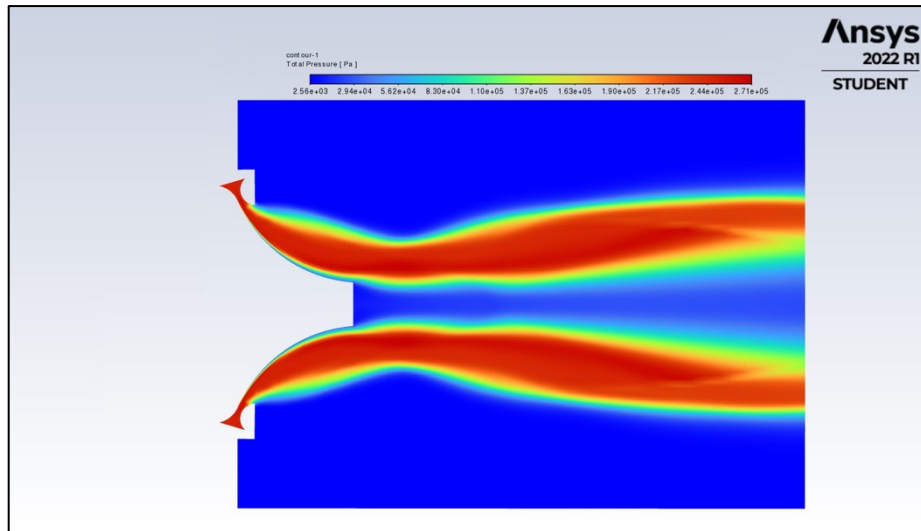


Figure 6.0.15 - Contour of total pressure at design altitude

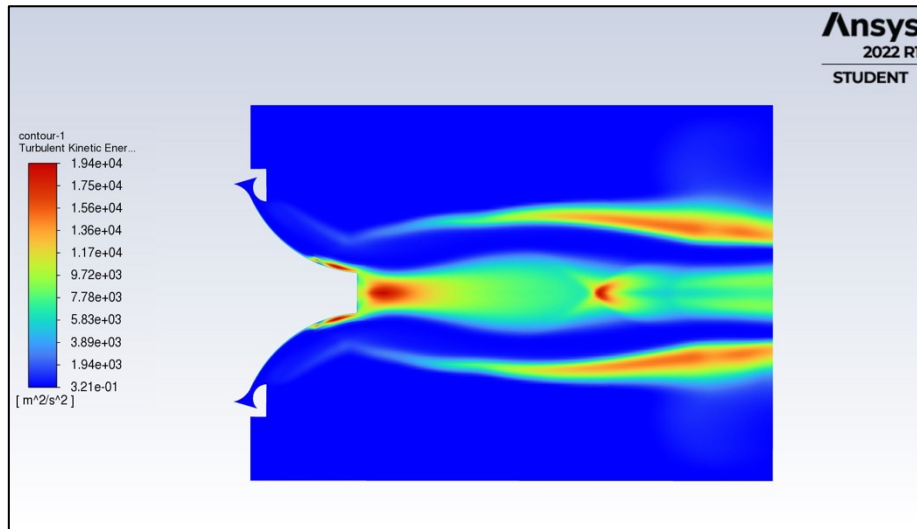


Figure 6.0.16 - Contour of turbulent kinetic energy at sea-level

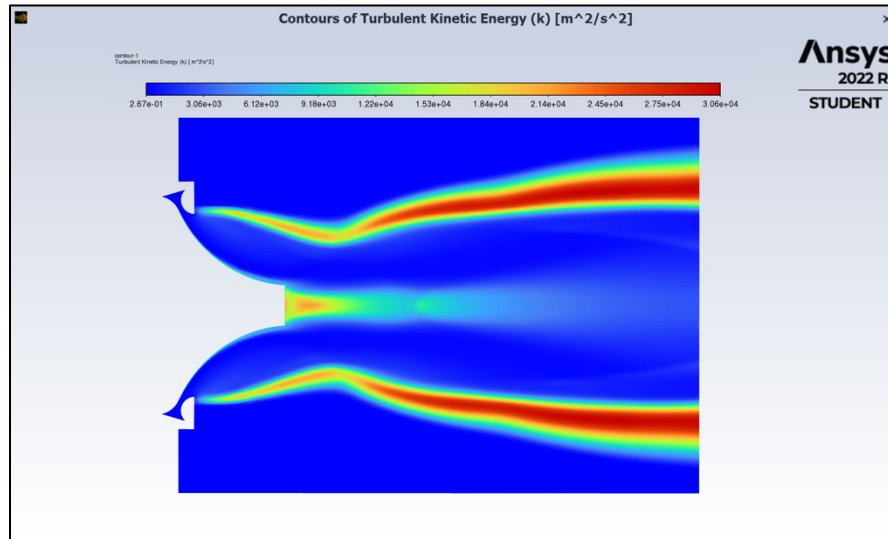


Figure 6.0.17 - Contour of turbulent kinetic energy at design altitude

The inlet was also simulated in similar altitudes as the linear aerospike. Results of Mach, total pressure, and total temperature contours are displayed in figures 6.18 to 6.23. On the other hand, there were some setting differences between the inlet and linear aerospike models. For instance, outlet conditions for the inlet design was not equivalent to the pressure far-field. At sea-level the outlet was set at 725,282.14Pa and 630.11K inside the inlet. However, for design altitude simulations, the outlet was set at 4292.30Pa and 468.34K. Furthermore, at sea-level the pressure inlet was set at 1,504,680.65Pa while at desired altitude the inlet pressure was at 37,530.52Pa.

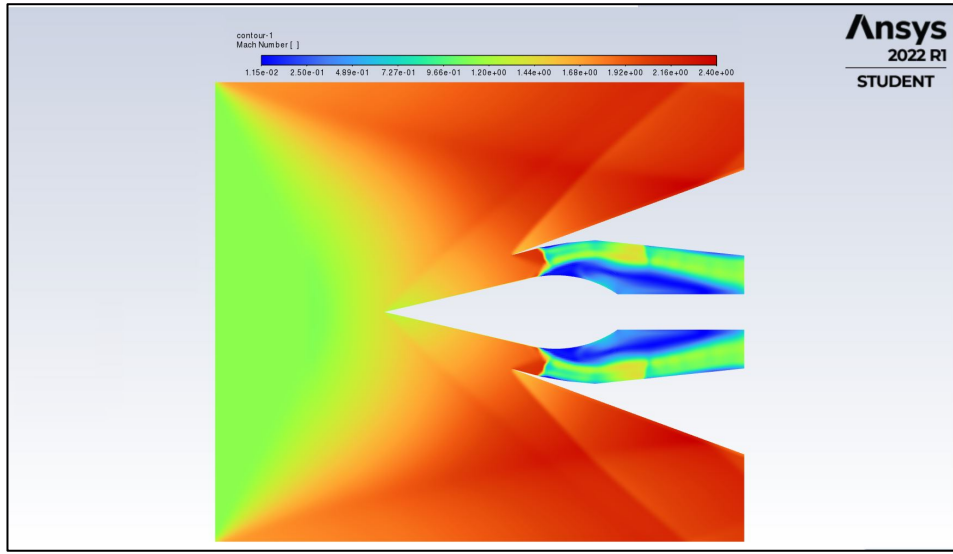


Figure 6.0.18 - Contour of Mach at sea-level

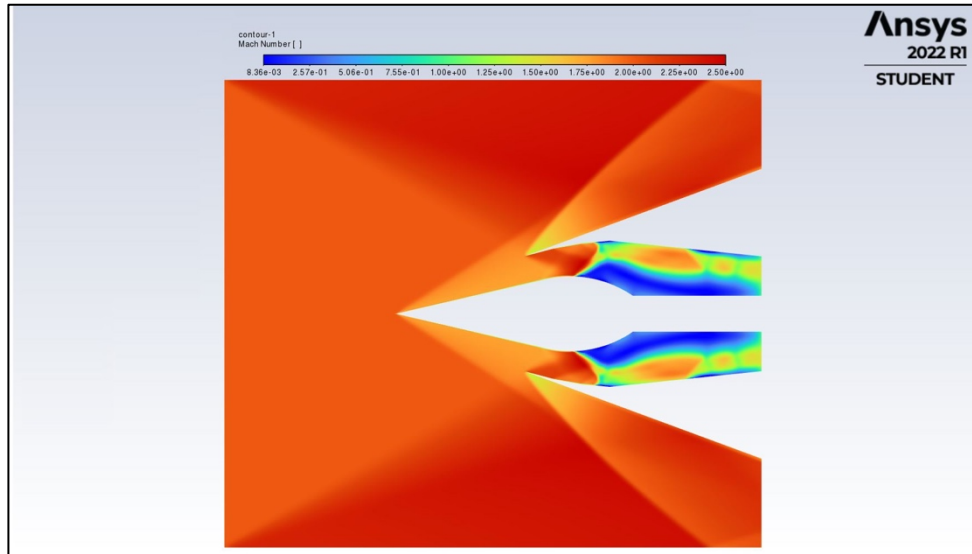


Figure 6.0.19 - Contour of Mach at design altitude

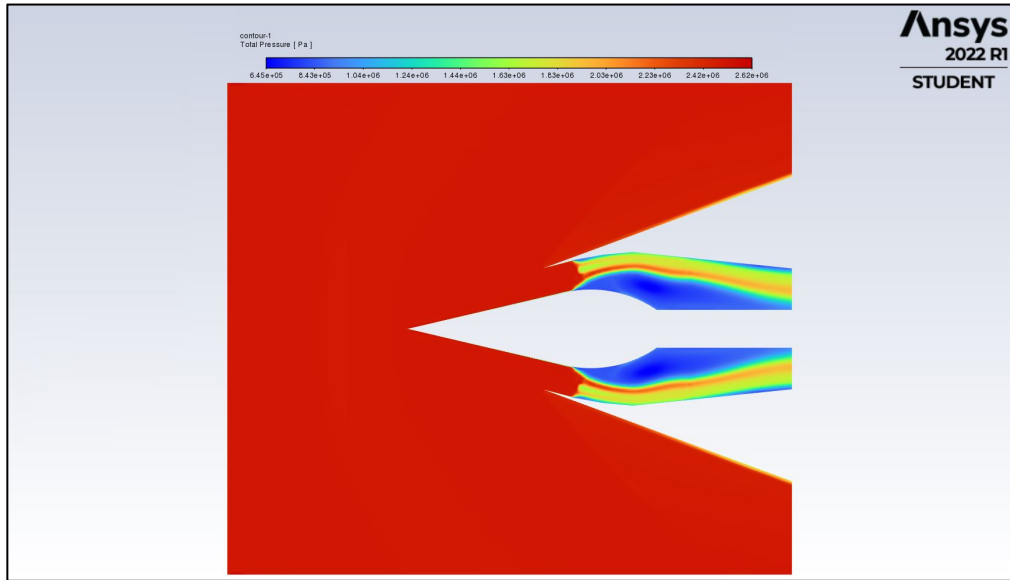


Figure 6.0.20 - Contour of total pressure at sea-level

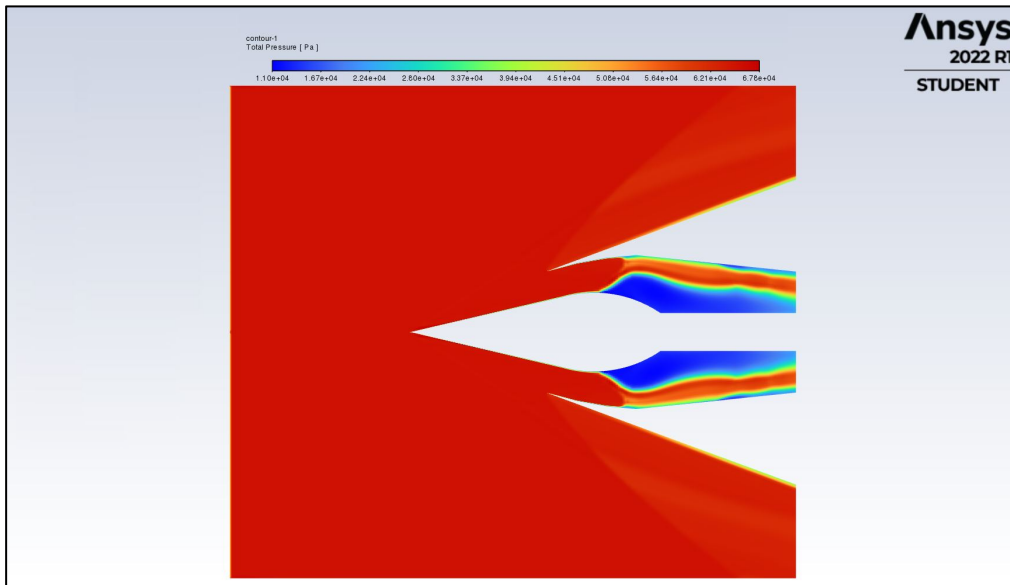


Figure 6.0.21 - Contour of total pressure at design altitude

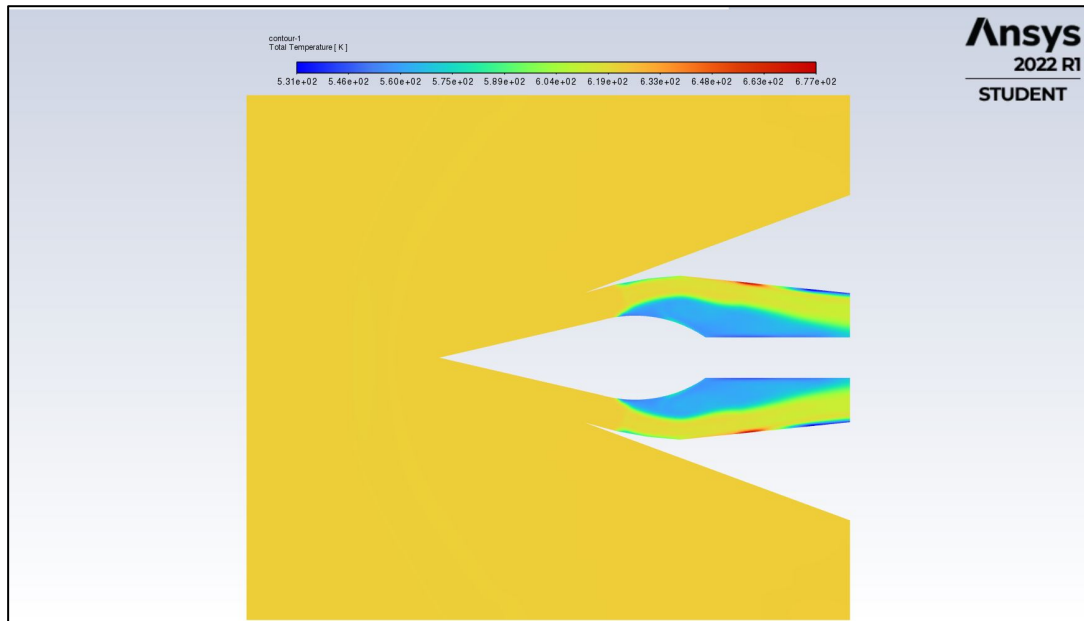


Figure 6.0.22 - Contour of total temperature at sea-level

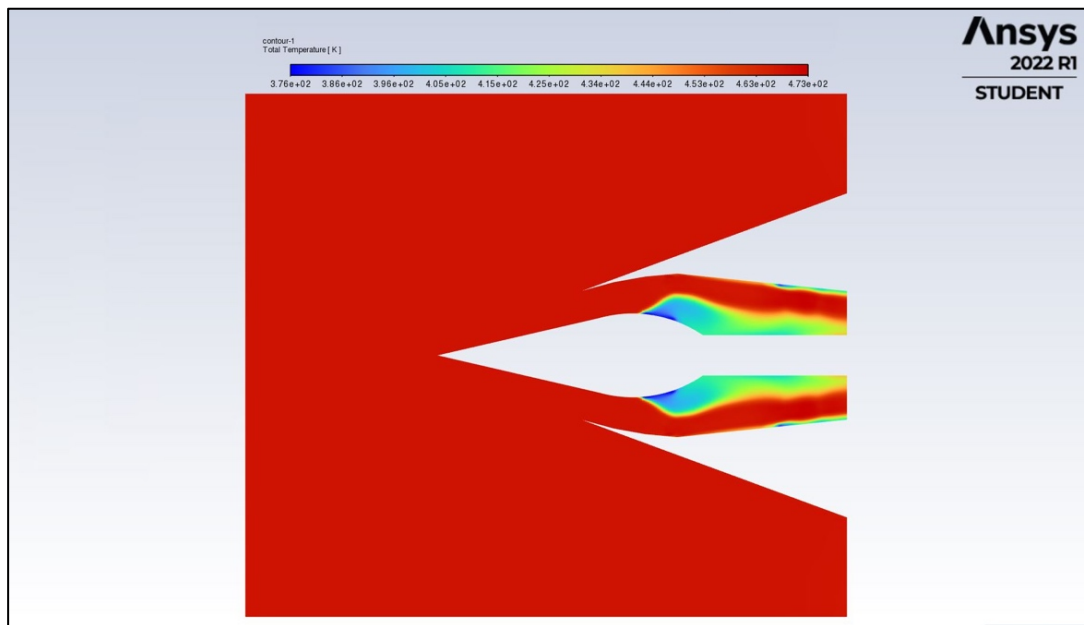


Figure 6.23 - Contour of total temperature at design altitude

Based on these results, there are few unexpected findings and successful accomplishments. For instance, there is a point at the curve where the flow is detached on the aerospike tested at sea-level conditions. The purpose of adding an aerospike was to maintain ideal expansion throughout the varying ambient pressures. However the results from the spike simulations seem to be under expanded at the desired altitude and slightly overexpanded at sea-level. This can be caused by several reasons. One could be the increased curvature of the spike design that forces the flow to make extreme turns without having enough energy to follow the curvature of the nozzle. Additionally, without a bleed near the base of the linear nozzle, the airflow's potential to maintain steady flow decreased. A bleed is a smaller nozzle ejecting some of the exhaust gases which assist the main flow to stay attached to the nozzle's profile. Therefore, in the future design adding a bleed at the base of the spike will generate better performance at varying ambient pressures.

Conversely, the flow at sea-level seems to have poor pressure recovery with inlet cones and ramps when compared to the results at design altitude. This is evident from figures 6.20 and 6.21, where the total pressure loss is nearly 40% at sea-level but only 18% at desired altitude. When the difference between initial and final total pressures are compared to their initial values, the difference is more insignificant at lower ambient pressures. This causes the boundary between initial and final pressure to be limited. Therefore, engine performance at lower altitudes are more sensitive to pressure recovery than at desired altitude. Furthermore, at full extension, the stagnation point is more forward at higher pressures than at desired altitude. Typically this is consistent with an increase in flow, pushing the oblique shocks aft of the inlet. When this occurs the shock angle decreases with respect to the inlet cone and causes the shocks to move out of the optimal location. As a result, other engine components will be exposed to inoperable temperatures and pressures causing complete engine failures. However due to the second ramp and cone's curvature, the shock was unable to sustain itself to move aft of the inlet. Additionally, the combination of both were able to slow down the velocity enough to safely enter the engine's precooler. Even though Mach at the desired altitude is higher inside the inlet than at sea-level conditions, there are no additional components which will negatively be effected with this velocity range. Besides, the precooler should reduce the velocity further before entering the combustion chamber, as some of the heat and air is absorbed to generate liquid oxidizer.

6.4 Conclusion

The results portrayed above consent to more design revisions and further testing, especially at the inlet cone with different inlet cone extensions and aerospike nozzle with base bleeds. Furthermore, the combustion chamber has not been simulated in CFD. This is due to the complexity and time constraint required to simulate fuel injection and ignition inside the combustion chamber. Regardless, the results were able to portray some performance improvement. For example, at design altitude, the linear aerospike's flow almost sustained an ideal expansion which permits constant fuel consumption and improved thrust. An addition of a small bleed, which does not add substantial amount of weight or increase fuel consumption, will increase the affinity of the flow to be more attached despite varying ambient pressures. Similarly, adjusting the intake design to produce more less curves with acute angles would assist the flow to stay attached around the inlet cone. On another note, pressure recovery at the inlet is a major influence of performance. If there is not enough pressure maintained within the engine, then the exit pressure will also be non-existent. This will reduce thrust as exit pressure is directly proportional to thrust, which can be observed in equation 6.11.

$$T = \dot{m}_e V_e + A_e(p_e - p_a) \quad (6.11)$$

In the future, further tests with varying inlet extensions will provide a more complete assessment of the effect of double ramps with an inlet cone. Plus, with an ideally expanded nozzle the thrust should be optimized at specific boundary conditions. Also by taking advantage of the available packages in CFD, the combustion chamber can be tested with the selected fuel and oxidizers. This can generate some information on the specific areas where the combustion chamber can be optimized. Based on the results, gained from these simulations further design updates can also increase the overall performance of this engine.

Chapter 7 – Delta V Budget

7.1 Introduction

Part of the mission objective is to travel from low earth orbit to the lunar orbit for a flyby and return to earth. This mission requires delta-V burns to achieve the correct trajectory. Each delta-V burn is highly correlated to the amount of propellant available, and time required to burn it. Weight of fuel determined from the previous chapters does not consider the fuel required for delta-V burns. A delta-V budget will generate an overall estimation of how many burns and how much fuel is required to accomplish this lunar mission. Since the moon is within the earth's sphere of influence, the spacecraft moving with respect to the earth and moon are governed by the three-body problem. However, through assumptions and deconstructed phases of the lunar mission, this three-body problem can be simplified and better approximated by the patched conic model. Even though the conic model's accuracy is low, for preliminary design purposes these estimated values will suffice to generate a delta-V budget. Furthermore, gravity perturbations are not considered due to the insignificant time spent in the low earth orbit (LEO) and low lunar orbit (LLO) when compared to the entire flight plan. Figure 7.1 depicts the deconstructed phases of the primary and secondary masses. In the diagram below, the primary mass is Earth, and the secondary mass is the Moon.

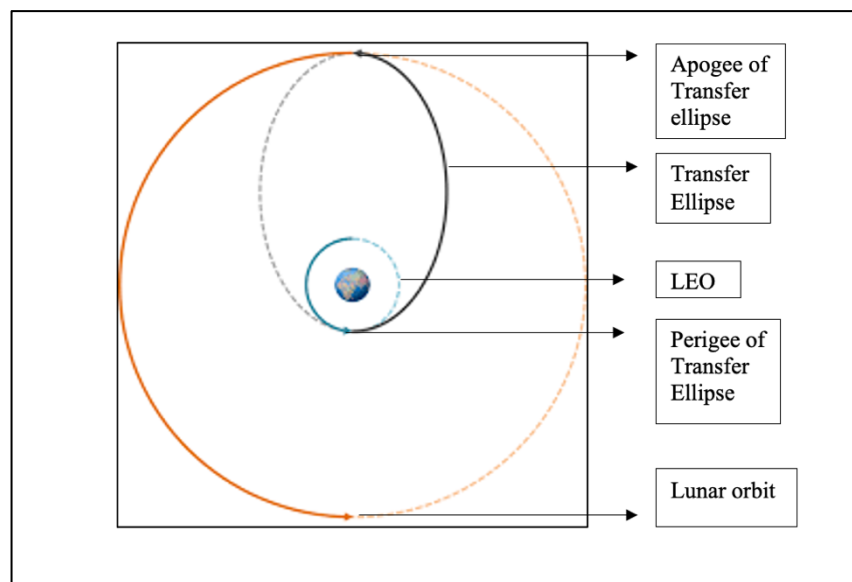


Figure 7.0.1 – Orbital trajectory for a Hohmann transfer

The trajectory displayed in this figure is an elliptical Hohmann transfer which is a gross estimation of the desired flight plan. Results from this model will generate higher discrepancies in delta-v burn calculations, leading to undesirable fuel weight estimations. Due to this reason, the patched conic model is favored over the elliptical Hohmann transfer. In the conic model, the flight plan is construed as two hyperbolic departures and one rendezvous orbit around the moon. Another undesirable attribute of a Hohmann transfer is the insertion of the spacecraft at the moon's trailing hemisphere. Such a maneuver increases the speed of the vehicle which in turn increases fuel economy to slow down the spacecraft and prevent a flyover to other planets. Therefore, a necessary inclination change will generate an intersection at the moon's leading edge after departing from earth. Similarly, the return trajectory will also include an inclination change.

Furthermore, majority of the flight plan is spent in the hyperbolic departures from the moon and earth. Since the mass of the sun alone is 333,000 and 27,000,000 times larger than the earth and moon, respectively, the sun's gravitational pull will have a higher affinity to affect the trajectory. Sun's pull will cause slight perturbations in the hypothesized trajectories. To account for these minor trajectory alterations two midcourse corrections are conducted. The basic flight plan is highlighted in figure 7.2 as a deformed figure 8 in light green color.

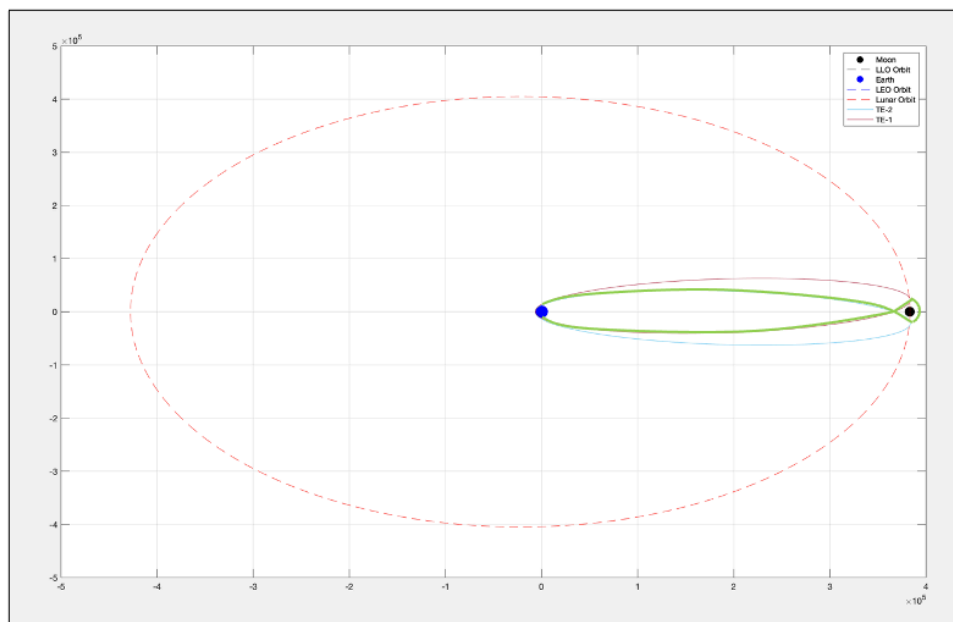


Figure 7.0.2 – Figure eight trajectory from two transfer ellipses and one circular orbit

7.2 Assumptions for Trajectory Calculations

The moon's orbit around the earth has an eccentricity of 0.0549. Since this value is close to zero, it is safe to assume that the moon's orbit is nearly circular. Similarly, LEO can also be assumed to be circular. These two assumptions setup a perfect model for a Hohmann transfer where the initial and final orbits are circular while the transfer orbit is elliptical. In the launch trajectory, the spacecraft is expected to travel from a lower energy, circular orbit to a higher energy, elliptical orbit. Therefore, this spacecraft will generate prograde burns. Once the spacecraft nears the moon, minor retrograde burns will be applied to stabilize and maintain the vehicle in the lunar orbit. At the trailing edge, another prograde burn will be conducted to insert the spacecraft into the return trajectory. The return trajectory will have the same profile as the launch trajectory. To simplify the equation further, perturbations are not considered. Additionally, the known values for this trajectory are listed in table 7.1.

Table 7.0.1 – Known values for Hohmann transfer calculations

Given	Values	Units
R_E – Radius of Earth	6378	km
LEO – Low Earth Orbit	200	km
LLO – Low Lunar Orbit	150	km
d_1 – Distance between center of earth and moon	384,400	km
r_p – Radius of perigee for transfer ellipse	6578	km
r_a – Radius of apogee for transfer ellipse	384,550	km
r_{Lp_m} - Lunar radius of perigee for return trajectory.	1,888	km
G – Gravitational constant	6.67×10^{-20}	$\text{km}^3/\text{kg} \cdot \text{s}^2$
M'_E – Mass of Earth	5.972×10^{24}	kg
M'_M – Mass of Moon	7.348×10^{22}	kg

7.3 Orbital Mechanics Calculations

In Hohmann transfer, delta-V burns are determined by the differences in velocities, as observed in equation 7.1. As the spacecraft begins to deviate from lower to higher altitude, the transfer ellipse has more energy than the energy of the circular velocity.

$$\Delta V_p = V_p - V_{circp} \quad (7.1)$$

Circular velocities at both perigee and apogee are governed by mu and their respective radii. As observed in equation 7.2, mu is a function of the gravitational constant and mass of the planet from which the circular velocity at perigee can be derived by utilizing equation 7.3.

$$\mu = GM_E \quad (7.2)$$

$$V_{circp} = \sqrt{\frac{\mu}{r_p}} \quad (7.3)$$

Based on the givens, both the circular velocities at perigee and apogee can be tabulated. However, for the transfer ellipse, the semi-major axis must be determined from equation 7.4. Once this value is known, then the elliptical velocities at perigee and apogee can be determined based on equations 7.5 and 7.6.

$$a' = \frac{1}{2}(r_a + r_p) \quad (7.4)$$

$$V_p = \sqrt{\frac{2\mu}{r_p} - \frac{\mu}{a}} \quad (7.5)$$

$$V_a = \sqrt{\frac{2\mu}{r_a} - \frac{\mu}{a}} \quad (7.6)$$

Delta-v at apogee is disclosed by equation 7.7. The elliptical orbit has lesser energy at the apogee than the circular orbit which accounts for the slight variations in equations 7.1 and 7.7, even though they are governed by the same concepts.

$$\Delta V_a = V_{circa} - V_a \quad (7.7)$$

The principles from equations 7.1 to 7.7 are also utilized in the patched conic model. This model is divided into three phases: departure, transit, and rendezvous/arrival. To calculate departure and arrival phases, the hyperbolic excess velocity derived from transit phase is required. Thus, the second phase will be calculated first before the other phases are determined. Transit phase refers to the Hohmann transfer from circular orbit of the earth to the elliptical transfer orbit. Since the conic model is a two-body problem, the sun's effect is not taken into consideration and only earth and moon are the significant masses that effect the spacecraft's trajectory. To calculate the change in velocity between the geocentric, circular orbit and the elliptical transfer orbit, equation 7.5 must be slightly altered into equation 7.8. The relation between the radii and the semi-major axis can be found in equation 7.4. Using this correlation, the major axis value can be substituted for the summation of both perigee radius and apogee radius.

$${}^E\vec{V}^Q = \sqrt{\frac{GM_E}{r_p}} \left\{ \sqrt{\frac{2r_a}{(r_p+r_a)}} - 1 \right\} = V_{\infty d1} \quad (7.8)$$

This value is also equivalent to the hyperbolic departure velocity from earth. On the other hand, the arrival velocity from hyperbolic trajectory to the moon is related to the apogee radius, as seen in equation 7.9. Nevertheless, since the circular orbit's energy of the moon is higher than the transfer ellipse's energy at apogee, the terms in the bracket are inverted.

$${}^M\vec{V}^Q = \sqrt{\frac{GM_E}{r_a}} \left\{ 1 - \sqrt{\frac{2r_p}{(r_p+r_a)}} \right\} = V_{\infty a2} \quad (7.9)$$

For return trajectory, the velocity increment required to escape low lunar orbit and transit to transfer ellipse is dictated by the arrival velocity and the difference of circular orbit energy. This specific relation is depicted in equation 7.10.

$$\Delta V = \sqrt{V_{\infty d2}^2 + \frac{GM_M}{r_{pm}}} - \sqrt{\frac{GM_M}{r_{pm}}} \quad (7.10)$$

Even though the model is geocentric, at low lunar orbit the spacecraft is in the moon's sphere of influence therefore properties such as mu, mass and perigee radius will be with respect

to the moon instead of the earth. At this phase there is also an inclination change which is incorporated to the delta-v budget. To tabulate the change in velocity due to the differences in inclination, equation 7.11 is utilized. This equation is derived from the momentum vector, which is a cross product of the position and force vectors with respect to time.

$$\Delta V = 2V_{\theta} \sin \left(\frac{\Delta i}{2} \right) \quad (7.11)$$

Due to the similarity between the proposed mission's trajectory with the Apollo 11, few of the values were extracted from published documents recording the inclinations at different stages of the mission. For instance, initially Apollo's earth orbit insertion was at an inclination of 32.521° degrees but after the second burn cutoff the inclination was reduced to 31.386° degrees [53]. The delta-v corresponding to this inclination change is reported in table 7.2 for translunar insertion (TLI). Between the ecliptic and the lunar equatorial plane there is an inclination of 1.543° degrees. Tangential velocity represented by V_{θ} is derived from the transit velocity of the spacecraft with respect to Earth as shown in equation 7.12.

$$V_{\theta} = \frac{2\pi r_p}{t} \quad (7.12)$$

Derivations of equations 7.8-7.10 from equations 7.1 to 7.7 are clearly explained in Astrodynamics Course Reader for fall of 2020 [43].

7.4 Discussion and Conclusion

After all the velocities are tabulated using the relations mentioned above, an overall budget can be determined for the entire orbital trajectory. Assuming some correctional velocities will be required during the journey, two more delta-V burns, one for departure and one for return trajectory, are added to the budget to counter act the deviations from gravitational and solar perturbations. Correctional values are extracted from the recorded documents of Apollo-11 mission [8]. The results from all the calculations, mission requirements, and final conditions are inputted into table 7.2. Since the original data was computed in International System of Units (SI), for consistency purposes the conversion to English units is also provided in column 3 of

table 7.2. Furthermore, for a better visual analysis, the results from the Apollo-11 mission are also displayed in table 7.2.

Table 7.0.2 – Total delta-v budget and conversion to English units

Item	Values	English units	Apollo-11 Data
Delta V budget (m/s)			
LEO to LLO			
1st burn - TLI	3.13 km/s	10269.03 ft/s	10008.1 ft/s
2nd burn – LOI	0.830 km/s	2723.1 ft/s	2917.5 ft/s
3rd burn – TEI	1.0394 km/s	3410.11 ft/s	3279.0 ft/s
MCC 1	0.0064372 km/s	21.12 ft/s	20.9 ft/s
MCC 2	0.0014784 km/s	4.85 ft/s	4.8 ft/s
Total delta-V without additional inclination changes	5.01 km/s	16428.20 ft/s	16230.3 ft/s
<u>Orbit Maneuvers</u>			
Inclination change from LEO to lunar orbital plane	0.483 km/s	1584.65 ft/s	--
Inclination change from lunar orbital plane to LEO	0.150 km/s	492.13 ft/s	--
Total delta-V	5.643 km/s	18504.98 ft/s	--

Assuming the spacecraft is inserted in the correct orbital plane from an earth launch, then there is no need for additional inclination changes. However, since this model does not consider any perturbations from the earth or moon, additional inclination changes are calculated for contingency purposes. Therefore, the amount of fuel carried in vacuum will be in excess for any emergency maneuvers or unexpected off-course trajectories.

Chapter 8 – Staging

8.1 Introduction

So far most of the optimized design points were extrapolated at a desired altitude within the earth's atmosphere, however the mission objective is to accomplish a lunar rendezvous and return to earth in 4 days. Such a mission requires high thrust throughout the entire journey. So, optimizing masses for each stage reduces the overall cost and increases the amount of payload space. For 10 passengers and 2 astronauts, there must be enough space for each passenger to recline into their pods, move around and to store all the required supplies for the trip. All these requirements feed into the payload budget. Typically, the staging approximation is not ideal for high thrust missions like the one proposed in this model. Regardless, results from optimal staging by utilizing Lagrange multiplier will generate the maximum amount of useful payload weight this model can have.

Even though the number of stages is limitless, the benefits of minimizing mass for each stage reduces after three stages [9]. Consequently, for this mission, only three stages will be employed to maximize the payload space. Primarily, the specific impulse, characteristic velocity, and structural ratios for three stages will be derived. Secondly, from this data the optimum mass ratios can be tabulated. Lastly, the optimized empty and propellant masses can be extrapolated. These readjusted values will be presented in a table format along with a summary of all the parameters generated thus far.

8.2 Required parameters

To calculate optimized masses, the necessary parameters can be extracted by the various specific impulses at different stages. This can be calculated by equation 8.1 and substituting delta-v burns derived from chapter 7. Even though the rocket is traveling away from earth, specific impulse is still dictated by the earth's gravitational acceleration g_0 which is equivalent to 9.81 m/s².

$$I_{sp} = \frac{V_{eq}}{g_0} \quad (8.1)$$

Characteristic velocity is a function of equivalent velocity and coefficient of thrust, as displayed in equation 8.2. The coefficient of thrust can be extracted from table 5.2.

$$c^* = \frac{V_{eq}}{C_F} \quad (8.2)$$

Structural ratio is determined by masses of different stages and equations 8.3 to 8.5 showcase these relations. Initial mass is a function of gross take-off weight and gravitational constant. On the other hand, masses for stages 2 and 3 are a function of payload mass and payload ratios.

$$m_{o_2} = \frac{m_{pl}}{\pi_2^3} \quad (8.3)$$

$$m_{o_1} = \frac{W_{gtot}}{g_o} \quad (8.4)$$

$$m_{o_3} = \frac{m_{pl}}{\pi_{pl}^3} \quad (8.5)$$

Payload ratio is determined from payload mass and mass of the overall weight, as observed in equation 8.6.

$$\pi'_{pl} = \frac{m_{pl}}{m_{o_1}} \quad (8.6)$$

Once all the masses are known, the structural ratios can be determined by the stage's empty weight and the difference of masses related to that stage, except for the last stage denoted by the subscript 1. For the final stage, only the mass of the payload remains significant therefore the difference is between the mass of the final stage and payload mass.

$$\epsilon_N = \frac{m_{E_N}}{m_{o_N} - m_{o_{N+1}}} \quad (8.7)$$

$$\epsilon_{N_1} = \frac{m_{E_{N_1}}}{m_{o_{N_1}} - m_{pl}} \quad (8.9)$$

The final parameter required for this calculation is the burnout velocity. This parameter is directly proportional to the average specific impulse, gravitational constant and inversely proportional to the product of structural and payload ratios which is then raised to the power of number of stages. Since the specific impulse and structural ratio of all three stages are not

known, the delta-v tabulated from chapter 7 will be employed as the constant velocity burnout for all three-stages.

$$V_{b_{oN}} = I_{sp} g_0 \ln \left(\frac{1}{\pi^{1/N} (1 - \varepsilon_t) + \varepsilon_t} \right)^N \quad (8.10)$$

Result from equation 8.10 can be utilized to solve for the Lagrange multiplier. Through iterative process, the multiplier can be derived from equation 8.11. Inputting the values for characteristic velocity and structural ratio from each stage with the burnout velocity will converge and produce a singular result for the multiplier.

8.3 Calculations for optimized parameters

In general equations, Lagrange multiplier is the extremum of partial derivatives with respect to x, y and z components. To find the maxima of mass ratio from the rocket equation, values for each stage's mass ratios are found from a constant point. Since the derivative of a constant is zero, the mass ratio of a specific stage will take the form of equation 8.11.

$$n_i = \frac{c_i \eta - 1}{c_i \varepsilon_i \eta} \quad (8.11)$$

Conversely, the partial derivative of the constant value with respect to the multiplier is a function of the burnout velocity, mass ratio and exhaust velocities. This relation is depicted in equation 8.12 where N represents the stage number and n is the mass ratio pertaining to that stage. Exhaust velocity is represented by c_N for that stage as well.

$$V_{b_o} = \sum_{i=1}^N c_N \ln (n_N) \quad (8.12)$$

Inputting equation 8.11 into equation 8.12 and expanding it by adhering to the logarithmic rules, the new form is depicted in equation 8.13.

$$\sum_{i=1}^N c_i \ln(c_i \eta - 1) - \ln \eta \sum_{i=1}^N c_i - \sum_{i=1}^N c_i \ln c_i \varepsilon_i = V_{b_o} \quad (8.13)$$

All these values were inputted into MATLAB and solved iteratively for the Lagrange multiplier which is substituted back into equation 8.11 to generate the optimized mass ratios. Once the new mass ratios are tabulated, equation 8.14 to 8.16 are utilized to derive the optimum masses for each stage.

$$m_3 = \frac{n_3-1}{1-n_3\varepsilon_3} (m_{pl}) \quad (8.14)$$

$$m_2 = \frac{n_2-1}{1-n_2\varepsilon_2} (m_{pl} + m_3) \quad (8.15)$$

$$m_1 = \frac{n_1-1}{1-n_1\varepsilon_1} (m_{pl} + m_2 + m_3) \quad (8.16)$$

Now that the overall mass for each stage is determined, empty and propellant weights required for specific stages are showcased in equations 8.17 and 8.18, respectively.

$$m_{E_N} = \varepsilon_N m_N \quad (8.17)$$

$$m_{P_N} = m_N - m_{E_N} \quad (8.18)$$

Results from equations 8.14 to 8.16 can also be employed to calculate the optimized overall mass which is dictated in equation 8.19.

$$m_o = m_1 + m_2 + m_3 \quad (8.19)$$

Like the masses for each stage, optimum payload ratios are dependent on the weight relevant for that stage. For instance, in a three-stage rocket, the third stage mainly consists of the payload while the second stage must support both masses: third stage, and its own. This method continues until the last stage where all the preceding masses are summed and divided by the mass of that stage.

Formulas displayed in equations 8.20 to 8.22 reveal the payload ratio of each stage for this type of rocket.

$$\lambda_3 = \frac{m_{pl}}{m_3} \quad (8.20)$$

$$\lambda_2 = \frac{m_{pl}+m_3}{m_2} \quad (8.21)$$

$$\lambda_1 = \frac{m_{pl}+m_2+m_3}{m_1} \quad (8.22)$$

8.4 Discussion and Conclusion

From these newly optimized masses, the previous weights can be used for comparison to observe the amount of discrepancy between them. All the results are showcased in table 8.1.

Table 8.0.1 – All the required and calculated values for optimum masses

Term	Value
<i>Required Parameters</i>	
m_{E_1}	5.4935E4 kg
m_{E_2}	4.9442E4 kg
m_{E_3}	4.4947E4 kg
<i>Initial Mass and Payload Ratio</i>	
m_{o_1}	7.0805E5 kg
m_{o_2}	3.6409E5 kg
m_{o_3}	1.8722E5 kg
π_{pl}	0.1360
<i>Specific Impulse</i>	
I_{sp_1}	450 secs
I_{sp_2}	400 secs
I_{sp_3}	375 secs
<i>Exhaust Velocity</i>	

Term	Value
c_1	3.13 km/s
c_2	0.829 km/s
c_3	1.098 km/s
<i>Structural Ratio</i>	
ε_1	0.1597
ε_2	0.2795
ε_3	0.4942
Optimized Values	
η	2.0463
<i>Mass Ratio</i>	
n_1	5.284
n_2	1.468
n_3	1.123
<i>Mass of Each Stage</i>	
m_3	26580.101 kg
m_2	97635.640 kg
m_1	6049244.389 kg
<i>Stage's Empty Mass</i>	
m_{e_1}	966153.504 kg
m_{e_2}	27292.725 kg
m_{e_3}	13135.707 kg
<i>Propellant Required for Each Stage</i>	
m_{p_1}	5083090.885 kg
m_{p_2}	70342.916 kg
m_{p_3}	13444.394 kg
<i>Payload Ratio</i>	
λ_1	0.036
λ_2	1.258

Term	Value
λ_3	3.622
Total Values	
m_{o_t}	6269734.881 kg
$\pi'_{p_l_t}$	0.0154

Even though, the mass for the third stage is smaller than the initial payload this is the minimum mass required to carry the payload throughout the mission. Furthermore, only the gross empty weight of the rocket was known so one-tenth of this value was hypothesized for each stage. This fraction was the lowest value in MATLAB that generated a positive Lagrange multiplier. To further validate the results from these equations, a check was conducted using equation 8.23 for all three stages.

$$c = \eta c_N (\varepsilon_N n_N - 1)^2 + 2 \varepsilon_N n_N - 1 \quad (8.23)$$

The three values were positive which corroborated that the masses extrapolated for all stages were the local minimum values. The final weight of the rocket is 12,265,600 lbs more than the overall gross take-off weight calculated in chapter 3. This increase is expected since the values calculated in chapter 5 did not include the fuel required in space and the design was considered as one coherent vehicle, instead of a staged vehicle. Additionally, the payload space is maximized for the required constraints needed for lunar travel.

References

- [1] Jones, H., “The Recent Large Reduction in Space Launch,” *International Conference on Environmental Systems*, 2018, pp.8-12.
- [2] Cohen, E., and Spector, S., “Comparative visions of cosmic expansion: implications for sustainability,” *Journal of Sustainable Tourism*, DOI: [10.1080/09669582.2020.1777142](https://doi.org/10.1080/09669582.2020.1777142)
- [3] Varvill, R., and Bond, A., “THE SKYLON SPACEPLANE: PROGRESS TO REALISATION,” *Journal of the British Interplanetary Society*, Vol. 61, 2008, pp.412-418, DOI: [10.1.1.685.5755&rep=rep1&type=pdf](https://doi.org/10.1.1.685.5755&rep=rep1&type=pdf)
- [4] Karampelas, A., Tsigaridi, L., Prodromidi, E., Kerkines, I.S.K., Poulou, V., and Arsenikos, S., “A School Experiment Inside Blue Origin’s New Shepard Space Vehicle Under Microgravity Conditions,” *Creating Conditions for Deeper Learning in Science*, 2019, pp.83
- [5] Sethi, C., “The Return of Manned Missions,” *The American Society of Mechanical Engineers*, 2019, Vol. 141, No.7, pp. 48-53, DOI: [10.1115/1.2019-JUL3](https://doi.org/10.1115/1.2019-JUL3)
- [6] Buck, D., “CST-100 STARLINER: Boeing’s Commercial Crew Program,” *The Space Congress® Proceedings*, 2016
- [7] Rösigen, T., Tribot, J., and Mareschi, V., “Flight Data Analysis of the Multicolor Imaging Pyrometry Experiment on ESA’s Intermediate Experimental Vehicle (IXV),” *International Conference on Flight Vehicles, Aerothermodynamics and Re-entry Missions and Engineering*, 2019, DOI: [20.500.11850/368235](https://doi.org/20.500.11850/368235)
- [8] Zaccagnino, E., Malucchi, G., Marco, V., Drocco, A., Dussy, S., and Préaud, J.-P., “Intermediate eXperimental vehicle (IXV), the ESA re-entry demonstrator,” *AIAA Guidance, Navigation, and Control Conference*, 2011, pp. 6340, DOI:

- [9] Yonemoto, K., Fujikawa, T., Morito, T., Wang, J., and Choudhuri, A., “Subscale Winged Rocket Development and Application to Future Reusable Space Transportation,” *ResearchGate*, Vol. 10, No. 1, 2018, pp. 161-172, DOI: [10.13111/2066-8201.2018.10.1.15](https://doi.org/10.13111/2066-8201.2018.10.1.15)
- [10] Sivan, K., and Pandian, S., “An Overview of Reusable Launch Vehicle Technology Demonstrator” *Current Science*, Vol. 114, 2018, DOI: [10.18520/cs/v114/i01/38-47](https://doi.org/10.18520/cs/v114/i01/38-47)
- [11] Chang, Y.-W., and Chern, J.-S., “Ups and downs of space tourism development in 60 years from moon register to spaceshiptwo CRASH,” *Acta Astronautica*, Vol. 127, 2016, pp. 533-541, DOI: [10.1016/j.actaastro.2016.06.008](https://doi.org/10.1016/j.actaastro.2016.06.008)
- [12] Dong, Z., Sun, M., Wang, Z., Chen, J., and Cai, Z., “Survey on key techniques of rocket-based combined-cycle engine in ejector mode,” *Acta Astronautica*, Vol. 164, 2019, pp. 51-68, DOI: [10.1016/j.actaastro.2019.07.016](https://doi.org/10.1016/j.actaastro.2019.07.016)
- [13] Klink, P., and Ogawa, H., “Investigation on the performance and feasibility of RBCC-based access-to-space via multi-objective design optimization,” *Acta Astronautica*, Vol. 157, 2019, pp. 435-454, DOI: [10.1016/j.actaastro.2018.12.034](https://doi.org/10.1016/j.actaastro.2018.12.034)
- [14] Zhang, T., Wang, Z., Huang, W., Ingham, D., Ma, L., and Porkashanian, M., “An analysis tool of the rocket-based combined cycle engine and its application in the two-stage-to-orbit mission,” *Energy*, Vol. 193, 2020, pp. 116709, DOI: [10.1016/j.actaastro.2019.116709](https://doi.org/10.1016/j.actaastro.2019.116709)
- [15] Aggarwal, R., Lakhara, K., Sharma, P.B., Darang, T., Jain, N., and Gangly, S., “SABRE Engine: Single Stage to Orbit Rocket Engine,” *International Journal Innovative Research in Science, Engineering and Technology*, Vol. 4, No. 10, 2015, pp. 10360-10366, DOI: [10.15680/IJRSET.2015.0410107](https://doi.org/10.15680/IJRSET.2015.0410107)

- [16] “Reaction Engines test programme fully validates precooler at hypersonic heat conditions,”
UK Space, 2019
- [17] Davies, P., Hempzell, M., and Varvill, R., “PROGRESS ON SKYLON AND SABRE,”
Proceedings of the International Astronautical Congress, Vol. 11, 2013, pp. 8427-8440.
- [18] Mukunda, V.S., Jain, V.K., Paul, P.J., “A review of hybrid rockets: present status and future potential,” *Proceedings of the Indian Academy of Sciences*, Vol. 2, 1979, pp. 215-242, DOI: [10.1007/BF02845033](https://doi.org/10.1007/BF02845033)
- [19] Frota, O., and Ford, M., “REVIEW ON HYBRID PROPELLANTS,” *ESA Special Publication*, Vol. 557, 2004, pp. 7-8, DOI: [2004ESASP.557E..33F](https://doi.org/2004ESASP.557E..33F)
- [20] Sutton, G., and Biblarz, O., “HYBRID PROPELLANTS ROCKET PROPULSION,” *Rocket Propulsion Elements*, 9th ed., Wiley, New Jersey, 2016, pp. 593-616.
- [21] Kuo, K., and Chiaverini, M., “Analytical Models for Hybrid Rockets,” *Fundamentals of Hybrid Rocket Combustion and Propulsion*, Vol. 218, American Institute of Aeronautics and Astronautics, Virginia, 2007, pp. 207-246, DOI: [10.2514/4.866876](https://doi.org/10.2514/4.866876)
- [22] Venugopal, S., Rajesh, K.K., and Ramanujachari, V., “Hybrid Rocket Technology,”
Defense Science Journal, Vol. 61, 2011, pp. 193-200, DOI: [10.14429/dsj.61.518](https://doi.org/10.14429/dsj.61.518)
- [23] Pastrone, D., “Approaches to Low Fuel Regression Rate in Hybrid Rocket Engines,”
International Journal of Aerospace Engineering, Vol. 2012, 2012, pp.1-12,
DOI: [10.1155/2012/649753](https://doi.org/10.1155/2012/649753)
- [24] Altman, D., “Hybrid rocket development history,” 27th Joint Propulsion Conference, 1991,
pp. 2515, DOI: [10.2514/6.1991-2515](https://doi.org/10.2514/6.1991-2515)

- [25] Calabro, M., “Overview on hybrid propulsion,” *Progress in Propulsion Physics*, Vol. 2, 2011, pp. 353-374, DOI: [10.1051/eucass/201102353](https://doi.org/10.1051/eucass/201102353)
- [26] Ley, W., Wittmann, K., and Hallmann, W., “Propulsion Systems”, *Handbook of Space Technology*, Wiley, Singapore, 2009, pp. 154-183.
- [27] Harnett, E., “Chemical and Plasma Rocket Propulsion,” *Lecture 24 Electric Propulsion V2*, University of Washington, 2012
- [28] Arbit, H., Clapp, S., and Nagai, C., “Investigation of the Lithium-Fluorine-Hydrogen Tripropellant System,” *American Institute of Aeronautics and Astronautics*, Vol. 7, 1970, pp. 1221, DOI: [/10.2514/3.30138](https://doi.org/10.2514/3.30138)
- [29] Mattingly, J., “The SNECMA ATAR 9C,” *Aircraft Engine Historical Society*
- [30] Grosdemange, H., and Schaefer, G., “The SEPR 844 Reusable Liquid Rocket Engine For Mirage Combat Aircraft,” *26th Joint Propulsion Conference*, 1990, pp. 1835, DOI: <https://doi.org/10.2514/6.1990-1835>
- [31] Wilkinson, P., “Aircraft Engines of the World, 1956,” *The Aeronautical Journal*, Vol. 60, No. 541, 1956, pp. 75, DOI: <https://doi.org/10.1017/S0368393100132559>
- [32] Krebs, G., “SpaceShipOne History,” *Gunter’s Space Page*
- [33] Rothmund, C., “Reusable Man-Rated Rocket Engines: The French Experience, 1944-1996,” *55th International Astronautical Congress of the International Astronautical Federation, the International Academy of Astronautics, and the International Institute of Space Law*, 2004, pp. IAA-6, DOI: <https://doi.org/10.2514/6.IAC-04-IAA.6.15.3.02>
- [34] Graham, R., “Flight Characteristics,” *SR-71 Flight Manual: The Official Pilot’s Handbook Declassified and Expanded with Commentary*, 1st ed., Voyageur Press, Minnesota, 2016,

pp 6-1.

- [35] Hendrickson, C., Smith, R., “NF-104A Aerospace Trainer Evaluation,” *Air Force Test Center Edwards AFB*, 1965, pp. 26
- [36] Swopes, B., “General Electric J79-GE-3B,” *This Day in Aviation: Important Dates in Aviation History*, 2018, retrieved 30 Jan 2021.
- [37] Hill, P., and Peterson, C., “Turbomachinery for Liquid-Propellant Rockets,” *Mechanics and Thermodynamics of Propulsion*, 2nd ed., Pearson, London, 1991, pp. 413-414.
- [38] Loosbrock, J., Avery, N., Butz, J.S., Witze, C., Carey, W.D., Stiles, L.J., Leavitt, W., Jonas, A.M., and De Sandro, J., “Air Force and Space Digest – The Magazine of Aerospace Power,” *Air Force Association*, Vol. 49, No. 2, 1966, pp. 50-51.
- [39] Alekhya, N., Kishore, P., Gupta, S. and Mukkoti, V., “COMPARISON OF PERFORMANCE OF CONIC AND RAMP INLET USING CFD,” *International Journal of Mechanical Engineering and Technology (IJMET)*, Vol. 8, No. 7, 2017, pp. 190-198
- [40] Fulop, L., Henry, I., Ruffner, J., and McMullen, A., “Supersonic Propulsion: Inlet Shock Wave/Boundary Layer Interaction in a Diffuser,” *Williams Honors College, Honors Research Project*, 2020, pp. 1161
- [41] Newton, I., “Axioms or laws of motion,” *The Principia: The Authoritative Translation Mathematical Principles of Natural Philosophy*, University of California Press, Berkeley, 2016, pp. 62-76, DOI: <https://doi.org/10.1525/9780520964785-010>
- [42] Anderson, J., “Navier-Stokes Solutions: Some Examples,” *Fundamentals of Aerodynamics*, 6th ed., McGraw Hill Education, New York, 2017, pp. 1063-1078

- [43] Hunter, J., “Interplanetary Trajectories,” *Orbital Mechanics & Mission Design: Fall 2020*, San Jose State University, California, 2020, pp. 90-93.
- [44] Nazarinia, M., Naghib-Lahouti, A., and Tolouei, E., “Design and Numerical Analysis of Aerospoke Nozzle with Different Plug Shapes to Compare their Performance with a Conventional Nozzle,” *AIAC-11 Eleventh Australian International Aerospace Congress*, 2005
- [45] Nagano, Y., Tagawa, M., “An Improved k- ϵ Model for Boundary Layer Flows,” *The American Society of Mechanical Engineers*, Vol. 112, 1990, pp. 33-39
- [46] Glatt, C., “Body Structure,” WAATS – A Computer Program for Weights Analysis of Advanced Transportation Systems, Aerophysics Research Corporation, Virginia, pp. 41.
- [47] Newlands, R., “The Thrust Optimised Parabolic nozzle,” *Aspire Space Rocket Engineering Society*, retrieved 10 April 2022.
- [48] Sreenath, K., Mubarak, A., “Design and analysis of contour bell nozzle and comparison with dual bell nozzle,” *International Journal of Research and Engineering*, Vol. 3, No. 6, 2016, pp. 52-56
- [49] Dakka, S., & Dennison, O., “Numerical Analysis of Aerospoke Engine Nozzle Performance at Various Truncation Lengths,” *International Journal of Aviation, Aeronautics, and Aerospace*, Vol. 8, No. 2, 2021, pp. 1-23, DOI: <https://doi.org/10.15394/ijaaa.2021.1601>
- [50] Anderson, J., “Oblique Shock and Expansion Waves,” *Fundamentals of Aerodynamics*, 6th ed., McGraw Hill Education, New York, 2017, pp. 625
- [51] Anderson, J., “Appendix B Normal Shock Properties,” *Fundamentals of Aerodynamics*, 6th ed., McGraw Hill Education, New York, 2017, pp. 1085

- [52] Kerrebrock, J., “Ramjets,” *Aircraft Engines and Gas Turbines*, 2nd ed., MIT Press, Massachusetts, 1992, pp. 6
- [53] Orloff, R., “Apollo by the Numbers,” National Aeronautics and Space Administration, 1966, pp. 22, DOI:
- [54] Anderson, J., “How Supersonic Inlets Work: Details of the Geometry and Operation of the SR-71 Mixed Compression Inlet,” Lockheed Martin Skunk Works, San Diego, CA, May 2014. URL: <http://www.enginehistory.org/Convention/2014/SR-71Inlts/SR-71Inlts.shtml>
- [55] Sutton, G., and Biblarz, O., “Definitions and Fundamentals,” *Rocket Propulsion Elements*, 9th ed., Wiley, New Jersey, 2016, pp. 30.
- [56] “Out of this World,” Embry-Riddle Aeronautical University, 2022.

Appendix A - HASA weight calculations

Fuel Weight:

$$W_{propellant} = W_{fuel} + W_{oxidizer}$$

$$W_{fuel} = m_{fuel}(W_{gtot})$$

$$W_{oxidizer} = m_{oxidizer}(W_{gtot})$$

Structural Weight:

$$W_{str} = W_b + W_w + W_{vt} + W_{ht} + W_{tps} + W_{gear} + W_{thrust}$$

Body Weight:

$$W_b = 0.341 mf(\sigma)$$

$$\sigma = \left| \left(\frac{L_b ULF}{D_{bc}} \right)^{0.15} (Q_{max})^{0.16} (S_{tot})^{1.05} \right|$$

Empty Weight:

$$W_{emp} = W_{gtot} - W_{fuel}$$

Wing Weight:

$$W_w = 0.2958 mf \left\{ \left| \frac{W_{emp} ULF}{1000} \right|^{0.52} |S_{ref}|^{0.7} |AR|^{0.47} \left| \frac{1+\lambda}{\frac{t}{c}} \right|^{0.4} \left| 3 + \frac{7}{\cos\left(\frac{\lambda_1}{2}\right)} \right| \right\}^{1.017}$$

Tail Weight:

$$W_{ht} = 0.0035 (\Lambda)$$

$$\Lambda = \left| \left(\frac{W_{gtot}}{S_{ref}} \right)^{0.6} (S_{wfh})^{1.2} (Q_{max})^{0.8} \right|$$

Vertical Tail:

$$W_{vt} = 5.0(S_{wfv})^{1.09}$$

Thermal Protection System Weight:

$$W_{tps} = W_{ins}(S_{tb} + S_{ref} + S_{wfh})$$

Landing Gear Weight:

$$W_{gear} = 0.00916 (W_{gtot})^{1.124}$$

Thrust Structure:

$$W_{thra} = 0.00625(T_{tott}) + 69.0$$

$$W_{thrr} = 0.0025(T_{totrk})$$

Engine: Turboramjet and Rocket

$$W_{trj} = N_{engtr}1782.63 e 0.003(W_a)$$

$$W_{trk} = 0.00766(T_{totrk}) + 0.00033(T_{totrk})(A_{ratio})^{0.5} + 130(N_{engrt})$$

Tank:

$$W_{tnk} = \sum \rho_{tank} V_{fuel} + fuel\ tank\ insulation$$

Propulsion:

$$W_{prop} = W_{tnk} + W_{eng}$$

Subsystems:

$$W_{sub} = W_{hyd} + W_{avcs} + W_{elec} + W_{equip}$$

Hydraulics:

$$W_{hyd} = 2.64(\psi)$$

$$\psi = \left| \left(\frac{(S_{ref} + S_{wfv} + S_{wfh})Q_{max}}{1000} \right)^{0.334} (L_b + W_{span})^{0.5} \right|$$

Avionics:

$$W_{avcs} = 66.37(W_{gtot})^{0.361}$$

Electronics:

$$W_{elec} = 1.167(O)^{0.361}$$

$$O = \left| (W_{gtot})^{0.5} (L_b)^{0.25} \right|^{1.0}$$

Equipment:

$$W_{equip} = 10000 + 0.01(W_{gtot} + 0.0000003)^1$$

Payload Weight:

$$W_{pay} = 3.3 * (V_{pay})$$

Appendix B – MATLAB code for design point

```
clc
close all
clear all;

dataset = xlsread('data.xlsx','A2:BH27');

x1 = dataset(:,1);
y1 = dataset(:,2);
z1 = dataset(:,3);
a = dataset(:,4);
b = dataset(:,5);
c = dataset(:,6);
d = dataset(:,7);
e = dataset(:,8);
f = dataset(:,9);
g = dataset(:,10);
h = dataset(:,11);
i = dataset(:,12);
j = dataset(:,13);
k = dataset(:,14);
l = dataset(:,15);
m = dataset(:,16);
n = dataset(:,17);
o = dataset(:,18);
p = dataset(:,19);
q = dataset(:,20);
r = dataset(:,21);
s = dataset(:,22);
t = dataset(:,23);
u = dataset(:,24);
v = dataset(:,25);
w = dataset(:,26);
x = dataset(:,27);
y = dataset(:,28);
z = dataset(:,29);
aa = dataset(:,30);
ab = dataset(:,31);
ac = dataset(:,32);
ad = dataset(:,33);
ae = dataset(:,34);
af = dataset(:,35);
ag = dataset(:,36);
ah = dataset(:,37);
ai = dataset(:,38);
aj = dataset(:,39);
ak = dataset(:,40);
al = dataset(:,41);
am = dataset(:,42);

%% Second Set of Data

dat = xlsread('datsht.xlsx','A2:BZ27');

bf = dat(:,1);
bg = dat(:,2);
```

```
bh = dat(:,3);
bi = dat(:,4);
bj = dat(:,5);
bk = dat(:,6);
bl = dat(:,7);
bm = dat(:,8);
bn = dat(:,9);
bo = dat(:,10);
bp = dat(:,11);
bq = dat(:,12);
br = dat(:,13);
bs = dat(:,14);
bt = dat(:,15);
bu = dat(:,16);
bv = dat(:,17);
bw = dat(:,18);
bx = dat(:,19);
by = dat(:,20);
bz = dat(:,21);
ca = dat(:,22);
cb = dat(:,23);
cc = dat(:,24);
cd = dat(:,25);
ce = dat(:,26);
cf = dat(:,27);
cg = dat(:,28);
ch = dat(:,29);
ci = dat(:,30);
cj = dat(:,31);
ck = dat(:,32);
cl = dat(:,33);
cm = dat(:,34);
cn = dat(:,35);
co = dat(:,36);
cp = dat(:,37);
cq = dat(:,38);
cr = dat(:,39);
cs = dat(:,40);
ct = dat(:,41);
cu = dat(:,42);
cv = dat(:,43);
cw = dat(:,44);
cx = dat(:,45);
cy = dat(:,46);
cz = dat(:,47);
da = dat(:,48);
db = dat(:,49);
dc = dat(:,50);
dd = dat(:,51);
de = dat(:,52);
df = dat(:,53);
dg = dat(:,54);
dh = dat(:,55);
di = dat(:,56);
dj = dat(:,57);
dk = dat(:,58);
dl = dat(:,59);
dm = dat(:,60);
```

```

dn = dat(:,61);
do = dat(:,62);
dp = dat(:,63);
dq = dat(:,64);
dr = dat(:,65);
ds = dat(:,66);
dt = dat(:,67);
du = dat(:,68);
dv = dat(:,69);
dw = dat(:,70);
dx = dat(:,71);
dy = dat(:,72);

figure(1)
scatter3(x1,y1,z1, 'MarkerFaceColor', [1 .6 .6])
hold on
scatter3(a,b,c, 'MarkerFaceColor', [1 .6 .6])
hold on
scatter3(d,e,f, 'MarkerFaceColor', [1 .6 .6])
hold on
scatter3(g,h,i, 'MarkerFaceColor', [1 .6 .6])
hold on
scatter3(j,k,l, 'MarkerFaceColor', [1 .6 .6])
hold on
scatter3(m,n,o, 'MarkerFaceColor', [1 .6 .6])
hold on
scatter3(p,q,r, 'MarkerFaceColor', [1 .6 .6])
hold on
scatter3(s,t,u, 'MarkerFaceColor', [1 .6 .6])
hold on
scatter3(v,w,x, 'MarkerFaceColor', [1 .6 .6])
hold on
scatter3(y,z,aa, 'MarkerFaceColor', [1 .6 .6])
hold on
scatter3(ab,ac,ad, 'MarkerFaceColor', [1 .6 .6])
hold on
scatter3(ae,af,ag, 'MarkerFaceColor', [1 .6 .6])
hold on
scatter3(ah,ai,aj, 'MarkerFaceColor', [1 .6 .6])
hold on
scatter3(ak,al,am, 'MarkerFaceColor', [1 .6 .6])
hold on
scatter3(bf,bg,bh, 'MarkerFaceColor', [0 .75 .75])
hold on
scatter3(bi,bj,bk, 'MarkerFaceColor', [0 .75 .75])
hold on
scatter3(bl,bm,bn, 'MarkerFaceColor', [0 .75 .75])
hold on
scatter3(bo,bp,bq, 'MarkerFaceColor', [0 .75 .75])
hold on
scatter3(br,bs,bt, 'MarkerFaceColor', [0 .75 .75])
hold on
scatter3(bu,bv,bw, 'MarkerFaceColor', [0 .75 .75])
hold on
scatter3(bx,by,bz, 'MarkerFaceColor', [0 .75 .75])
hold on
scatter3(ca,cb,cc, 'MarkerFaceColor', [0 .75 .75])
hold on

```

```

scatter3(cd,ce,cf, 'MarkerFaceColor',[0 .75 .75])
hold on
scatter3(cg,ch,ci, 'MarkerFaceColor',[0 .75 .75])
hold on
scatter3(cj,ck,cl, 'MarkerFaceColor',[0 .75 .75])
hold on
scatter3(cm,cn,co, 'MarkerFaceColor',[0 .75 .75])
hold on
scatter3(cp,cq,cr, 'MarkerFaceColor',[0 .75 .75])
hold on
scatter3(cs,ct,cu, 'MarkerFaceColor',[0 .75 .75])
hold on
scatter3(cv,cw,cx, 'MarkerFaceColor',[0 .75 .75])
hold on
scatter3(cy,cz,da, 'MarkerFaceColor',[0 .75 .75])
hold on
scatter3(da,db,dc, 'MarkerFaceColor',[0 .75 .75])
hold on
scatter3(de,df,dg, 'MarkerFaceColor',[0 .75 .75])
hold on
scatter3(dh,di,dj, 'MarkerFaceColor',[0 .75 .75])
hold on
scatter3(dk,dl,dm, 'MarkerFaceColor',[0 .75 .75])
hold on
scatter3(dn,do,dp, 'MarkerFaceColor',[0 .75 .75])
hold on
scatter3(dq,dr,ds, 'MarkerFaceColor',[0 .75 .75])
hold on
scatter3(dt,du,dv, 'MarkerFaceColor',[0 .75 .75])
hold on
scatter3(dw,dx,dy, 'MarkerFaceColor',[0 .75 .75])

xlabel('Specific Thrust')
ylabel('Specific Fuel Consumption')
zlabel('Overall Efficiency')
title('Ramjet Analysis')

```

```
%% Scramjet MDO Analysis
```

```
set = xlsread('ScramMach.xlsx','A2:AS27');
```

```

ea = set(:,1);
eb = set(:,2);
ec = set(:,3);
ed = set(:,4);
ee = set(:,5);
ef = set(:,6);
eg = set(:,7);
eh = set(:,8);
ei = set(:,9);
ej = set(:,10);
ek = set(:,11);
el = set(:,12);
em = set(:,13);
en = set(:,14);
eo = set(:,15);
ep = set(:,16);

```

```

eq = set(:,17);
er = set(:,18);
es = set(:,19);
et = set(:,20);
eu = set(:,21);
ev = set(:,22);
ew = set(:,23);
ex = set(:,24);
ey = set(:,25);
ez = set(:,26);
fa = set(:,27);
fb = set(:,28);
fc = set(:,29);
fd = set(:,30);
fe = set(:,31);
ff = set(:,32);
fg = set(:,33);
fh = set(:,34);
fi = set(:,35);
fj = set(:,36);
fk = set(:,37);
fl = set(:,38);
fm = set(:,39);
fn = set(:,40);
fo = set(:,41);
fp = set(:,42);
fq = set(:,43);
fr = set(:,44);
fs = set(:,45);

combu = xlsread('Scramtaub.xlsx','A2:BZ27');

ft = combu(:,1);
fu = combu(:,2);
fv = combu(:,3);
fw = combu(:,4);
fx = combu(:,5);
fy = combu(:,6);
fz = combu(:,7);
ga = combu(:,8);
gb = combu(:,9);
gc = combu(:,10);
gd = combu(:,11);
ge = combu(:,12);
gf = combu(:,13);
gh = combu(:,14);
gi = combu(:,15);
gj = combu(:,16);
gk = combu(:,17);
gl = combu(:,18);
gm = combu(:,19);
gn = combu(:,20);
go = combu(:,21);
gp = combu(:,22);
gq = combu(:,23);
gr = combu(:,24);
gs = combu(:,25);
gt = combu(:,26);

```

```

gu = combu(:,27);
gv = combu(:,28);
gw = combu(:,29);
gx = combu(:,30);
gy = combu(:,31);
gz = combu(:,32);
ha = combu(:,33);
hb = combu(:,34);
hc = combu(:,35);
hd = combu(:,36);
he = combu(:,37);
hf = combu(:,38);
hg = combu(:,39);
hh = combu(:,40);
hi = combu(:,41);
hj = combu(:,42);
hk = combu(:,43);
hl = combu(:,44);
hm = combu(:,45);
hn = combu(:,46);
ho = combu(:,47);
hp = combu(:,48);
hq = combu(:,49);
hr = combu(:,50);
hs = combu(:,51);
ht = combu(:,52);
hu = combu(:,53);
hv = combu(:,54);
hw = combu(:,55);
hx = combu(:,56);
hy = combu(:,57);
hz = combu(:,58);
ia = combu(:,59);
ib = combu(:,60);
ic = combu(:,61);
id = combu(:,62);
ie = combu(:,63);
If = combu(:,64);
ig = combu(:,65);
ih = combu(:,66);
ii = combu(:,67);
ij = combu(:,68);
ik = combu(:,69);
il = combu(:,70);
im = combu(:,71);
in = combu(:,72);
io = combu(:,73);
ip = combu(:,74);
iq = combu(:,75);
ir = combu(:,76);
is = combu(:,77);
it = combu(:,78);

figure(2)
scatter3(ea,eb,ec, 'MarkerFaceColor',[1 .6 .6])
hold on
scatter3(ed,ee,ef, 'MarkerFaceColor',[1 .6 .6])
hold on

```

```

scatter3(eg,eh,ei, 'MarkerFaceColor',[1 .6 .6])
hold on
scatter3(ej,ek,el, 'MarkerFaceColor',[1 .6 .6])
hold on
scatter3(em,en,eo, 'MarkerFaceColor',[1 .6 .6])
hold on
scatter3(ep,eq,er, 'MarkerFaceColor',[1 .6 .6])
hold on
scatter3(es,et,eu, 'MarkerFaceColor',[1 .6 .6])
hold on
scatter3(ev,ew,ex, 'MarkerFaceColor',[1 .6 .6])
hold on
scatter3(ey,ez,fa, 'MarkerFaceColor',[1 .6 .6])
hold on
scatter3(fb,fc,fd, 'MarkerFaceColor',[1 .6 .6])
hold on
scatter3(fe,ff,fg, 'MarkerFaceColor',[1 .6 .6])
hold on
scatter3(fh,fi,fj, 'MarkerFaceColor',[1 .6 .6])
hold on
scatter3(fk,fl,fm, 'MarkerFaceColor',[1 .6 .6])
hold on
scatter3(fn,fo,fp, 'MarkerFaceColor',[1 .6 .6])
hold on
scatter3(fq,fr,fs, 'MarkerFaceColor',[1 .6 .6])
hold on
scatter3(ft,fu,fv, 'MarkerFaceColor',[0 .7 .7])
hold on
scatter3(fw,fx,fy, 'MarkerFaceColor',[0 .7 .7])
hold on
scatter3(fz,ga,gb, 'MarkerFaceColor',[0 .7 .7])
hold on
scatter3(gc,gd,ge, 'MarkerFaceColor',[0 .7 .7])
hold on
scatter3(gf,gh,gi, 'MarkerFaceColor',[0 .7 .7])
hold on
scatter3(gj,gk,gl, 'MarkerFaceColor',[0 .7 .7])
hold on
scatter3(gm,gn,go, 'MarkerFaceColor',[0 .7 .7])
hold on
scatter3(gp,gq,gr, 'MarkerFaceColor',[0 .7 .7])
hold on
scatter3(gs,gt,gu, 'MarkerFaceColor',[0 .7 .7])
hold on
scatter3(gv,gw,gx, 'MarkerFaceColor',[0 .7 .7])
hold on
scatter3(gy,gz,ha, 'MarkerFaceColor',[0 .7 .7])
hold on
scatter3(hb,hc,hd, 'MarkerFaceColor',[0 .7 .7])
hold on
scatter3(he,hf,hg, 'MarkerFaceColor',[0 .7 .7])
hold on
scatter3(hh,hi,hj, 'MarkerFaceColor',[0 .7 .7])
hold on
scatter3(hk,hl,hm, 'MarkerFaceColor',[0 .7 .7])
hold on
scatter3(hn,ho,hp, 'MarkerFaceColor',[0 .7 .7])
hold on

```

```

scatter3(hq,hr,hs, 'MarkerFaceColor',[0 .7 .7])
hold on
scatter3(ht,hu,hv, 'MarkerFaceColor',[0 .7 .7])
hold on
scatter3(hw,hx,hy, 'MarkerFaceColor',[0 .7 .7])
hold on
scatter3(hz,ia,ib, 'MarkerFaceColor',[0 .7 .7])
hold on
scatter3(ic,id,ie, 'MarkerFaceColor',[0 .7 .7])
hold on
scatter3(If,ig,ih, 'MarkerFaceColor',[0 .7 .7])
hold on
scatter3(ii,ij,ik, 'MarkerFaceColor',[0 .7 .7])
hold on
scatter3(il,im,in, 'MarkerFaceColor',[0 .7 .7])
hold on
scatter3(io,ip,iq, 'MarkerFaceColor',[0 .7 .7])
hold on
scatter3(ir,is,it, 'MarkerFaceColor',[0 .7 .7])
xlabel('Specific Thrust')
ylabel('Specific Fuel Consumption')
zlabel('Overall Efficiency')
title('Scramjet Analysis')

%% Rocket Analysis

% Given
g1 = 1.3;
go = 9.81;
Cp = 1004;
T_t4 = 2200;
P_c1 = 74374.45;
P_e = linspace(0.00001,0.50,900);
P_a6 = linspace(0.00001,0.50,900);
A_str = linspace(0.9,2,900);
P_c = linspace(1000,10000000,900);

% Ambient Pressures
P_a = 0.05;
P_a1 = 0.025;
P_a2 = 0.005;
P_a3 = 0.001;
P_a4 = 0;
P_a5 = 0.013;
P_a7 = 0.04;
P_a8 = 0.008;
P_a9 = 0.009;
P_a10 = 0.023;
P_a11 = 0.019;
P_e1 = 0.5;

[e1, Cf, c_st, Ft, v_e, m_dot, Isp] = space(g1,P_e,P_a,Cp,T_t4,P_c,A_str,go);
[e2, Cf2, c_st1, Ft1, v_e1, m_dot1, Isp1] =
space(g1,P_e,P_a1,Cp,T_t4,P_c,A_str,go);
[e3, Cf3, c_st2, Ft2, v_e2, m_dot2, Isp2] =
space(g1,P_e,P_a2,Cp,T_t4,P_c,A_str,go);

```

```

[e4, Cf4, c_st3, Ft3, v_e3, m_dot3, Isp3] =
space(g1,P_e,P_a3,Cp,T_t4,P_c,A_str,go);
[e5, Cf5, c_st4, Ft4, v_e4, m_dot4, Isp4] =
space(g1,P_e,P_a4,Cp,T_t4,P_c,A_str,go);
[e6, Cf6, c_st6, Ft5, v_e5, m_dot5, Isp5] =
space(g1,P_e,P_a6,Cp,T_t4,P_c1,A_str,go);
[e7, Cf7, c_st7, Ft6, v_e6, m_dot6, Isp6] =
space(g1,P_e,P_a5,Cp,T_t4,P_c,A_str,go);
[e8, Cf8, c_st8, Ft7, v_e7, m_dot7, Isp7] =
space(g1,P_e,P_a7,Cp,T_t4,P_c,A_str,go);
[e9, Cf9, c_st9, Ft8, v_e8, m_dot8, Isp8] =
space(g1,P_e,P_a8,Cp,T_t4,P_c,A_str,go);
[e10, Cf10, c_st10, Ft9, v_e9, m_dot9, Isp9] =
space(g1,P_e,P_a9,Cp,T_t4,P_c,A_str,go);
[e11, Cf11, c_st11, Ft10, v_e10, m_dot10, Isp10] =
space(g1,P_e,P_a10,Cp,T_t4,P_c,A_str,go);
[e12, Cf12, c_st12, Ft11, v_e11, m_dot11, Isp11] =
space(g1,P_e,P_a11,Cp,T_t4,P_c,A_str,go);
abc = Isp(:,(4:900));
TF = islocalmax(Cf(:,(4:900)));
TF1 = islocalmax(Cf2(:,(4:900)));
TF2 = islocalmax(Cf3(:,(4:900)));
TF3 = islocalmax(Cf4(:,(4:900)));
TF4 = islocalmax(Cf5(:,(4:900)));
TF5 = islocalmax(Cf6(:,(4:900)));
TF6 = islocalmax(Cf7(:,(4:900)));
TF7 = islocalmax(Cf8(:,(4:900)));
TF8 = islocalmax(Cf9(:,(4:900)));
TF9 = islocalmax(Cf10(:,(4:900)));
TF10 = islocalmax(Cf11(:,(4:900)));
TF11 = islocalmax(Cf12(:,(4:900)));

figure(3)
plot(e1(:,(4:900)),Cf(:,(4:900)),e1(TF),Cf(TF),'*','Color',[0 0
1],'LineWidth',1)
hold on
plot(e1(:,(4:900)),Cf2(:,(4:900)),e1(TF1),Cf2(TF1),'*','Color',[1 0
1],'LineWidth',1)
hold on
plot(e1(:,(4:900)),Cf3(:,(4:900)),e1(TF2),Cf3(TF2),'*','Color',[1 0
0],'LineWidth',1)
hold on
plot(e1(:,(4:900)),Cf4(:,(4:900)),e1(TF3),Cf4(TF3),'*','Color',[0 1
0],'LineWidth',1)
hold on
plot(e1(:,(4:900)),Cf5(:,(4:900)),e1(TF4),Cf5(TF4),'*','Color',[0 0
0],'LineWidth',1)
hold on
plot(e1(:,(4:900)),Cf6(:,(4:900)),e1(TF5),Cf6(TF5),'*','Color',[0 1
1],'LineWidth',1)
hold on
plot(e1(:,(4:900)),Cf7(:,(4:900)),e1(TF6),Cf7(TF6),'*','Color',[0.9290 0.6940
0.1250],'LineWidth',1)
plot(e1(:,(4:900)),Cf8(:,(4:900)),e1(TF7),Cf8(TF7),'*','Color',[0.8500 0.3250
0.0980],'LineWidth',1)
plot(e1(:,(4:900)),Cf9(:,(4:900)),e1(TF8),Cf9(TF8),'*','Color',[0.6350 0.0780
0.1840],'LineWidth',1)

```

```

plot(e1(:,(4:900)),Cf10(:,(4:900)),e1(TF9),Cf10(TF9),'*','Color',[0.3010
0.7450 0.9330],'LineWidth',1)
plot(e1(:,(4:900)),Cf11(:,(4:900)),e1(TF10),Cf11(TF10),'*','Color',[0.4940
0.1840 0.5560],'LineWidth',1)
plot(e1(:,(4:900)),Cf12(:,(4:900)),e1(TF11),Cf12(TF11),'*','Color',[0.4660
0.6740 0.1880],'LineWidth',1)
legend('Pa=0.05','Pa=0.05','Pa=0.025','Pa=0.025','Pa=0.005','Pa=0.005','Pa=0.
001','Pa=0','Pa=(0 to
0.5)','Pa=0.013','Pa=0.013','Pa=0.04','Pa=0.04','Pa=0.008','Pa=0.008','Pa=0.0
09','Pa=0.009','Pa=0.023','Pa=0.023','Pa=0.019','Pa=0.019')
xlabel('Expansion Ratio [\epsilon]')
ylabel('Coefficient of Thrust [C_f]')
title('Study 3')

```

```

figure(4)
plot(e1(:,(4:900)),v_e(:,(4:900)),'Color',[0.4660 0.6740
0.1880],'LineWidth',1)
hold on
plot(e1(:,(4:900)),v_e1(:,(4:900)),'g-','LineWidth',1)
hold on
plot(e1(:,(4:900)),v_e2(:,(4:900)),'m-','LineWidth',1)
hold on
plot(e1(:,(4:900)),v_e3(:,(4:900)),'Color',[0 0.4470 0.7410],'LineWidth',1)
hold on
plot(e1(:,(4:900)),v_e4(:,(4:900)),'b-','LineWidth',1)
hold on
plot(e1(:,(4:900)),v_e6(:,(4:900)),'r-','LineWidth',1)
hold on
plot(e1(:,(4:900)),v_e7(:,(4:900)),'Color',[0.4940 0.1840
0.5560],'LineWidth',1)
legend('Pa=0.05','Pa=0.025','Pa=0.005','Pa=0.001','Pa=0','Pa=(0 to
0.5)','Pa=0.013','Pa=0.04','Pa=0.008','Pa=0.009','Pa=0.023','Pa=0.019')
xlabel('Expansion Ratio [\epsilon]')
ylabel('Exit Velocity [V_e]')
title('Study 2')

```

```

figure(5)
plot3(Cf(:,(4:900)),v_e(:,(4:900)),Isp(:,(4:900)),'r','LineWidth',1)
hold on
plot3(Cf2(:,(4:900)),v_e1(:,(4:900)),Isp1(:,(4:900)),'b','LineWidth',1)
hold on
plot3(Cf3(:,(4:900)),v_e2(:,(4:900)),Isp2(:,(4:900)),'k','LineWidth',1)
hold on
plot3(Cf4(:,(4:900)),v_e3(:,(4:900)),Isp3(:,(4:900)),'c','LineWidth',1)
hold on
plot3(Cf5(:,(4:900)),v_e4(:,(4:900)),Isp4(:,(4:900)),'y','LineWidth',1)
hold on
plot3(Cf6(:,(4:900)),v_e6(:,(4:900)),Isp5(:,(4:900)),'Color',[0.4660 0.6740
0.1880],'LineWidth',1)
plot3(Cf7(:,(4:900)),v_e7(:,(4:900)),Isp6(:,(4:900)),'Color',[0.3010 0.7450
0.9330],'LineWidth',1)
xlabel('Coefficient of Thrust')
ylabel('Exit Velocity [m/s]')
zlabel('Specific Impulse [secs]')
title('Design Point for Rocket')
legend('Pa=0.05','Pa=0.025','Pa=0.005','Pa=0.001','Pa=0','Pa=(0 to
0.5)','Pa=0.013','Pa=0.04','Pa=0.008','Pa=0.009','Pa=0.023','Pa=0.019')
grid on

```

```

function [e1,Cf,c_st,Ft,v_e,m_dot,Isp] =
space(g1,P_e,P_a,Cp,T_t4,P_c,A_str,go)
G = sqrt(g1*((1+g1)/2)^((1+g1)/(1-g1)));
b1 = (2.*g1)./(g1-1);
a1 = (P_e).^(2./g1);
c1 = 1-((P_e).^(g1-1./g1));
e1 = G./sqrt((b1).*(a1).*(c1));
Cf = G.*(sqrt(((2.*g1)./(g1-1)).*(1-(P_e).^((g1-1)./g1))))+(P_e-P_a).*(e1);
m_dot = (P_c.*A_str.*G)./sqrt(Cp.*((g1-1)./g1).*T_t4);
Ft = (P_c.*A_str.*G).*(sqrt(((2.*g1)./(g1-1)).*(1-(P_e).^(g1-
1./g1))))+(P_e)-(P_a)).*(e1);
c_st = (Ft./(m_dot.*Cf));
v_e = sqrt((2./g1-1).*(Cp.*(g1-1./g1)).*T_t4.*(1-(P_e).^(g1-1./g1)));
Isp = Ft./(m_dot.*go);
end

```

Appendix C – MATLAB code for staging

```
clear all
close all
clc

% Staging
W_gtot = 6945994.287915;
W_emp = 4850221.0286876;
g_o = 9.81;
mpl = 96274.75097;

% Mass transformations
m_e1 = (W_emp/g_o)*(1/9);
m_e2 = (W_emp/g_o)*(1/10);
m_e3 = (W_emp/g_o)*(1/11);
m_o1 = W_gtot/g_o
pp_pl = mpl/m_o1
m_o2 = mpl/((pp_pl)^(2/3))
m_o3 = mpl/((pp_pl)^(1/3))

% Given conditions
Isp_1 = 450;
c1 = 3.13;
e_1 = (m_e1)/(m_o1-m_o2)
Isp_2 = 400;
c2 = 0.829;
e_2 = (m_e2)/(m_o2-m_o3)
mpl = 96274.75125;
Isp_3 = 375;
c3 = 1.098;
e_3 = (m_e3)/(m_o3-mpl)
ep = (e_1+e_2+e_3)/2;
I = (Isp_1+Isp_2+Isp_3)/2;
v_bo = (I*g_o*log(1/(((pp_pl)^(1/3))*(1-ep)+ep))^3)/1000;

% Equations
syms n
eqn = c1*log(c1*n-1)+c2*log(c2*n-1)+c3*log(c3*n-1)-((c1+c2+c3)*log(n))-
((c1*log(c1*e_1))+(c2*log(c2*e_2))+(c3*log(c3*e_3))) == 5.656;
S = (vpasolve(eqn,n));

% Optimum Mass Ratios
n1 = ((c1*S)-1)/(c1*e_1*S)
n2 = ((c2*S)-1)/(c2*e_2*S)
n3 = ((c3*S)-1)/(c3*e_3*S)

% Step Masses
m3 = (n3-1)*(mpl)/(1-(n3*e_3));
m2 = (n2-1)*(mpl+m3)/(1-(n2*e_2));
m1 = (n1-1)*(m2+mpl+m3)/(1-(n1*e_1));

% Empty and propellant masses
me1 = e_1*m1;
me2 = e_2*m2;
me3 = e_3*m3;
```

```

mp1 = m1-me1;
mp2 = m2-me2;
mp3 = m3-me3;

% Payload Ratios
l_1 = (m3+m2+mp1)/(m1);
l_2 = (m3+mp1)/(m2);
l_3 = mp1/(m3);

% Total mass of vehicle
m_o = m1+m2+m3+mp1;

% Overall payload
p_pl = mp1/m_o;

% Check the results above
ch_1 = (S*c1*(e_1*n1-1)^2)+(2*e_1*n1)-1;
ch_2 = (S*c2*(e_2*n2-1)^2)+(2*e_2*n2)-1;
ch_3 = (S*c3*(e_3*n3-1)^2)+(2*e_3*n3)-1;

```